

AD A 069826

LEVEL

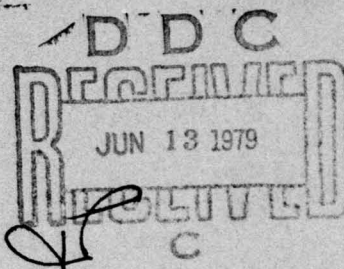
12

CR79-623

# PARTICLE IMPACT DAMAGE IN CERAMICS

TECHNICAL REPORT

March 1979



Submitted to the

Office of Naval Research  
800 N. Quincy Street  
Arlington, VA 22217

by

William F. Adler  
Timothy W. James

This document has been approved  
for public release and sale; its  
distribution is unlimited.

DDC FILE COPY

Reproduction in whole or in part is permitted for  
any purpose of the United States Government

This research was sponsored by the Office of Naval  
Research under Contract No. N00014-76-C-0744,  
NR 032-565.

EFFECTS TECHNOLOGY, INC.  
5383 Hollister Avenue  
Santa Barbara, California 93111

79 06 13 009

14

ETI - CR79-623

6

PARTICLE IMPACT DAMAGE IN CERAMICS.

9

TECHNICAL REPORT,

11

March 1979

12 150p.

15

Contract No. ~~N00014-76-C-0744~~

Project No. 471 (NR 032-565)

Prepared for the

Office of Naval Research  
800 N. Quincy Street  
Arlington, VA 22217

by

10

William F./Adler  
Timothy W./James

EFFECTS TECHNOLOGY, INC.  
5383 Hollister Avenue  
Santa Barbara, California 93111  
(805) 964-9831

405 842

LB



UNCLASSIFIED

SECURITY CLASSIFICATION OF THIS PAGE (When Data Entered)

REPORT DOCUMENTATION PAGE		READ INSTRUCTIONS BEFORE COMPLETING FORM
1. REPORT NUMBER	2. GOVT ACCESSION NO.	3. RECIPIENT'S CATALOG NUMBER
4. TITLE (and Subtitle)  PARTICLE IMPACT DAMAGE IN CERAMICS		5. TYPE OF REPORT & PERIOD COVERED Technical
7. AUTHOR(s)  W. F. Adler and T. W. James		6. PERFORMING ORG. REPORT NUMBER CR79-623
		8. CONTRACT OR GRANT NUMBER(s) N00014-76-C-0744
9. PERFORMING ORGANIZATION NAME AND ADDRESS Effects Technology, Inc. 5383 Hollister Avenue Santa Barbara, CA 93111		10. PROGRAM ELEMENT, PROJECT, TASK AREA & WORK UNIT NUMBERS  Project No. 471 (NR 032-565)
11. CONTROLLING OFFICE NAME AND ADDRESS Office of Naval Research 800 North Quincy Street Arlington, VA 22217		12. REPORT DATE March 1979
		13. NUMBER OF PAGES 144
14. MONITORING AGENCY NAME & ADDRESS (if different from Controlling Office)		15. SECURITY CLASS. (of this report) Unclassified
		15a. DECLASSIFICATION DOWNGRADING SCHEDULE
16. DISTRIBUTION STATEMENT (of this Report)  Approved for public release; distribution unlimited.		
17. DISTRIBUTION STATEMENT (of the abstract entered in Block 20, if different from Report)		
18. SUPPLEMENTARY NOTES		
19. KEY WORDS (Continue on reverse side if necessary and identify by block number) water drop impingement, impact, polymethylmethacrylate, ceramics, fracture, magnesium oxide, calcium fluoride, lithium fluoride, particulate erosion		
20. ABSTRACT (Continue on reverse side if necessary and identify by block number) The objective of this research is to understand and model the deformation and fracture response of materials exposed to water drop collisions. Due to the inherent complexity of the erosive response of materials exposed to a multiple water drop environment, this investigation concentrated on a very idealized water drop impact condition: the normal impact of a spherical water drop on a plane surface. The development of an experimental facility is described for producing spherical water drop impacts on materials at both subsonic and supersonic impact velocities. A reproducible, controlled, and well-characterized impact condition is necessary if		

DD FORM 1 JAN 73 1473

EDITION OF 1 NOV 55 IS OBSOLETE

UNCLASSIFIED

SECURITY CLASSIFICATION OF THIS PAGE (When Data Entered)

UNCLASSIFIED

SECURITY CLASSIFICATION OF THIS PAGE (When Data Entered)

an accurate assessment of the material's response is to be established.

The response of polymethylmethacrylate (PMMA) and single crystals of magnesium oxide (MgO), calcium fluoride (CaF<sub>2</sub>), and lithium fluoride (LiF) has been investigated for 1.5 to 2.0 mm water drops impacting from 200 to 700 ms<sup>-1</sup>.

Detailed microscopic examination of water drop impacted PMMA has provided a reasonably comprehensive picture of its deformation and fracture response including several unknown features of the resulting damage. This information will form the basis for analytical studies of the general impact process.

The slip and fracture observed in the crystalline materials corresponded to the same systems and planes identified for quasistatic loading conditions. However the deformation due to water drop impacts is such that material is displaced in directions away from the impact plane in contrast to rounded solid particle loadings which produce displacements both in directions in the impact plane as well as away from it.

For impacts on (001) MgO it was demonstrated that introduction of numerous active slip sources into the impact face is an effective means for reducing the impact damage and completely eliminating fracture for the impact velocities tested which approach 600 ms<sup>-1</sup>. The numerous active sources allow deformation to take place by slip (rather than fracture) at rates greater than can be accommodated by dislocation multiplication methods in surfaces with very few active sources.

However the presence of numerous active slip sources in CaF<sub>2</sub> was not sufficient to eliminate water drop impact fractures over the velocity range investigated.

The difference in the response of MgO which exhibits extensive slip and insignificant fracture or none at all, and CaF<sub>2</sub> which exhibits extensive crack growth and very limited slip can be attributed to their respective fracture energies and critical shear stresses. MgO has a much higher ratio of fracture energy to shear stress than CaF<sub>2</sub>, therefore the preference of CaF<sub>2</sub> to fracture rather than slip when compared to MgO is understandable. The fact that it is the ratio of fracture energy to shear stress rather than the magnitude of either property is borne out by the impacts on LiF. LiF is much softer than either CaF<sub>2</sub> or MgO (based on the magnitude of the critical resolved shear stress and microhardness) but has a high ratio of fracture energy to shear stress and exhibits, as does MgO, limited fracture and extensive slip. It is apparent that water drop impact resistance in single crystals will benefit most from increases in fracture energy rather than hardness.

Accession For	
NTIS	<input checked="checked" type="checkbox"/>
DDC TAB	<input type="checkbox"/>
Unannounced	<input type="checkbox"/>
Justification	
By	
Distribution	
Availability Codes	
Dist	Availand/or special
<input checked="checked" type="checkbox"/>	

UNCLASSIFIED



## TABLE OF CONTENTS

<u>SECTION</u>		<u>PAGE</u>
1.0	INTRODUCTION	1
2.0	LIQUID DROP IMPACT FACILITY	5
2.1	General Description of Liquid Drop Impact Facility	6
2.2	Development of Liquid Drop Impact Facility	14
2.3	Characterization of Impact Conditions	20
2.3.1	Liquid Drop Distortion Prior to Impact	21
2.3.2	Ellipsoidal Drop Impact Characteristics	30
3.0	WATER DROP IMPACTS ON POLYMETHYLMETHACRYLATE	39
3.1	Related Observations	39
3.2	Experimental Results and Discussion	45
4.0	WATER DROP IMPACTS ON SINGLE CRYSTALS	63
4.1	Magnesium Oxide	72
4.1.1	Specimen Preparation and Characterization	72
4.1.2	Slip Band Structure in Water Drop Impacted Specimens	74
4.1.3	Fracture Initiation Mechanisms	93
4.2	Calcium Fluoride	103
4.2.1	Specimen Preparation and Characterization	103
4.2.2	Dislocation Etch Pit Patterns on $\text{CaF}_2$	104
4.2.3	Fracture Geometries	113
4.3	Lithium Fluoride	118
4.3.1	Specimen Preparation and Characterization	118
4.3.2	Dislocation Slip Bands in (001) Impacted LiF	120
4.3.3	Impact Fracture Patterns on (001) LiF	123
5.0	SOFT PARTICLE SIMULATION OF WATER DROP IMPACT DAMAGE	127
6.0	CONCLUSIONS	137
	REFERENCES	141

# LIST OF ILLUSTRATIONS

<u>FIGURE</u>		<u>PAGE</u>
2.1	Liquid Drop Impact Facility	7
2.2	Specific Gravity of Water-Glycol Solutions at 15.6°C	10
2.3	Viscosity of Water and Ethylene Glycol	11
2.4	Vapor Pressure of Water and Ethylene Glycol	11
2.5	Typical Appearance of Water Drop Prior to Impact for Impact Velocities from 200 to 700 ms <sup>-1</sup> at a Pressure of 0.1 torr or less	19
2.6	Wave Diagram	23
2.7	Density and Velocity History	23
2.8	Non-Dimensional Time of Exposure for ETI Facility	26
2.9	Regimes of Droplet Deformation and Breakup (from Ranger and Nicholls, 1969)	27
2.10	Estimates of Drop Distortion (adapted from Lankford and Leverance, 1971)	29
2.11	Ellipsoidal Drop Geometry	31
2.12	Contact Radii for Ellipsoidal Drops as a Function of Contact Angle	34
2.13	Critical Radii for Lateral Outflow for Ellipsoidal Drops as a Function of Impact Velocity	36
3.1	Characteristic Water Drop Impact on PMMA. 1.5 mm Water Drop Impacting at 356 ms <sup>-1</sup>	40
3.2	Form of Circumferential Fractures Described by Lankford, et al. (1973)	43
3.3	Summary of Experimental Values of the Characteristic Dimensions for Depressed Annulus on PMMA Due to Water Drop Impacts	46
3.4	Graphical Evaluation of Impact Pressure and Particle Velocities for a Water Impact on PMMA at 700 ms <sup>-1</sup>	49
3.5	1.6 mm Water Drop Impacting at 476 ms <sup>-1</sup>	52
3.6	1.6 mm Water Drop Impacting at 520 ms <sup>-1</sup>	53
3.7	1.9 mm Water Drop Impacting at 660 ms <sup>-1</sup>	54



# LIST OF ILLUSTRATIONS (continued)

<u>FIGURE</u>		<u>PAGE</u>
3.8	Subsurface Deformation and Fracture on Cross Sections of PMMA Specimens as a Function of Impact Velocity	56
3.9	Characteristic Water Drop Impact on PMMA at $300 \text{ ms}^{-1}$ Showing Deformation Marking Usually Present	60
3.10	1.8 mm Water Drop Impact on PMMA at $390 \text{ ms}^{-1}$	61
4.1	1.70 mm Water Drop Impact on Si(111) at $313 \text{ ms}^{-1}$	70
4.2	1.82 mm Water Drop Impact on $\text{CaF}_2(111)$ at $326 \text{ ms}^{-1}$	70
4.3	1.61 mm Water Drop Impact on Ge(111) at $305 \text{ ms}^{-1}$	71
4.4	Dislocation Etched (001) Surface of MgO Specimen Prepared for Impact	75
4.5	Dislocation Etched Water Drop Impacts on (001) Face of MgO	76
4.6	Dislocation Etched Impact Face and Cross Section of MgO Specimens	79
4.7	Sketch of Slip Bands Present and Coordinate System Used for Single Drop Impacts on MgO	81
4.8	Characteristic Rosette Pattern for Sapphire Bead Impact on (001) MgO	84
4.9	Etched Cross Section Showing Slip Bands and Fractures in MgO	87
4.10	Dislocation Etched Impact Face and Non-center-line Cross Section of Shot No. 808	88
4.11	Nature of Water Drop Impact Damage on Mechanically-Polished MgO	91
4.12	Dislocation Etched Impact Face and Cross Section of Shot No. 858 ( $413 \text{ ms}^{-1}$ )	92
4.13	Inner Region of One Quadrant of Fig. 4.5	94
4.14	Slip Band Interaction for Fracture Initiation Proposed By Stokes, et al. (1958, 1959, 1960)	98
4.15	Crack Formation on (110) Plane in MgO Crystals	100
4.16	Cross Section of Nylon Bead Impact at $1000 \text{ ms}^{-1}$ on (001) MgO	102

# LIST OF ILLUSTRATIONS (continued)

<u>FIGURE</u>		<u>PAGE</u>
4.17	Dislocation Etched {111} Face on $\text{CaF}_2$ Single Crystal Showing In-grown Dislocation Density and Low Angle Tilt Boundary	105
4.18	Dislocation Etched {111} Impacts on $\text{CaF}_2$	106
4.19	Geometric Orientations of Slip Bands on a {111} Face and their Burgers Vectors	110
4.20	Dislocation Etched {100} Impacts on $\text{CaF}_2$	111
4.21	(110) Cross Section of Water Drop Impact on {111} $\text{CaF}_2$ at $307 \text{ ms}^{-1}$	115
4.22	(100) Cross Section of a Water Drop Impacting at $548 \text{ ms}^{-1}$ (Shot No. 914) on (001) $\text{CaF}_2$	116
4.23	Lightly Dislocation Etched (001) Surface of LiF Prepared for Impact Revealing In-Grown Dislocation Content and Low Angle Tilt Boundaries	119
4.24	Dislocation Etched Water Drop Impact on (001) LiF at $385 \text{ ms}^{-1}$ (Shot No. 980)	121
4.25	Fracture Annulus for Shot No. 980 (Impacted at $385 \text{ ms}^{-1}$ ) Viewed in Transmitted Light	124
4.26	Unetched Water Drop Impact on (001) LiF at $555 \text{ ms}^{-1}$ (Shot No. 915)	126
5.1	Schematic Representation of the Observed Subsurface Fracture Patterns for Water Drop and Nylon Bead Impacts on CVD Zinc Sulfide	130
5.2	Surface and Subsurface Fractures Due to Particle Impacts on CVD zinc sulfide	134



# LIST OF TABLES

<u>TABLE</u>		<u>PAGE</u>
3.1	Representative Dimensions Associated with Surface and Subsurface Circumferential Fractures	59
4.1	Properties of Single Crystals	64
4.2	Water Drop Impacts on Single Crystals	65
4.3	Fracture Data for Single Crystals	114
5.1	Grain Size Dimensions for CVD Zinc Sulfide	131
512	Summary of Particle Impact Damage Dimensions on CVD Zinc Sulfide	133

## 1.0 INTRODUCTION

A basic understanding of water drop impact damage in materials is evolving as a result of the development of a facility for controlled and well-characterized single water drop impact testing, microscopic examination of the damaged target materials to elucidate and quantify the dominant modes of failure, and utilization of computational procedures describing the water drop loading sequence and the dynamic response of the target. The focused research activity in the investigation of liquid drop impact damage in transparent materials over the past few years has provided insights into the means for adequately addressing the problem of liquid drop erosion of materials at high subsonic to supersonic impact velocities. The capacity for existing and developmental materials to withstand particle impacts, primarily protective covers for electromagnetic sensing devices exposed to hostile environments, can be studied in considerable depth. Observations of the fracture initiation modes and resultant crack morphologies produced in controlled particle impact experiments provide a valuable data base for identifying the material properties governing the damage process. This information can be used in a number of ways to suggest improvements in the particle impact resistance of specific materials.

A ballistic range test facility was selected as the most desirable means for obtaining single water drop impacts on brittle and semi-brittle crystals, however a number of technical difficulties were encountered in providing the damaged specimens required in this research program. A significant developmental effort was required to establish suitable stopping and retrieval conditions for the brittle specimens fired down the range which would not introduce any damage other than that due to impact with a single water drop and to eliminate a variety of problems associated with maintaining the integrity of the water drop before impacting the specimen. A completely satisfactory system is now operational.



In retrospect the course of the present investigation has developed along lines paralleling in many ways an overall program pursued by Lankford and Leverance (1971; Lankford, et al., 1973) concerned with water drop impact damage on slip cast fused silica radome materials. They proposed a five-phase program which they felt was necessary before a thorough understanding of water drop impact damage could be achieved. Their approach was based on the following:

1. Development of controlled experimental techniques,
2. Accumulation of accurate data on control materials and developmental materials,
3. Development of simple but effective methods of damage evaluation,
4. Correlation of damage characteristics for discrete impacts with material properties, and
5. Comparison with theories and correlation where possible of discrete impacts with erosion results.

Phases one to three were addressed during the course of this effort which apparently was not completed.

While several details of the program outlined differ from the present investigation, the philosophical aspects expounded by Lankford and Leverance in their reports pertaining to the discrete impact approach in relation to other means for producing and evaluating water drop impact damage on materials are consistent with our perspective of the research in progress. Considerable attention and developmental effort have been devoted to obtaining spherical drop impacts on materials. The evolution of the experimental facility to provide controlled impact conditions from subsonic to low supersonic velocities is described in Section 2.2.

During the course of this developmental effort, single water drop impacts were obtained on polymethylmethacrylate (PMMA) and oxide-based glass specimens at velocities up to  $700 \text{ ms}^{-1}$ . The quality of the water drop impacts obtained in the liquid drop impact facility is judged on the basis of the PMMA and glass control materials. This is to assure that uniform drop impacts are actually produced when investigating crystalline solids at velocities where the symmetry of the impact may not be as evident. The damage observed on these materials is compared with other single drop impact data found in the literature. Several inconsistencies are noted in Section 3 for the reported supersonic water drop impact damage in PMMA. Water drop impact damage on single crystals of magnesium oxide, calcium fluoride, and lithium fluoride is described and analyzed in Section 4.

Phase 3 of the approach outlined by Lankford and Leverance involved two tasks: quantification of the damage produced and alternative means for producing the general features of water drop collisions. The first task was not carried to a meaningful end, but they did classify the transitions in the type of damage which occurs with increasing impact velocity based on low magnification microscope examination of the impacted surface. They also used profilometer traces to characterize the large scale surface features and crater characteristics. Lankford and Leverance sought a simple laboratory methodology for evaluating the rain erosion resistance of developmental materials. They used various solid particles as an alternative to water drops and arrived at the same conclusion previously stated by Fyall (1967; 1970, Fyall and Smith, 1973) based on his ballistic range experiments. Fyall experimentally evaluated the collision of solid spheres as a simulation procedure for water drop impacts. After examining the flow behavior for a number of materials during impact using high-speed photography and measuring the dimensions of the resulting depressions in PMMA, he concluded that the use of solid particles to simulate rain erosion damage on materials has little merit. However he did not rule out the possibility that the solid body impacts may be useful in ranking

materials with respect to their rain erosion resistance. The materials Fyall used for the particles in his experiments were polyethylene, nylon, cellulose acetate, polytetrafluoroethylene, lead, tungsten carbide, steel, sapphire and even a water in wax sphere. In contrast to this result it will be shown in Section 5 that nylon bead impacts on polycrystalline zinc sulfide do produce both surface and subsurface fractures which are similar to those observed for water drop collisions. This work is still in progress, however, so any conclusion reached at this point would have to be considered tentative. Engel (1955) had concluded that the mechanisms of damage produced by the impact of deforming lead pellets and by the high-speed impingement of water drops on PMMA are identical. The difference between them being only one of degree. This comparison was based solely on micrographs of the impacted surface, however there does appear to be justification for exploring possible alternatives to water drop impact environments.



## 2.0 LIQUID DROP IMPACT FACILITY

Material damage due to rain erosion for actual flight conditions depends on the drop size distribution, the drop attack angle, the ambient pressure and temperature, and the local shape of the vehicle. The effectiveness of the multiple water drop collisions in producing material damage is directly related to the form, quantity, impact velocity, and attack angle of the water which reaches a particular location on the vehicle. The aerodynamics of the flow fields the drops encounter and drop penetration of the inviscid or shock layer around a moving vehicle have been described by several analysts and experimentalists. These are important aspects of applied erosion situations.

Due to the inherent complexity of the erosive response of materials exposed to a multiple water drop environment, the present investigation experimentally reproduced a very idealized water drop impact condition: the normal impact of a spherical water drop on a plane surface. The number of impact parameters influencing the response of the target materials is thereby minimized. The additional advantage of having spherical water drop collisions is that a direct association can be established between the experimental results and analytical approaches which are formulated for this idealized impact condition. Since the pressure distribution acting on the expanding interface between an impacting water drop and a deformable target is just beginning to become known, it is essential to have a well-characterized and reproducible test configuration in order to quantify the fracture response of a material due to a water drop collision. The development of a water drop impact facility to experimentally achieve the idealized impact condition has become a fairly substantial undertaking, although it was never the intent of this program to make this a major effort, it has of necessity become an integral part of the overall program.

The general features and capabilities of the liquid drop impact facility will be described. Brief mention will be made of the developmental evolution of the facility and the upgraded requirements imposed which have now been satisfied in order to conduct the material response investigations reported in Section 4. During the course of the development of a test facility to provide a reproducible spherical drop impact on the plane face of the target material, the impact conditions achieved in other facilities were examined in terms of the available published details for these facilities. On the basis of this survey it was found that potential and confirmed deviations from a spherical drop collision prevail in liquid drop facilities.

## 2.1 GENERAL DESCRIPTION OF LIQUID DROP IMPACT FACILITY

A schematic of the ETI liquid drop impact facility is shown in Fig. 2.1. The specimen is mounted at the front end of a sabot which is propelled down the range by a small charge of gunpowder. Water drops are formed at the tip of a hypodermic needle mounted above the test section and fall in the path of the moving specimen. A slotted rail system is used to guide the sabot through the test section and into the recovery tube. As a single drop falls from the tip of the hypodermic needle it interrupts a pair of fiber optics links situated at right angles to each other. If both beams are disrupted, this action initiates the firing sequence. The system is calibrated so the sabot reaches the drop when it has fallen to a point within the limits of the exposed surface of the specimen. After impacting the water drop the sabot enters the recovery tube. A graded distribution of material in the recovery tube controls the deceleration of the sabot and protects the face of the specimen from extraneous damage. As shown in Fig. 2.1 the total length of the recovery system is only 8 meters.

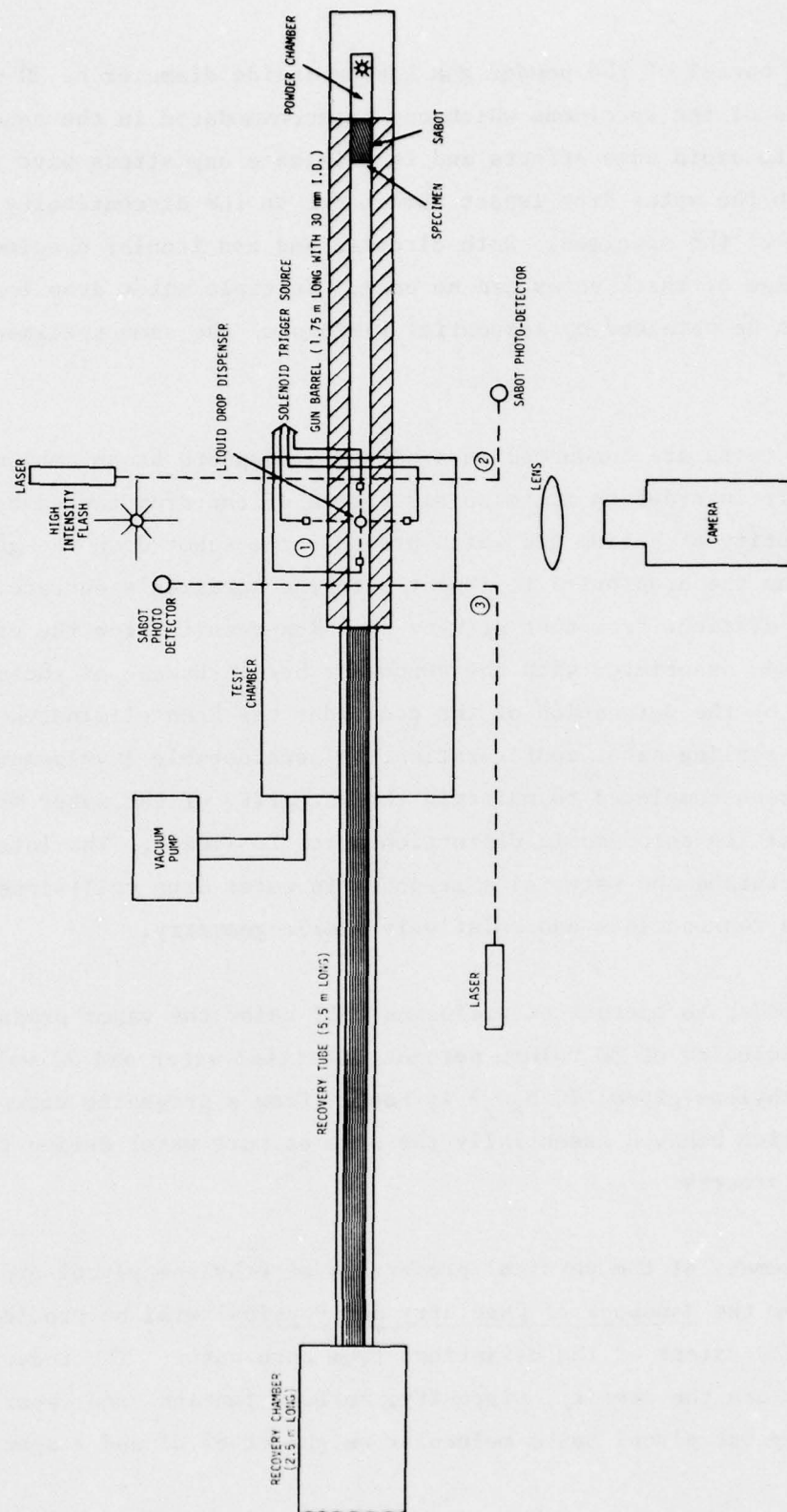


Figure 2.1. Liquid Drop Impact Facility.



The barrel of the powder gun has an inside diameter of 30 mm. The dimensions of the specimens which can be accommodated in the sabot are adequate to avoid edge effects and to eliminate any stress wave interactions with the water drop impact damage due to the discontinuity at the back face of the specimen. Both circular and noncircular specimens with a wide range of thicknesses can be used. Multiple water drop impact damage can be obtained by sequential firings of the same specimen down the range.

The tests are conducted in a helium atmosphere at an ambient pressure of 0.1 torr in order to minimize distortion of the drop caused by the small quantity of helium gas which precedes the sabot down the gun barrel and engages the drop prior to impact with the specimen's surface. This effect is distinct from that of blow-by which results from the expansion of the gases associated with the gunpowder burn. Escape of these gases generated by the detonation of the gunpowder has been eliminated by means of a self-sealing sabot configuration. A considerable developmental effort has been completed to maintain the integrity of the water drop and to minimize its aerodynamic distortion prior to impact. The intent here is to understand the material's response to water drop collisions which requires a reproducible and relatively simple geometry.

In order to operate at pressures well below the vapor pressure of water, a solution of 80 volume percent distilled water and 20 volume percent ethylene glycol ( $C_2H_6O_2$ ) is used. From a pragmatic viewpoint this solution behaves essentially the same as pure water during the collision process.

A summary of the physical properties of ethylene glycol and water (taken from the Handbook of Chemistry and Physics) will be provided to indicate the extent of the deviations from pure water. The relevant properties are the density, viscosity, surface tension, and vapor pressure. Ethylene glycol has a molecular weight of 62.07 and a specific

gravity of 1.1155 at 20°C. It has an infinite solubility in water with a molecular weight of 18.02. The specific gravity of the water-glycol solution used in the water drop impact experiments is 1.03 at 15.6°C (60°F) as determined from the plot in Fig. 2.2. The data in Fig. 2.3 compares the viscosity of the two liquids. The water-glycol solution should fall into a viscosity range where relatively minor differences would be expected in the drop impact characteristics of this solution compared to pure water. On the other hand the surface tension of ethylene glycol in air at 20°C is 4.77 Pa while the corresponding value for water is 7.275 Pa. The vapor pressures of water and ethylene glycol as a function of temperature are plotted in Fig. 2.4. Based on our experiments the effects of vaporization of the water-glycol solution at pressures on the order of 0.1 torr appear to be negligible over the temperature range from 5 to 20°C. Fig. 2.4 shows that it would not be possible to operate effectively below a pressure of 5 to 10 torr if pure water was used.

The water-glycol solution is deaerated. The temperature of the solution is typically slightly below room temperature: approximately 15°C. Chilling the solution has the advantage of lowering the vapor pressure, but this advantage has to be balanced against an increase in viscosity. The deaerated water-glycol solution is placed in a reservoir above the test chamber where it is drawn into a vertically mounted syringe. Manually applied pressure to the syringe initiates drop formation at the tip of the hypodermic needle. If the drops are forming satisfactorily at the test pressure when viewed through an optical microscope with a magnification of about seven times, a single drop is photographed as it falls between the guide rails at the elevation of the specimen. The integrity and general appearance of the drop is checked from this photograph. If it passes this visual inspection, the pressure in the system is checked to confirm that it matches the desired test pressure, the pre-set firing sequence is unlocked, and detonation of the gun-powder takes place as a subsequent drop interrupts the dual fiber optics links passing above the test chamber corresponding to station ① in

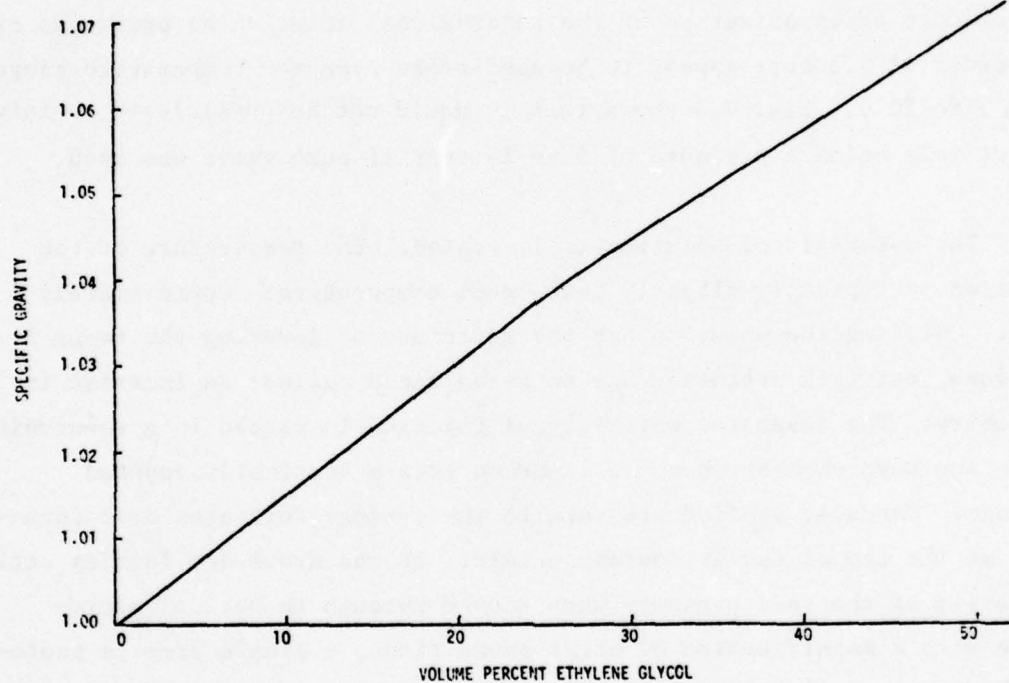


Figure 2.2. Specific Gravity of Water-Glycol Solutions at 15.6°C.



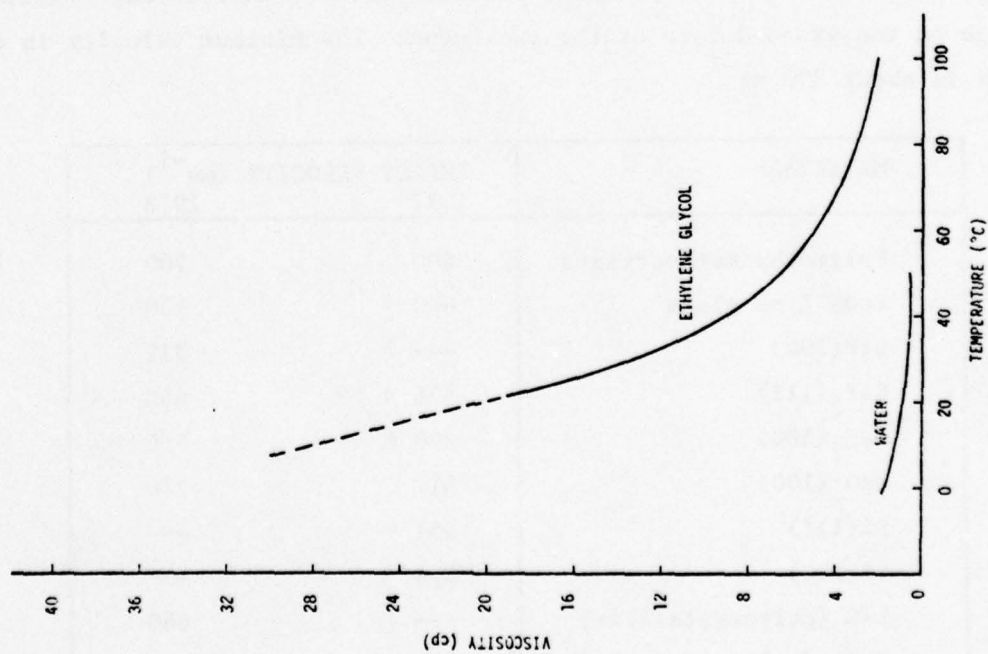


Figure 2.3. Viscosity of Water and Ethylene Glycol.

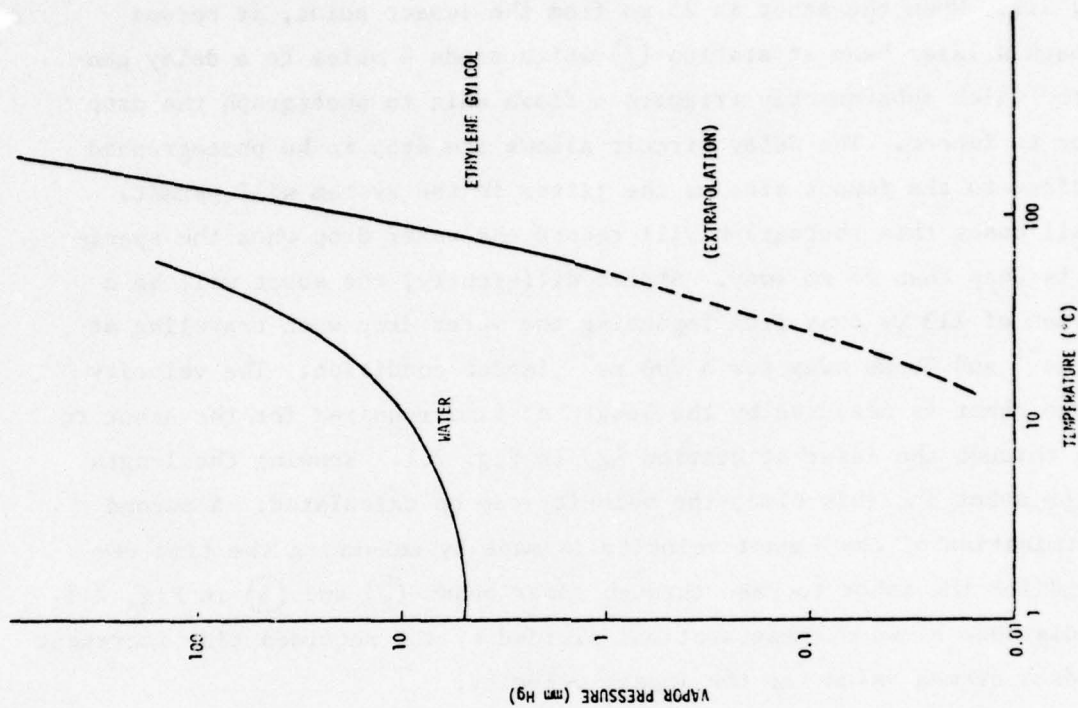


Figure 2.4. Vapor Pressure of Water and Ethylene Glycol

Fig. 2.1. When the sabot is 25 mm from the impact point, it passes through a laser beam at station (2) which sends a pulse to a delay generator which subsequently triggers a flash unit to photograph the drop prior to impact. The delay circuit allows the drop to be photographed as close to the impact site as the jitter in the system will permit. In all cases this photograph will record the water drop when the specimen is less than 25 mm away. Stated differently, the sabot will be a maximum of 113  $\mu\text{s}$  away from impacting the water drop when traveling at 222  $\text{ms}^{-1}$  and 36  $\mu\text{s}$  away for a 700  $\text{ms}^{-1}$  impact condition. The velocity of the sabot is measured by the length of time required for the sabot to pass through the laser at station (2) in Fig. 2.1. Knowing the length of the sabot and this time, the velocity can be calculated. A second determination of the impact velocity is made by measuring the time required for the sabot to pass through laser beams (2) and (3) in Fig. 2.1. The distance between these stations divided by the recorded time increment yields a second value for the impact velocity.

Water drop impacts at the velocities indicated below have been obtained in the liquid drop impact facility without introducing extraneous damage on the exposed face of the specimens. The minimum velocity in all cases is about 200  $\text{ms}^{-1}$ .

MATERIAL	IMPACT VELOCITY ( $\text{ms}^{-1}$ )	
	1977	1978
Polymethylmethacrylate	600	700
Soda lime glass	600 *	700
LiF(100)	---	512
CaF <sub>2</sub> (111)	326 *	550
CaF <sub>2</sub> (100)	290 *	550
MgO (100)	612	770
Si(111)	351 *	---
Si(100)	388 *	---
ZnS (polycrystalline)	---	680
ZnSe (polycrystalline)	---	645

The velocities denoted by an asterisk indicate the specimens consistently cracked at this and higher velocities. The velocities listed for 1978 (after several modifications were made to the water drop impact facility) are not the maximum values obtainable before cracking of the specimen occurs but are the velocities for which the features of the water drop impact damage are well developed. In most cases considerable velocity increases would be required to produce a significant change in the general fracture mode.

At the end of 1977 the impact conditions for single crystals of silicon and calcium fluoride were judged to be marginal in that specimen cracking occurred after a small increase in impact velocity beyond the single water drop fracture threshold. This condition limits the range of drop impact velocities and makes specimen survivability improbable for multiple impacts. This motivated a moderate developmental effort to improve the recovery system in the facility to provide an expanded range of experimental conditions.

Several modifications were made in the liquid drop impact facility during 1978 which include:

- Increased length of the specimen recovery system (from 5.5 to 8 m).
- Analysis and implementation of optimal distributions of graded material for decelerating the sabot in the recovery system at higher impact velocities.
- Redesign of the specimen sabot for maintenance of water drop integrity prior to impact and recovery of fragile specimens.
- Improved diagnostics for timing the impact event and photographing the drop prior to impact.



The water drop impact conditions are being carefully analyzed and characterized as indicated in Section 2.3. Photographic records of the individual drop impacts are taken so that an accurate assessment can be made of the damage in the target material in response to the actual applied loading function.

## 2.2 DEVELOPMENT OF LIQUID DROP IMPACT FACILITY

A brief account of the evolution of the liquid drop impact facility will be given, since experiments were conducted at various stages of its development under conditions which are different than those finally achieved. Although many of the earlier test results have been discarded in favor of a limited number of water drop impacts obtained under the near ideal impact conditions currently attainable in the liquid drop impact facility, some general observations will of necessity be made on the basis of the earlier experiments.

Using 2 mm water drops, impact velocities in the vicinity of  $300 \text{ ms}^{-1}$  were initially thought to be sufficient to produce substantial damage in single crystals of calcium fluoride, silicon, and magnesium oxide. This assumption was based on our previous experience with multiple water drop impacts on ceramic materials (Adler and Hooker, 1976), however it was found that a broader range of velocities was desirable for investigating the damage modes in these materials after this initial objective was achieved. Relatively little damage was found on magnesium oxide specimens at 300 to  $400 \text{ ms}^{-1}$  and the number of successful water drop impacts was judged to be marginal for silicon and calcium fluoride in that specimen cracking occurred during recovery after a small increase in impact velocity beyond the single water drop fracture threshold which occurs in both materials in the neighborhood of  $300 \text{ ms}^{-1}$ . This recovery problem limited the velocity range for investigation and made specimen survivability improbable for multiple impacts. The water drop impact facility was therefore modified by increasing the length of the recovery distance by one-half the initial distance, modifying the materials used to decelerate the

sabot, and redesigning the sabot configuration for better isolation of the specimen from the imposed loads. Successful and essentially routine water drop impacts can now be obtained over the expanded velocity range indicated for the representative materials listed at the end of Section 2.1.

Numerous problems had to be overcome in the liquid drop impact facility in order to achieve the present level of operational capability. Some analysis could be utilized but in general trial and error procedures which progressively led to innovations in the experimental arrangement proved most effective. The major problems involved maintenance of the spherical shape of the water drop prior to impact and recovering fairly fragile specimens after impact without introducing additional damage or completely fracturing the specimen. Soda lime and borosilicate glass specimens were used as an inexpensive means to evaluate the susceptibility of the actual test specimens to gross fracture during the acceleration phase and the subsequent deceleration of the water drop impacted specimens. Polymethylmethacrylate (PMMA) specimens were used to check the quality of the water drop impact and to evaluate the recovery damage which may occur due to material in the recovery tube contacting the face of the specimen. PMMA is ideally suited for this purpose over the velocity range of 200 to 700  $\text{ms}^{-1}$  since impressions of material contact are easily formed. While recovery of the PMMA was not difficult, the glass specimens required a significantly improved recovery system. Advances made in the sabot design and firing sequence which produced good water drop impacts had to be balanced against the latitude available for successfully recovering the specimen. The outcome of hundreds of firings of the powder gun has been the empirical solution to a multidimensional problem in variational calculus. It is not known if the optimal conditions have been reached, however an acceptable solution is now in hand.

The attainment of spherical water drops is highly dependent on the ambient pressure, since the inviscid layer at the front of the sabot will interact with the water drop to cause distortion. The minute quantity of

gas which can affect the water drop was not fully realized in the early stages of the facility development. Much experimentation was carried out to eliminate blow-by due to the expansion of the combustion gases due to the gunpowder burn. A distinction ultimately had to be made between water drop distortion due to blow-by and the interaction with the small quantity of gas remaining in the gun barrel even at ambient pressures of 10 torr or less. The efforts to eliminate or at least minimize these effects will be recounted.

Since the water drop impact takes place in a closed system, it was anticipated that reduced pressures would be required to minimize the influence of the compressed air at the front of the sabot on the water drop. A water drop with its low value of viscosity and surface tension is quite susceptible to distortion even from the slightest perturbation in the local pressure. Gases are also generated by the gunpowder burn which propel the sabot down the barrel of the gun. Venting these gases, which in many applications involving a powder gun is not critical, became a major undertaking. Since these combustion gases are expanding faster than the sabot, they can escape around the sabot as it travels down the barrel and reach the drop first. An enlarged blast chamber was incorporated into the system but only provided a marginal improvement. The guided rail system tended to channel the gases in the direction of the drop. The sabot weight was reduced by shortening the sabot length so that it would accelerate faster and possibly outdistance the expanding combustion gases. This series of experiments was carried out with PMMA specimens. When glass was used in the shortened sabot, the specimens fractured due to the shock wave transmitted to the back face of the specimen from the gunpowder blast. While this appeared to be a move in the right direction, it was not satisfactory for fragile, brittle specimens. It became evident that this approach was of limited utility.

Procedures to isolate the specimen from the impulse imparted to the sabot were then introduced. The specimen was placed in an aluminum cup filled with a low impedance polymeric material in order to isolate it



from the stresses imposed during launch and recovery. Epoxy mounting materials, silicone sealing materials, and elastomeric molding materials were introduced to reduce the stresses imparted to the specimen. An elastomeric molding material was selected as being most effective. The aluminum cup was then fitted into the sabot and a cover plate placed over the surface to be impacted with a 12 mm diameter hole which exposed the central portion of the specimen. The cover plate and an extended nose on the front end of the sabot reduced the potential for recovery damage.

The blow-by problem was eliminated by modifying the outlet on the powder chamber and finally arriving at the proper dimensions for a sealing flange on the rear end of the sabot. Gunpowders with different burn rates were tried to determine the best condition for accelerating the sabot such that the combustion gases were contained by the sealing flange. Unfortunately drop distortion persisted to the extent that the drop actually burst in several instances. In order to see whether it was possible to obtain a stable drop at all, mineral oil was used to gain the advantage of an increased viscosity. This proved effective but produced impact damage on PMMA distinctly different than that observed previously for water drop impacts. Since good impacts were at least being obtained with mineral oil, it was then thought that it may be possible to relax the conditions on the viscosity and use dilute polymeric solutions whose viscosity and density would be closer to water. The system was now being purged with helium, so a lower density gas was present in the system at a pressure on the order of 1 torr. It was difficult to realize that at this pressure enough helium would be present in the gun barrel to produce a plug of gas in front of the sabot which distorted the water drop when the separation distance was from 2 to 4 cm. After exploring several other possibilities, this was the only one that remained. A lower pressure would be required. The combination of ethylene glycol and water was then introduced and greatly improved results were obtained at 0.25 to 0.50 torr.

Subsequent improvements in the vacuum pumping system and the drop generation technique resulted in drops being introduced into the helium atmosphere at 0.1 torr. By our present photographic procedure, which records the condition of the drop when it is less than 25 mm from the face of the sabot, no measurable drop distortion is observed. Prior tests conducted at 0.3 torr still indicated the drops were deforming to an ellipsoidal shape. Considerable variability in the drop shape is observed. However essentially spherical drops are obtained at a pressure of 0.1 torr as shown in Fig. 2.5. The sabot is seen to the right of the falling water drop as viewed through the slotted channel in the test chamber.

Deceleration of the test specimens over a reasonable velocity range was a second major problem area which required an effort equal to that for obtaining spherical drop impacts. At present a soda lime glass specimen can be recovered after impacting a water drop at  $700 \text{ ms}^{-1}$  (slightly in excess of Mach 2) in a stopping distance of less than 8 meters without introducing extraneous damage. This is all the more remarkable since a 2 mm water drop impact at Mach 2 produces a sizable fracture zone which penetrates to millimeter depths on the glass specimen. This is accomplished by the sabot configuration and a velocity-dependent distribution of several materials in the recovery tube which avoids large increments in the magnitude of the deceleration pressure. Calculations were carried out in order to determine the densities of the materials required. The conditions for a uniform pressure curve combined with considerable trial and error experience produced the final material distributions which have been found to be effective.

Thus the back end of the sabot is designed to isolate the impulse imparted to the sabot to accelerate it to the desired velocity from the specimen and to completely seal the gases from the gunpowder burn behind the sabot, while the front end of the sabot is designed to impact the graded material without transferring a significant amount of stress to the specimen and to keep the recovery material away from the exposed face

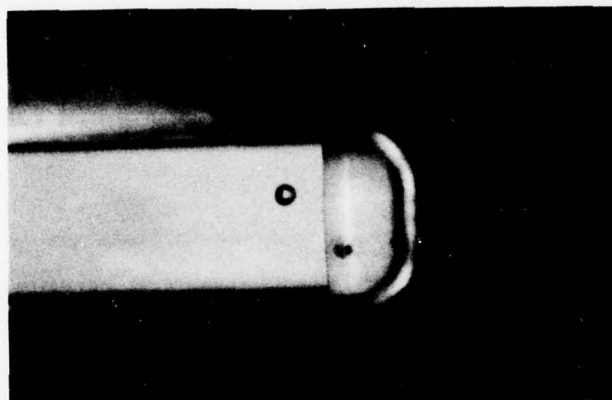


Figure 2.5. Typical Appearance of Water Drop Prior to Impact for Impact Velocities from 200 to 700  $\text{ms}^{-1}$  at a Pressure of 0.1 torr or less.



of the specimen. The mass of the sabot will be directly related to the magnitude of the recovery stresses and therefore has been reduced as much as possible while still affording the protection indicated above.

While the problem of drop distortion is intimately associated with the experimental arrangement use here, it is also a consideration in other test configurations. In many instances the characteristics of the drop prior to impact is totally unknown, and it is simply assumed to be a spherical drop of a stated mean diameter. This is not satisfactory for quantifying the fracture response for various materials subjected to water drop impingement. The relevant analyses for estimating the degree of drop distortion possible and the implications of using nonspherical drops will be explored in the next section.

### 2.3 CHARACTERIZATION OF IMPACT CONDITIONS

The literature pertaining to water drop distortion and break up will be utilized to examine the gas layer/water drop interactions in the ETI liquid drop impact facility. In order to compare the data generated in ballistic ranges or rotating arm facilities, it is important to know the quantity, form, and properties of the water which actually impacts the specimen. The characteristics of the drops impacting the surface thus become an integral aspect of characterizing the material response.

The conditions prevailing in the ETI liquid drop impact facility have been estimated using the available analyses and compared with direct observations of the water drop prior to impact. The level of distortion the drop experiences is thus known as it passes through the layer of gas which is pushed along the gun barrel by the sabot which acts like a piston in a cylinder. The effects of the gas layer are significantly reduced for supersonic impacts in this facility, however the interaction of a gas layer with the water drop is common to all facilities in which the specimen is accelerated to the desired impact velocity. Liquid jet impingement on the other hand eliminates these considerations. The specimen is now stationary and an air shock precedes the arrival of the head of the water jet (Field, et al., 1974).

### 2.3.1 Liquid Drop Distortion Prior to Impact

The extent of drop distortion in the ETI liquid drop impact facility will be estimated for the range of operating conditions which provided successful water drop impacts. The sabot is propelled down the barrel of the 30 mm ID gun for 1.75 m in a helium atmosphere before it impacts the water drop. The ambient pressure has ranged from 0.1 to 10 torr. As the sabot accelerates, the ambient helium is compressed by a wave system which runs ahead and produces gas flow over the falling water drop. To investigate the potential distortion of the drop, an estimate of the severity of the flow field is required. An evaluation of the sabot trajectory is needed for this purpose which will now be provided.

The gun is modeled as a constant diameter preburned propellant ideal gas gun. For this case Siegal (1965) gives the following equation which relates the sabot velocity  $u$  to its position  $x$  :

$$\frac{x A \rho_o}{\gamma m} = \frac{2}{\gamma + 1} \left[ \frac{\frac{2}{\gamma - 1} - \frac{\gamma + 1}{\gamma - 1} \left[ 1 - \frac{u(\gamma - 1)}{2a_o} \right]}{\left[ 1 - \frac{u(\gamma - 1)}{2a_o} \right]^{(\gamma + 1)(\gamma - 1)}} + 1 \right] \quad (2.1)$$

where a subscript  $o$  denotes the initial chamber conditions

$A$  = sabot base area ( $7.068 \text{ cm}^2$ )

$\gamma$  = specific heats ratio ( $\gamma = 1.18$  for the propellant)

$m$  = sabot mass ( $\sim 50 \text{ g}$ )

$a_o$  = sound speed =  $\sqrt{\gamma R T_o}$

$\rho_o$  = propellant gas density =  $P_o R T_o = m_p / v_p$

$R$  = gas constant  $R_o / M = 320 \frac{\text{N-m}}{\text{kg } ^\circ\text{K}}$

( $M$  is the molecular weight of the propellant which is taken to be 26)

$T_o$  = initial propellant temperature

$P_o$  = initial chamber pressure

$m_p$  = propellant mass ( $\sim 5$  g for a terminal velocity  
 $u_f = 700 \text{ ms}^{-1}$ )

$v_p$  = propellant chamber volume ( $\sim 16.387 \text{ cm}^3$ )

The sabot trajectory is obtained as follows. Given the impact velocity  $u_f$  at  $x_f = 1.75 \text{ m}$  (distance the sabot travels to engage water drop) and power charge  $m_p$ , Eq.(2.1) is solved for the effective sound speed  $a_o$ . Then  $u(x)$  can be found iteratively from Eq.(2.1). The corresponding time is found from

$$t = \int \frac{dx}{u}, \quad (2.2)$$

As the piston accelerates compression waves are generated which propagate ahead of the sabot. Until the waves coalesce, the flow remains isentropic. Assuming the compression is a "centered" set of waves (it is not in general, but this approximation is reasonable), the slope of the wave characteristic is related to the speed of the sabot  $u$  at the time of initiation (Leipmann and Roshko, 1957):

$$a = \left( \frac{dx}{dt} \right)_{\text{wave}} = a_{\infty} + \frac{\gamma+1}{2} u; \quad \gamma = 5/3 \text{ for helium} \quad (2.3)$$

where  $a_{\infty} = \sqrt{\gamma R_o T/M} = 1007 \text{ ms}^{-1}$  (helium at  $293^\circ\text{K}$ ).

From this, approximate wave diagrams can be constructed (Fig. 2.6), where  $u, \rho, a$ , etc. are constant along each wave. The density along each wave is (Leipmann and Roshko, 1957)

$$\rho = \rho_{\infty} \left( \frac{a}{a_{\infty}} \right)^{\frac{2}{\gamma-1}} \quad (2.4)$$



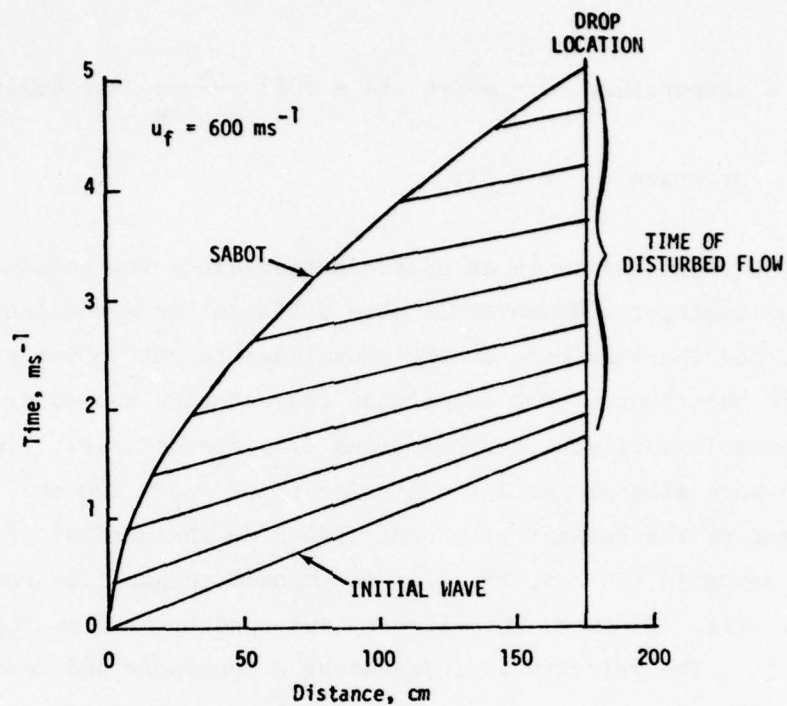


Figure 2.6. Wave Diagram.

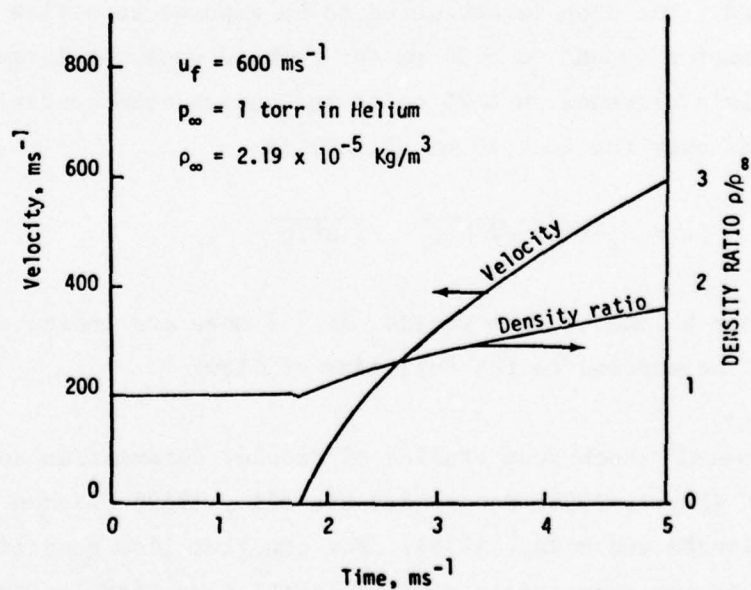


Figure 2.7. Density and Velocity History.

Also

$$\text{temperature } T = a^2/\gamma R \quad (R = 2077 \frac{\text{m}^2}{\text{sec}^2 \text{ } ^\circ\text{K}} \text{ for helium}) \quad (2.5)$$

$$\text{pressure } P = \rho RT \quad (2.6)$$

The present theory is an approximation since the actual breech is of finite length, the diameter is also different from the launch tube diameter, and the burn rate of the propellant is not infinite which are assumed in the theory. The calculated trajectories should at least provide reasonable estimates for computing drop distortions. Fig. 2.6 shows the wave diagram for a final velocity of  $u_f = 600 \text{ ms}^{-1}$  which is independent of the ambient pressure. Based on the arrival of the compression waves in the gas, the drop is exposed to gas flow for about 2.5 msec. Fig. 2.7 shows the velocity and density history for  $\rho_\infty = 1 \text{ torr}$ . The velocity is independent of pressure and density scales directly with pressure.

Since the drop is falling, the exposure time to the flow has to be determined. The drop is estimated to be exposed to a flow field which has a diameter around  $d \approx 30 \text{ mm}$  (or perhaps somewhat larger). The water drop falls a distance  $h \approx 25 \text{ cm}$  to the launch tube centerline. The time difference over the last 15 mm of fall is

$$\Delta t = t_f - t^* = \sqrt{2h/g} - \sqrt{2h^*/g} \quad (2.7)$$

where  $h^* = h - 15 \text{ mm}$ . This yields  $\Delta t \approx 7 \text{ msec}$  and indicates that the drop will be exposed to the full time of flow.

Several shock tube studies of droplet deformation and breakup have been made (Engel, 1958; Ranger and Nicholls, 1969; Waldman and Reinecke, 1971; Reinecke and McKay, 1976). For constant flow conditions (i.e., shock tube) the appropriate nondimensional time correlational variable is

$$T^* = (t u/D) \sqrt{\rho_{\text{gas}}/\rho_{\text{liquid}}} \quad (2.8)$$

where  $t$  = time during constant velocity flow  
 $u$  = flow speed relative to the drop  
 $D$  = initial diameter of drop  
 $\rho$  = density of ambient fluid or drop

For the present analysis both  $u$  and  $\rho_{\text{gas}}$  are variable. It is speculated that correlations of droplet break up and deformation will be usable if  $T^*$  is replaced by

$$T^* = \int_0^T \frac{u(t)}{D} \sqrt{\frac{\rho_{\text{gas}}(t)}{\rho_{\text{liquid}}}} dt \quad (2.9)$$

which is a time-averaged value.  $T$  is the elapsed time of the disturbed flow.

Fig. 2.8 shows the values of  $T^*$  calculated according to Eq.(2.9) for the velocity and drop size range available in the ETI facility. For similar conditions the drop deformation has been determined experimentally by Ranger and Nicholls (1969). Up to about  $T^* \approx 1.25$  the drops flatten linearly with  $T^*$  to blunt ellipsoids of about  $D/D_0 \approx 3.0$  (Fig. 2.9). After that (larger  $T^*$ ) stripping of the fluid occurs with eventual drop breakup. Waldman and Reinecke (1971) indicate that catastrophic breakup occurs at  $T^* \approx 3.5$ . Thus to avoid significant drop distortion, it is necessary to keep  $T^* < 0.5$ . According to the data compiled in Fig. 2.8, this can be accomplished in the ETI liquid drop facility if the ambient pressure in helium is on the order of 0.1 torr.

In actual fact the photographic records of the drop prior to impact show that negligible distortion of the drop takes place at a pressure of 0.1 torr. As indicated in Section 2.1 a photograph of the drop is taken



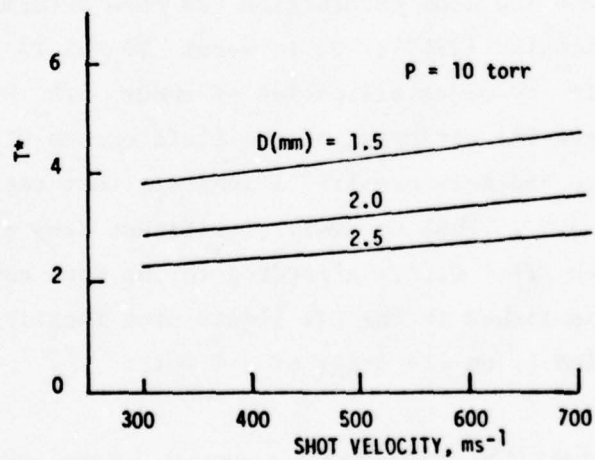
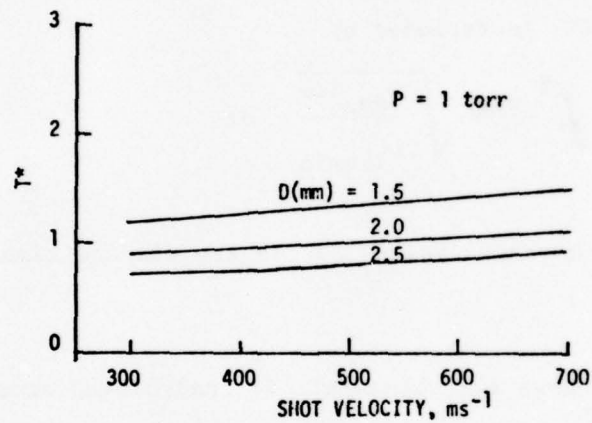
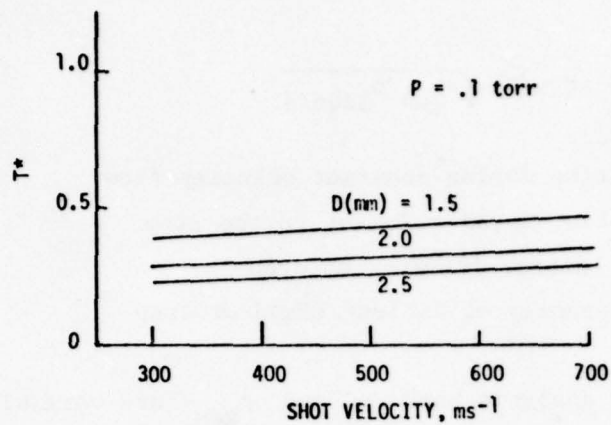


Figure 2.8. Non-Dimensional Time of Exposure for ETI Facility.

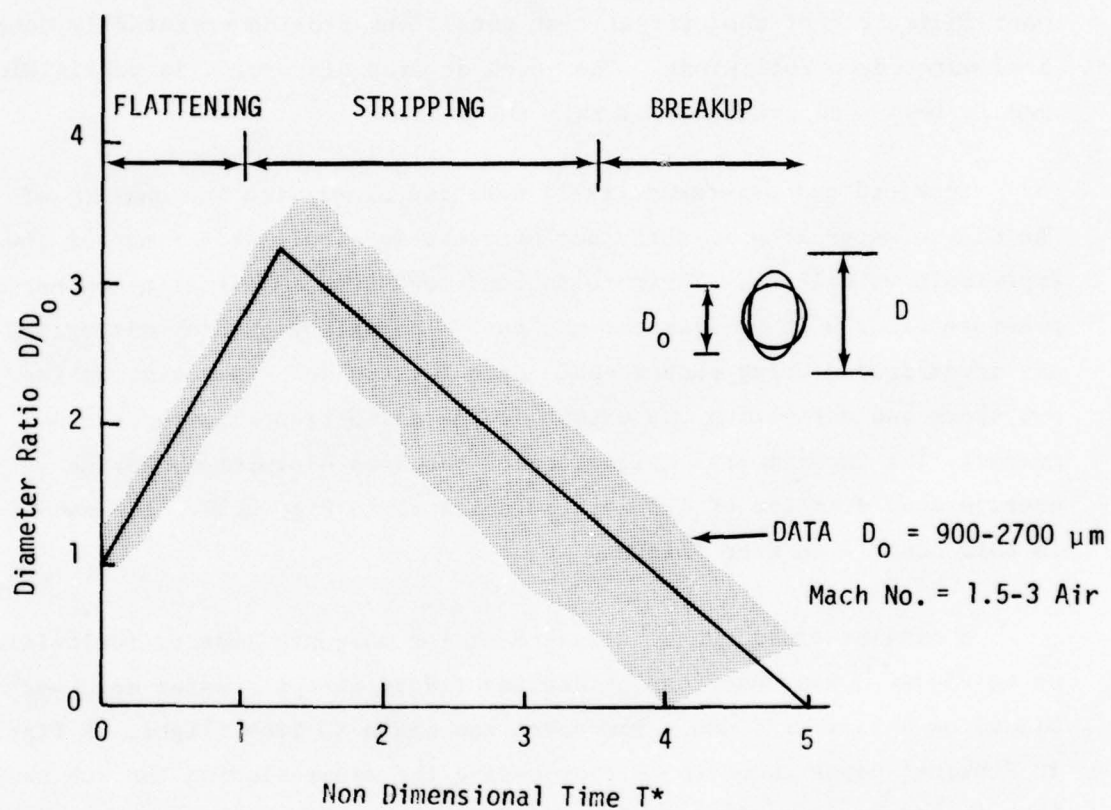


Figure 2.9. Regimes of Droplet Deformation and Breakup (from Ranger and Nicholls, 1969).

when the sabot is less than 25 mm from the drop as shown in Fig. 2.5. The previous computations indicate that the travel time for the sabot is greater than 5 msec at velocities less than  $700 \text{ ms}^{-1}$ . The time required for the sabot to travel the last 25 mm is typically less than 0.1 msec, so the dimensions taken from the photograph of the drop on this basis should be representative of the drop dimensions just before it impacts the specimen. Direct observations of the drop prior to impact indicate that the current test conditions provide essentially spherical water drop collisions. The level of drop distortion is negligible and is less than predicted by this analysis.

Lankford and Leverance (1971) were concerned with the quality of the single water drop impacts they obtained in a ballistic range at low supersonic velocities. Their tests were conducted in air at atmospheric pressure using a 20 mm diameter gas gun. The extent of drop distortion was investigated using photographic data for the drops penetrating the bow shock and estimating the extent of the distortion from the photographs. The experimental evaluation of the drop distortion, for an average drop diameter of 1.2 mm, is indicated in Fig. 2.10. The sabot in this case is in free flight.

A similar experimental arrangement for subsonic impacts (velocities up to  $250 \text{ ms}^{-1}$ ) was described by Jenkins (1955) except a water drop was placed on a polymeric web. The sabot was again in free flight. A figure in Jenkins' paper shows the air preceding the sabot blowing the web away from the drop. According to Jenkins this leaves "a roughly spherical drop to be struck by the projectile." This gas gun configuration was used subsequently by Fyall (1967) and Kinner (1967).



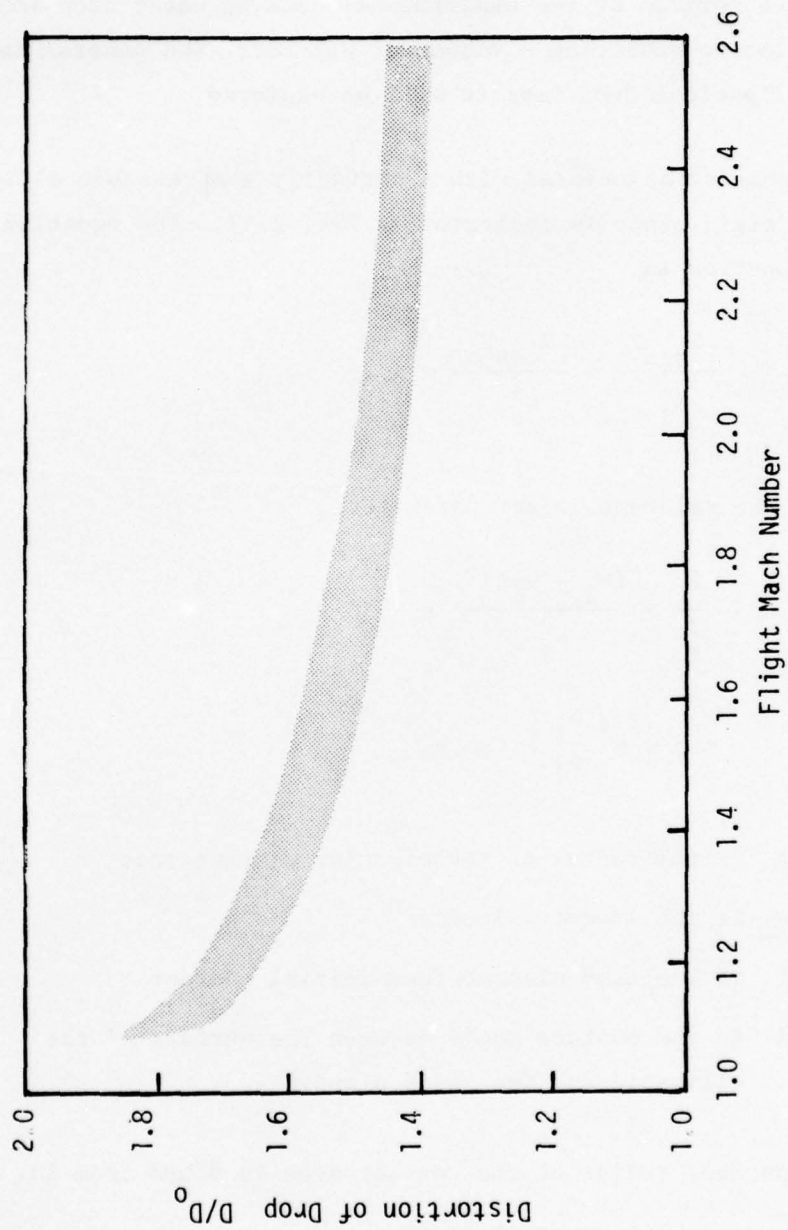


Figure 2.10. Estimates of Drop Distortion  
(adapted from Lankford and Leverance, 1971).

### 2.3.2 Ellipsoidal Drop Impact Characteristics

Since a portion of the experimental data on water drop impacts was acquired prior to achieving a vacuum of 0.1 torr, the general implications of ellipsoidal drop impacts will be explored.

The geometry associated with a perfectly compressible ellipsoid impacting a rigid plane is indicated in Fig. 2.11. The equation for the elliptical section is

$$\frac{r^2 \sin^2 \alpha}{b_1^2} + \frac{r^2 \cos^2 \alpha}{b_2^2} = 1 . \quad (2.10)$$

In terms of the relevant impact parameters,

$$\frac{c^2}{b_1^2} + \frac{(b_2 - v_o t)^2}{b_2^2} = 1 \quad (2.11)$$

and  $\tan \alpha = \left( \frac{b_1}{b_2} \right) \tan \phi \quad (2.12)$

where  $c$  is the radius of the circular contact area  
 $v_o$  is the impact velocity  
 $t$  is the time elapsed from initial contact  
 $\phi$  is the contact angle between the surface of the ellipsoid and the rigid plane.

The time-dependent radius of the contact area is found from Eq. (2.11),

$$c(t) = \left( \frac{b_1}{b_2} \right) \sqrt{2b_2 v_o t - (v_o t)^2} \quad (2.13)$$

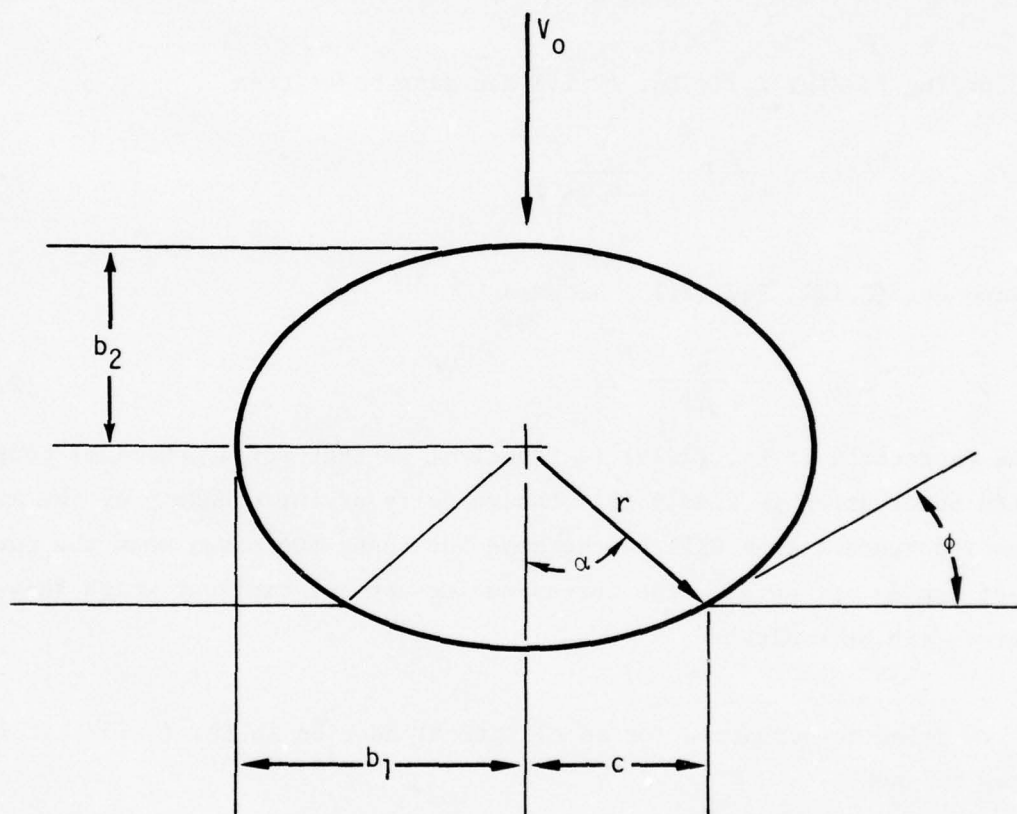


Figure 2.11. Ellipsoidal Drop Geometry.



Differentiating Eq. (2.13) yields the rate of expansion of the contact radius,

$$\dot{c}(t) = \left( \frac{b_1}{b_2} \right) \frac{v_o (b_2 - v_o t)}{\left[ 2b_2 v_o t - (v_o t)^2 \right]^{1/2}} = \left( \frac{b_1}{b_2} \right)^2 \frac{v_o (b_2 - v_o t)}{c} \quad (2.14)$$

According to Fig. 2.11, Eq. (2.14) can also be written

$$\dot{c}(t) = \left( \frac{b_1}{b_2} \right)^2 \frac{v_o}{\tan \alpha(t)} \quad (2.15)$$

Using Eq. (2.12), Eq. (2.15) becomes

$$\dot{c}(t) = \frac{v_o}{\tan \phi(t)} \quad (2.16)$$

The expression in Eq. (2.16) is identical to that for a spherical body. This observation is simply that the velocity of the boundary of the expanding contact area will be the same for these two cases when the contact angles are equal. The corresponding contact radii at which this occurs can be evaluated.

Using the equation for an elliptical section in Eq. (2.10), it is easy to show

$$c = r \sin \alpha = \frac{b_1 \left( \frac{b_1}{b_2} \right) \sin \phi}{\left[ 1 - \sin^2 \phi \left( 1 - \frac{b_1}{b_2} \right)^2 \right]^{1/2}} \quad (2.17)$$

Denoting the radius of the contact zone for a spherical drop collision by  $a$ , then

$$a = r_o \sin\phi \quad (2.18)$$

where  $r_o$  is the radius of the sphere. The relations in Eq. (2.17) and (2.18) are plotted in Fig. 2.12 for  $\left(\frac{b_1}{b_2}\right)$  equal to 1.25 and 1.50.

Obviously, when  $\frac{b_1}{b_2} = 1$ , Eq. (2.17) degenerates into Eq. (2.18).

The previous analysis assumes the drop is perfectly compressible which is a reasonable assumption for the initial stages of the impact event. However incompressibility effects will become significant in conjunction with the onset of lateral outflow (Adler, 1979), and it would seem that differences in the nature of the lateral outflow velocities would occur between a spherical and ellipsoidal drop impact. It is our conjecture that whatever differences may arise would be relatively small as long as  $\frac{b_1}{b_2} \leq 1.5$ .

It is Adler's finding (Adler, 1979) that an adequate criterion for the onset of lateral outflow for a spherical drop does not exist, although a number of analyses can be found in the literature. A fairly wide dichotomy prevails between the elementary analyses, numerical calculations, and experimental measurements for disc-shaped drops. To date, there are no direct measurements of the critical lateral outflow parameters for spherical drop impacts. In view of this situation the widely accepted lateral outflow condition derived by Bowden and Field (1964) will be applied to an ellipsoidal drop. Their criterion is simply

$$\sin\phi_c = \frac{v_o}{C_w} \quad (2.19)$$

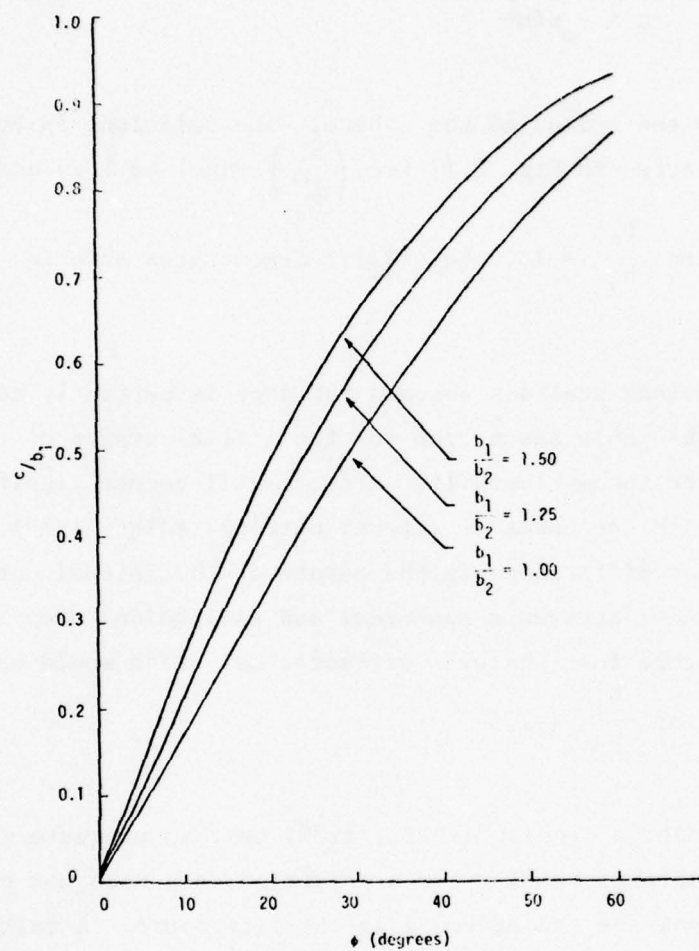


Figure 2.12. Contact Radii for Ellipsoidal Drops as a Function of Contact Angle.



where  $C_w$  is the compressional wave speed for water which is approximately 1.5 mm/ $\mu$ s . For the range of impact velocities under investigation the wave speed  $C_w$  should be replaced by Eq. (2.19) by the shock wave speed for water,  $U_w$  . According to Heymann (1968),

$$U_w = C_w (1 + 2M_o) \quad (2.20)$$

where  $M_o = v_o/C_w$  . The relation in Eq.(2.20) is valid for impacts on a rigid surface and when  $M_o < 1.2$  . Eq. (2.19) now takes the form

$$\sin\phi_c = \frac{a_c}{r_o} = \frac{M_o}{1 + 2M_o} \quad (2.21)$$

This is a lateral outflow criterion for spherical drops, however the same condition pertains to elliptical drops, since this is a condition on velocity components at the periphery of the contact zone. A diagram of the various velocity vectors is shown as an insert in Fig. 2.13. It was already shown, Eq. (2.16), that the expansion velocities of the contact zone were identical for a sphere and an ellipsoid for the same value of the contact angle. The critical contact radii for which this condition pertains are determined by Eq. (2.17) and (2.18) upon substitution of Eq. (2.21). The resulting expressions for the critical contact radii are plotted in Fig. 2.13 as a function of the impact velocity.

The aforementioned effects should have some influence on the pressure distribution applied to the surface of the target, since lateral outflow for ellipsoidal drops with  $b_1/b_2 \leq 1.5$  will occur at larger contact zone radii than spherical drops but the time required to reach these radial distances will be less. This should perturb the development of the pressure distribution. In contrast, note the different conditions which would prevail for a pancake-shaped drop. The drop distortions for our test conditions do not reach this extreme. Reiterating,

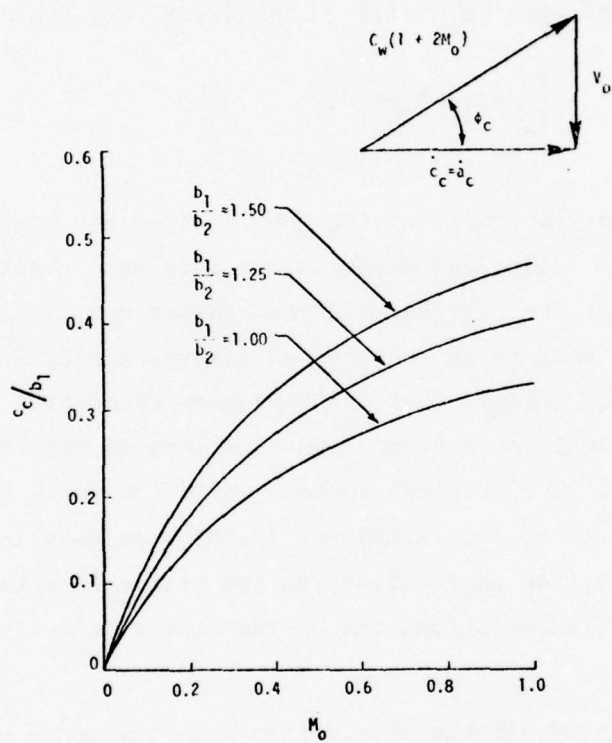


Figure 2.13. Critical Radii for Lateral Outflow for Ellipsoidal Drops as a Function of Impact Velocity.

the major difference between spherical and ellipsoidal drop impacts would be that the direct pressure is applied over a larger contact zone for the ellipsoidal drop compared with a spherical drop of the same mass, and the temporal and spatial distribution of the applied pressure should be the applied pressure modified as  $b_1/b_2$  increases.

Aerodynamic effects should have a perturbing influence on water drop geometry prior to impact in all facilities employing a specimen moving at high subsonic to supersonic velocities. If severe perturbations are not produced, it is extremely difficult to identify the ellipsoidal drop collisions (for small eccentricities) from post-test examinations of the impact specimens. The photographic records of the actual collision in the ETI liquid drop impact facility affords the opportunity to quantify and correct these subtleties in the water drop impact conditions which have gone unnoticed in most liquid drop erosion studies.

An ellipsoidal drop will be considered equivalent to a spherical drop when they have the same mass. Hence, the equivalent drop radius is determined from the relation

$$r_o = \left( b_1^2 b_2 \right)^{1/3} . \quad (2.22)$$

The semi-axes of the elliptical cross section can be measured from the photograph of the drop prior to impact. The range of equivalent drop diameters in the liquid drop impact facility is currently 1.5 to 2.0 mm.

In view of the previous considerations the existing impact conditions in the liquid drop impact facility are approaching the idealized conditions represented in most modeling studies. Having well-documented individual water drop collisions is a significant advantage in any effort which attempts to characterize or model the damage produced in a material due to single or multiple liquid drop impacts.



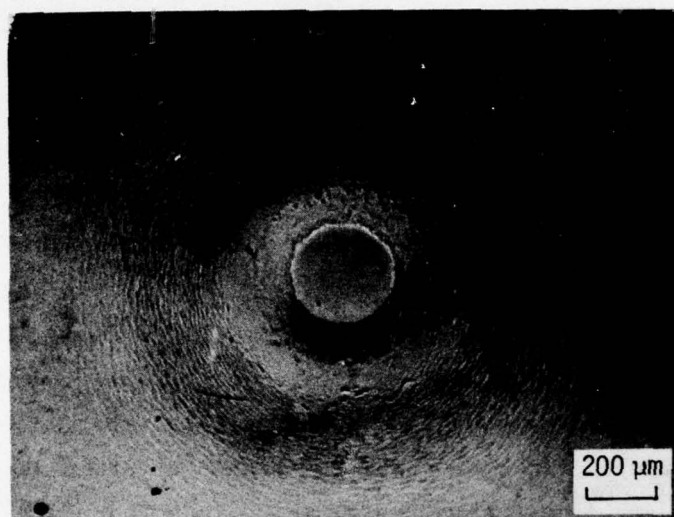
### 3.0 WATER DROP IMPACT ON POLYMETHYLMETHACRYLATE

Polymethylmethacrylate (PMMA) specimens were used to evaluate the perfection of the water drop impact damage and to detect if any recovery damage was being produced on the face of the specimen in the liquid drop impact facility. The recovery of PMMA from 200 to 700  $\text{ms}^{-1}$  presented no particular problems, however the recovery of fragile brittle and semi-brittle ceramics is considerably more challenging. During the initial and subsequent development of the recovery system, soda lime glass specimens were used in place of the test specimens. After successful shots were accomplished using soda lime glass, trials were carried out with the test materials. In most cases the single crystals were more susceptible to recovery damage than the glass. Since there are relatively few accounts of single water drop impacts on PMMA above 400  $\text{ms}^{-1}$ , the general character of the damage from 200 to 700  $\text{ms}^{-1}$  is of some interest.

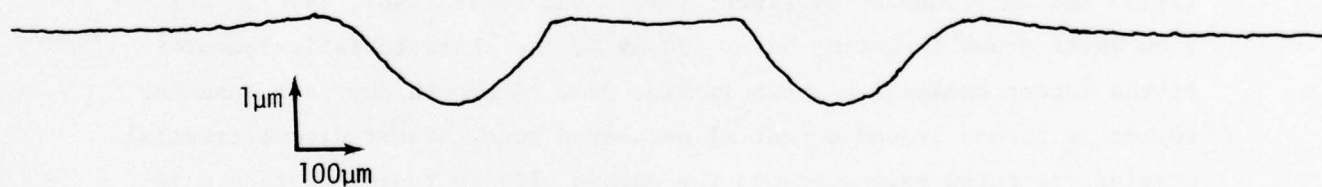
#### 3.1 RELATED OBSERVATIONS

Single water drop impacts on PMMA were first described by Engel (1955) and subsequently by Kinner (1967) and Fyall (1967, 1970). For 2 mm water drops impacting below 400  $\text{ms}^{-1}$ , the characteristic features of the impact damage are shown in Fig. 3.1. A smooth depressed annular region is formed around a central undamaged zone. Short circumferential crazing fractures extend beyond the damage site to radial distances in excess of the radius of the impacting drop. The now familiar surface contour of the impacted specimen appears as shown in the profilometer trace in Fig. 3.1.

A general description of the damage produced by water drop impacts on PMMA at low impact velocities has been provided by Adler and Hooker (1978). Descriptions of liquid impact on PMMA over an extended velocity range have been given by Brunton (Bowden and Brunton, 1961; Brunton, 1966). These observations are derived from water jet impacts rather than water drop collisions and are quite general.



Photographed with oblique polarized illumination.



Surface contour along midplane of damage site.

Figure 3.1. Characteristic Water Drop Impact on PMMA.  
1.5 mm Water Drop Impacting at  $356 \text{ ms}^{-1}$ .

The water jet was developed at the University of Cambridge during the late fifties as a useful laboratory device for evaluating the effects of water impacts on materials. The correspondence between the loading imparted to a surface by a water jet and by a spherical drop was considered in the initial paper on this subject (Bowden and Brunton, 1961); the correspondence has been strengthened within the last few years (Field, et al., 1976, 1979). Empirical correlations have now been developed based on the similarities in the impact damage produced by water jets and equivalent sized water drops. It is hypothesized that the initial water hammer pressure in both cases controls the amount of damage. Thus damage extension during the period of lateral outflow is taken to be relatively small and not significantly different for a water drop and water jet over a velocity range from 200 to 400  $\text{ms}^{-1}$ .

The water jet impact experiments indicated that the depressed annular region in PMMA was replaced by a ring crack at impact velocities of 450 to 500  $\text{ms}^{-1}$  (Bowden and Brunton, 1961; Brunton, 1966). The water jet conditions used at this time would correspond to water drops on the order of 10 to 50 mm according to Field's correlations. Prior to the occurrence of the ring fracture, fractures could be seen below the depressed annulus which are similar to those forming the ring fracture at higher velocities. These fractures cut the surface to form small hair-line cracks within the annular region and reached depths of 500  $\mu\text{m}$ .

Outside this region a high concentration of short circumferential crazing fractures are observed on the specimen's surface. The outer faces of these fractures just outside the depressed annulus are uplifted by about 0.2  $\mu\text{m}$ . These fractures are susceptible to lateral outflow jetting from the collapsing jet. This interaction results in small pits on the surface of the specimen which Brunton conjectures are responsible for the pitted appearance of the annular zone at higher impact velocities. At approximately 600  $\text{ms}^{-1}$  a star-shaped crack develops beneath the surface in the vicinity of the axis of symmetry. The fracture surfaces



follow the shear trajectories. According to Brunton as the impact velocity is increased further, the ring fracture widens and deepens and eventually joins with the subsurface star fracture at a velocity of  $900 \text{ ms}^{-1}$ .

Lankford, et al. (1973) used PMMA as a control material in their investigations of water drop impacts on radome materials at low Mach numbers. They made a cursory examination of the damage at 300 to  $760 \text{ ms}^{-1}$  using 1 to 2 mm water drops in a ballistic range configuration. The characteristic depressed annulus was observed for velocities below  $450 \text{ ms}^{-1}$ , but a transition in the form of the damage took place for impact velocities from 450 to  $500 \text{ ms}^{-1}$ . Above  $500 \text{ ms}^{-1}$  Lankford and co-workers noted that the annular depressed zone no longer appeared, but significant subsurface cracking became evident with occasional small dents or depressions on the surface. No micrographs are shown of the damage for this velocity range; only a sketch of the subsurface damage is provided which is reproduced in Fig. 3.2. The dents occurring in the annular region are difficult to explain. The subsurface cracks are shown as penetrating normal to the surface. Lankford and co-workers noted that the cracked regions at the higher velocities appeared slightly smaller in diameter in some cases than the depressed annular zone occurring at velocities just below the transition velocity.

A brief account of water drop impacts on PMMA in a whirling arm facility is provided by Behrendt (1974) for impact velocities from 400 to  $700 \text{ ms}^{-1}$ . These tests were carried out using 1.2 mm water drops at ambient pressures in the range from 6 to 18 torr. The micrographs show an elliptical undamaged zone with a dominant cone fracture penetrating the bulk of the specimen just outside this zone. The illumination used does not show the conditions on the surface of the specimen. An annular rippled zone of irregular width is seen at  $600 \text{ ms}^{-1}$  and significant removal of material particles from the surface is evident at  $700 \text{ ms}^{-1}$ . The author states that the undamaged zone is experiencing plastic

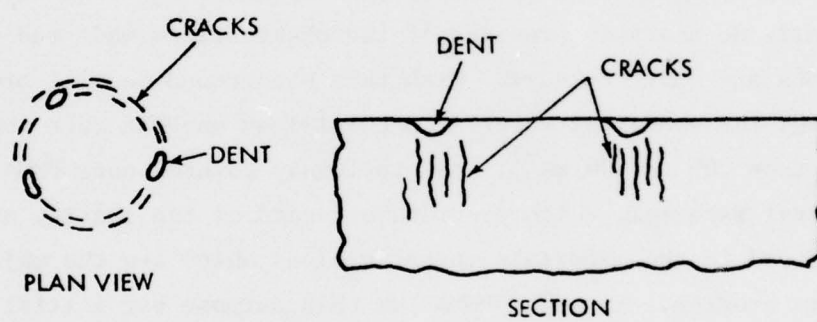


Figure 3.2. Form of Circumferential Fractures  
Described by Lankford, et al. (1973).

deformation at  $700 \text{ ms}^{-1}$ . The general character and lack of symmetry of the damage indicates that the drops are undergoing distortion prior to impact and may also be changing their composition during the time they are exposed to the low pressure in the test chamber.

It is to be noted that neither Lankford's nor Behrendt's experiments produced the central star-shaped subsurface damage associated with Brunton's water jet impacts.

While the characteristic surface deformation of PMMA shown in Fig. 3.1 is well established for low velocity impacts, significant differences are found in the form of the water impact damage on PMMA reported by several investigators at impact velocities above  $400 \text{ ms}^{-1}$ . It is also our observation on the basis of this review that there has been virtually no analysis provided of the observations made and the reported accounts are quite cursory. With this background we will present our findings for spherical water drop collisions on PMMA over the velocity range from 200 to  $700 \text{ ms}^{-1}$ . As previously pointed out, PMMA was used as a control material, which provided a record of the quality of the water drops used in the materials investigations which are the major concern of this program. In using PMMA for this purpose our initial evaluations of the impact damage was quite superficial. However during the course of obtaining higher velocity impacts the variation in the previously reported results became evident and it seemed worthwhile to report our microscopic observations of the higher velocity damage. A moderately detailed account of the deformation and fracture of PMMA due to spherical water drops is summarized in the next section.



### 3.2 EXPERIMENTAL RESULTS AND DISCUSSION

No special specimen preparation was undertaken for this investigation; the specimens were simply cut from sheets of Rohm and Haas Plexiglas G ranging from 6 to 12 mm thick. In some cases the surface was cleaned with methanol. The damage produced in PMMA by single water drop collisions impacting at velocities ranging from 200 to 700  $\text{ms}^{-1}$  will be described for water drop diameters ranging from 1.5 to 2.0 mm.

The essential features of the water drop impacts below 400  $\text{ms}^{-1}$  are as shown in Fig. 3.1. Measurements of the radii of the depressed annulus have been taken by Kinner (1967), Rickerby (1977), and Hackworth and Kocher (1977). The first two investigations used a gas gun to propel a sabot into a suspended drop while Hackworth and Kocher used a single drop generator in a rotating arm facility. These measurements are summarized in Fig. 3.3. Rickerby's data, as reported by Field, et al. (1979), is normalized with respect to the drop diameter, however according to Hackworth and Kocher's measurements the normalized inner and outer radii of the depressed annulus for 0.7, 2.0 and 2.5 mm water drop impacts at 222  $\text{ms}^{-1}$  are not constant but decrease by a factor of two as the drop diameter increases from 0.7 to 2.5 mm as seen in Fig. 3.3. The measurements made by Kinner and Rickerby were obtained from profilometer traces, whereas the measurements reported by Hackworth and Kocher were derived from microscope examination of the specimen's surface. While a fairly accurate measurement of the boundary of the undamaged central zone can be made with an optical microscope, determination of the outer radius of the depressed annulus presents a significant level of uncertainty using this method. Additional uncertainty arises in conjunction with not knowing the actual diameter of the drop which impacts the specimen.

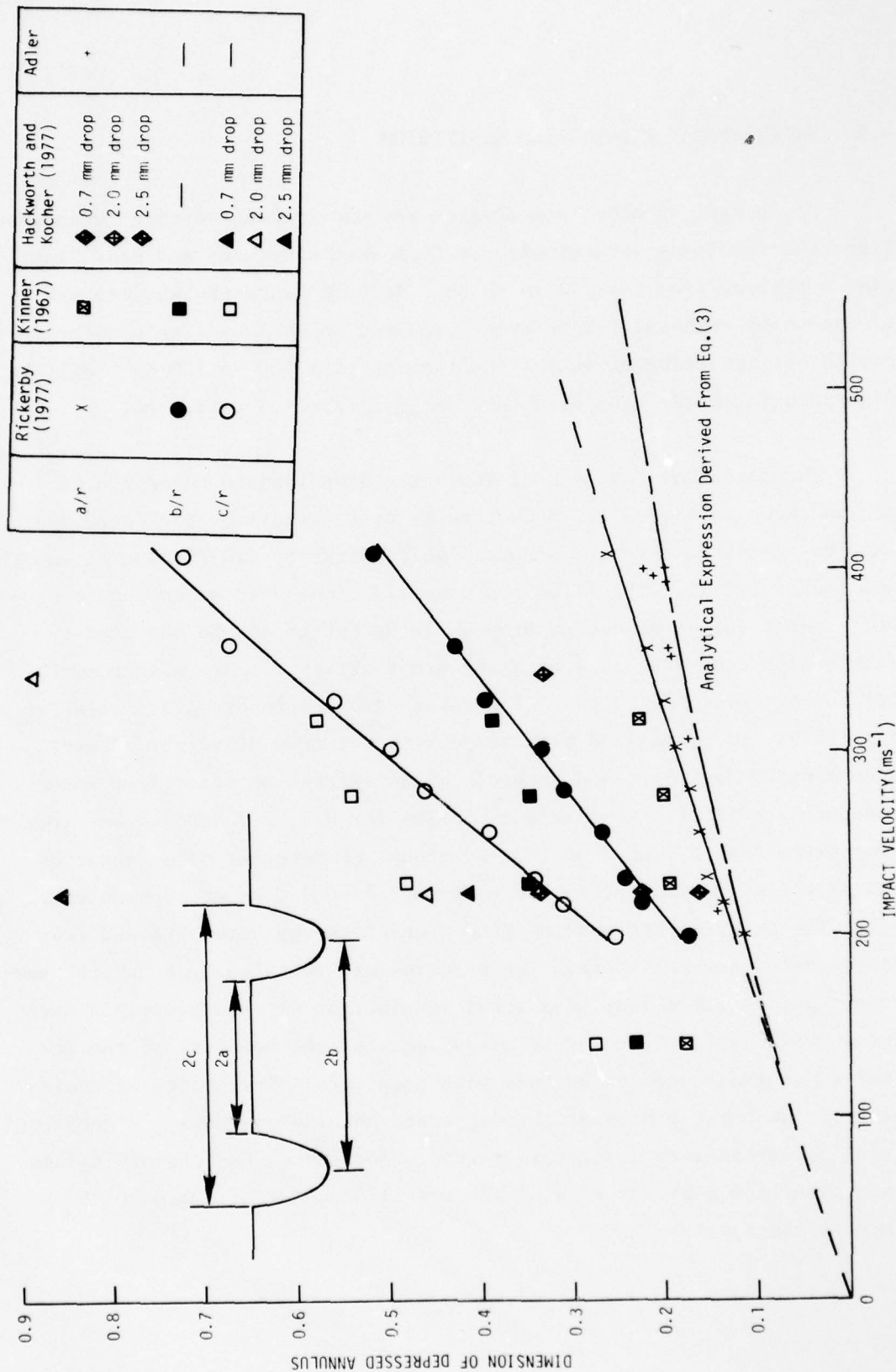


Figure 3.3. Summary of Experimental Values of the Characteristic Dimensions for Depressed Annulus on PMMA Due to Water Drop Impacts.

The trend in the experimental values for the diameter of the central undamaged zone shown in Fig. 3.3 will be compared with kinematic considerations for water drop impacts on PMMA. A reasonable approximation to the expansion of the contact surface between an impacting drop and a rigid plane is

$$a(t) = \sqrt{2rv_o t - (v_o t)^2} \quad (3.1)$$

where  $a$  is the instantaneous radius of contact zone,  $v_o$  is the impact velocity,  $r$  is the radius of the spherical drop, and  $t$  is the time elapsed from the initial contact. The rate at which the contact area expands, neglecting any change in the velocity of approach between the drop and the solid is,

$$\dot{a}(t) = \frac{v_o (r - v_o t)}{a(t)} \quad (3.2)$$

This velocity decreases monotonically with time. It will be assumed that the water drop loads the surface until the velocity of the contact zone equals the shock velocity,  $U_w$ , in the drop which initiates release of the pressure loading. Thus the critical value of the contact radius,  $a_c$ , is determined from the relation

$$\dot{a}_c = U_w$$

which leads to the result that (Adler, 1979)

$$\frac{a_c}{r_o} = \frac{v_o}{U_w} \left[ \frac{1}{1 + (v_o/U_w)^2} \right]^{1/2} \quad (3.4)$$

The shock velocity for water can be approximated by (Heymann, 1968)

$$U_w = 1.5 + 2 v_w \quad (3.5)$$



where  $v_w$  is the particle velocity. If the water drop was impacting a rigid plane,  $v_w$  would equal  $v_o$ . However the target material is not rigid but deformable. The value of  $v_w$  can be determined graphically using Schuler's (1970) shock data for PMMA which is applicable to water drop impacts through  $700 \text{ ms}^{-1}$ . The graphical method provides a solution to the equations

$$P_w = \rho_w U_w v_w = \rho_t U_t v_t = P_t \quad (3.6)$$

$$v_w + v_t = v_o \quad (3.7)$$

where the subscripts  $w, t$  refer to the water drop and the target, respectively.  $P$  denotes pressure and  $\rho$  the density. The graphical evaluation of Eq.(3.6) and (3.7) for an impact velocity of  $700 \text{ ms}^{-1}$  is shown in Fig. 3.4 to illustrate the method used. Now that  $v_w$  can be obtained, Eq.(3.4) can be evaluated using Eq.(3.5). The resulting curve for  $a_c$  is plotted in Fig. 3.3.

Field, et al. (1979), demonstrated that Rickerby's experimental measurements of the central undamaged zone,  $2a$ , were approximated by the condition

$$\dot{a}_c^2 = U_w^2 + v_o^2, \quad (3.8)$$

as originally proposed by Bowden and Field (1964), and argue that the experimentally determined radii are invariably larger than the computed values. When the compressibility of the target is taken into account, the values of  $a_c$  determined from Eq.(3.8) are only slightly higher than those found from Eq.(3.3) for impact velocities below  $700 \text{ ms}^{-1}$  (Adler, 1979).

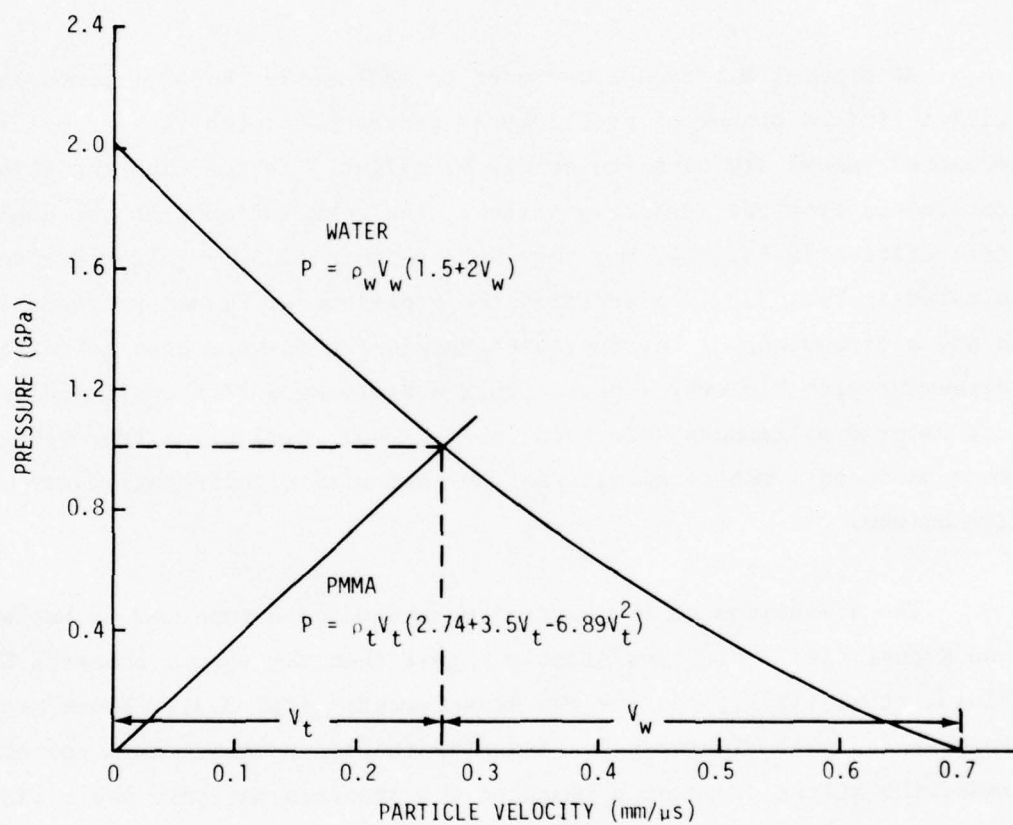


Figure 3.4. Graphical Evaluation of Impact Pressure and Particle Velocities for a Water Impact on PMMA at 700 ms<sup>-1</sup>.

The dimensions of the central undamaged zone determined from our experiments are compared in Fig. 3.3 with the analytical predictions. These measurements are seen to fall slightly below the values obtained by Rickerby and conform more closely to the nonlinear relation obtained from either Eq.(3.3) or (3.8). The close agreement with Rickerby's experimental data is encouraging, as is the correlation with the analytical relations.

An optical microscope was used to measure  $2a$ , however comparisons with a limited number of profilometer traces indicated the optically measured values are equal to or may be slightly larger than the values determined from the surface profiles. The correlation with the analytical relation in Eq.(3.4) may thus be even more closely followed than indicated in Fig. 3.3. In addition the profilometer traces provided the  $b$  and  $c$  dimensions of the depressed annulus which were also in reasonable agreement with Rickerby's data. Only measurements from confirmed spherical water drop impacts were used in Fig. 3.3. Deviations from spherical form produced symmetrical deformations but with significantly increased dimensions.

The dimensions of the central undamaged zone reported by Hackworth and Kocher (1977) are consistently higher than the values reported by Field, et al (1979), and our own measurements (Fig. 3.3). There are many sources for this discrepancy. Assuming the measurements were correctly made, the actual drop which impacted the specimen may have had a diameter different than the mean value determined from static measurements, since no direct measurement of the impacting drop is made in the whirling arm facility. If this is the case, the necessity for having a photographic record of the drop prior to impact for single drop impact experiments is amply demonstrated. Another explanation is that the drop was not spherical when it impacted due to drop distortion as it passed through the inviscid air layer in front of the specimen. Thus the critical undamaged zone corresponds to a much larger drop than assumed by Hackworth and

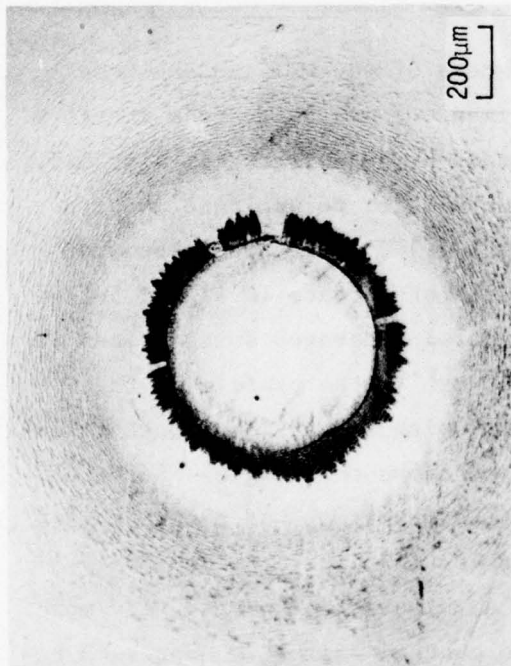


Kocher for the whirling arm test configuration. According to the analysis provided in Section 2.3.1 the drop distortion increases with decreasing drop diameter (Fig. 2.8 and 2.9), so the trend with respect to drop size in Fig. 3.3 appears reasonable.

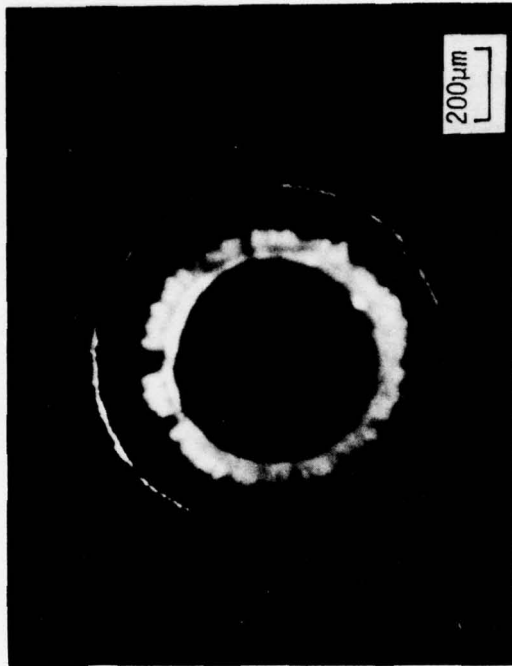
Kinner's (1967) measurements are normalized with respect to a nominal 2 mm drop diameter, since no measurements of the drop sizes are cited in his paper. The drop diameters may have deviated from the nominal dimension.

The primary transitions in the character of the damage site for velocities above  $400 \text{ ms}^{-1}$  are shown in Fig. 3.5 to 3.7 along with representative surface profiles. A circumferential ring fracture and subsurface ring fracture are characteristic of the higher impact velocity. Thus  $400 \text{ ms}^{-1}$  becomes a transition velocity between purely deformational response and fracture (although our subsequent discussion will show this may only be true in a restricted sense).

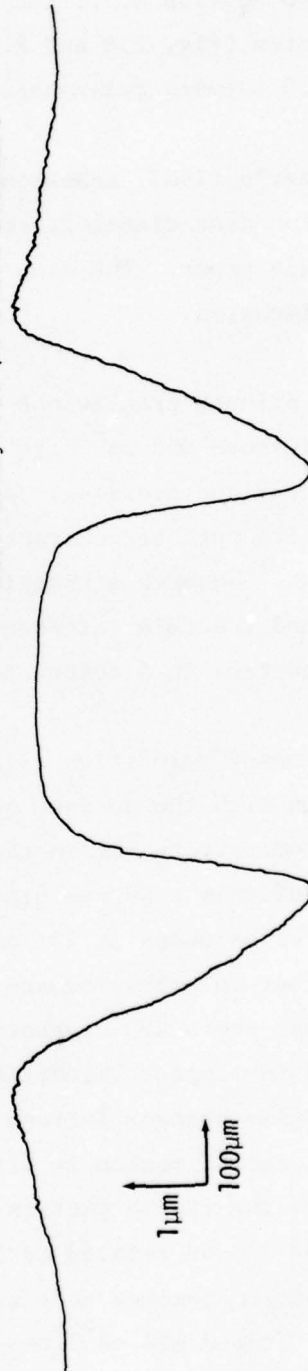
At impact velocities slightly in excess of  $400 \text{ ms}^{-1}$  an enhanced interaction with the surface of the specimen becomes evident in the form of a rippled pattern within the annular zone as illustrated in Fig. 3.5. A pattern of this type was previously observed for polysulfone impacted by 1.8 mm water drops at  $222 \text{ ms}^{-1}$  (Adler, 1977) and seen to a somewhat lesser extent on polycarbonate. The profilometer trace in Fig. 3.5c indicates that the sharp boundary of the central undamaged zone is less pronounced for impact velocities above  $400 \text{ ms}^{-1}$ : the profile of the central region becomes increasingly rounded with increasing impact velocity. The central region is slightly raised above the original surface elevation. The ripple pattern occurs on the outer wall of the depressed annulus and can be related to lateral outflow jetting. The intensity of the interaction becomes more severe as the velocity increases. At impact velocities around  $600 \text{ ms}^{-1}$  the top of the central region is depressed below the undeformed surface of the specimen as seen from the profilometer trace in Fig. 3.7b. The increasing dimensions of the damage site are evident in Fig. 3.5 to 3.7.



a. Bright field illumination showing surface features.

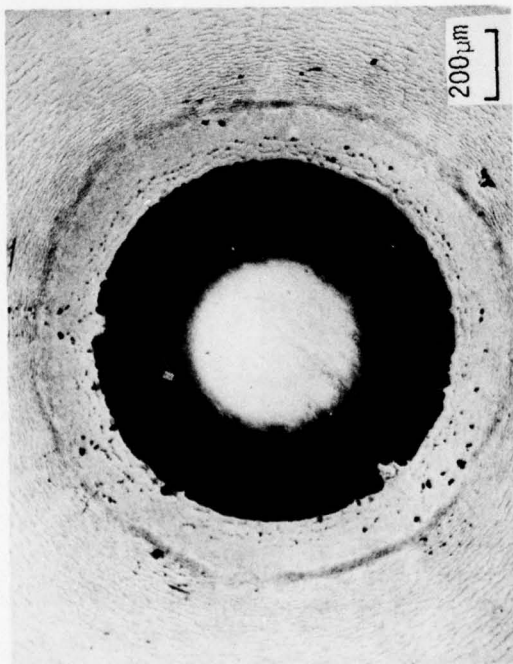


b. Transmitted light illumination passing through side of specimen. Focused at subsurface fracture array 280 μm below surface.



c. Surface contour along midplane of damage site.

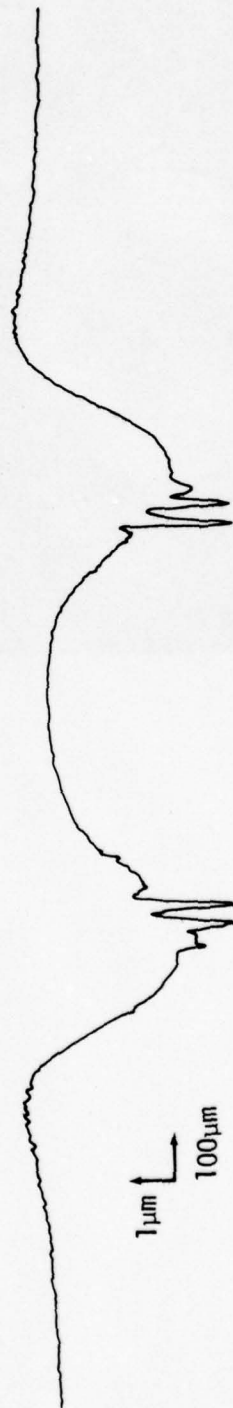
Figure 3.5. 1.6 mm Water Drop Impacting at 476 ms<sup>-1</sup>.



a. Bright field illumination showing surface features. Ring around damage site is due to subsurface fracture array.



b. Side transmitted light illumination. Focused at surface. Overexposed ring at interior of ripple pattern is due to surface ring fracture.

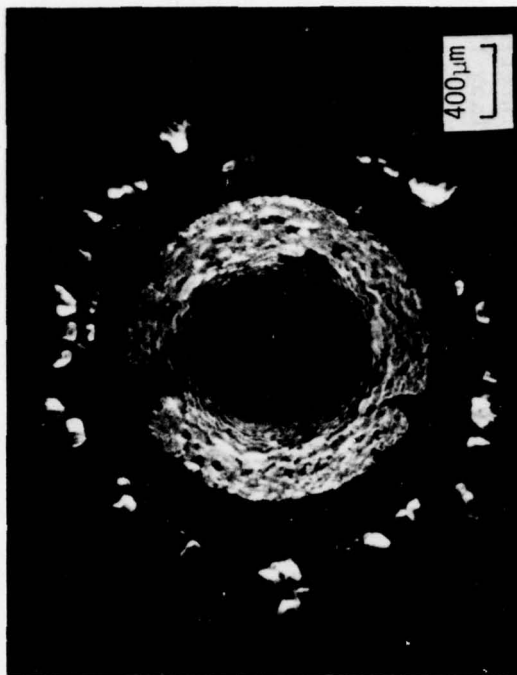


c. Surface contour along midplane of damage site.

Figure 3.6. 1.6 mm Water Drop Impacting at  $520 \text{ ms}^{-1}$ .



a. Side transmitted light illumination of central damage zone.



b. Surface contour along midplane of damage site.

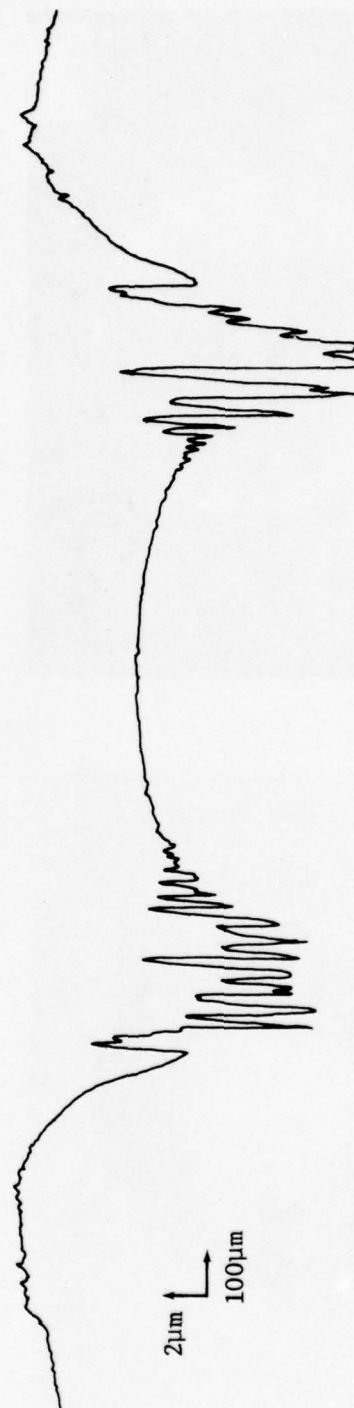


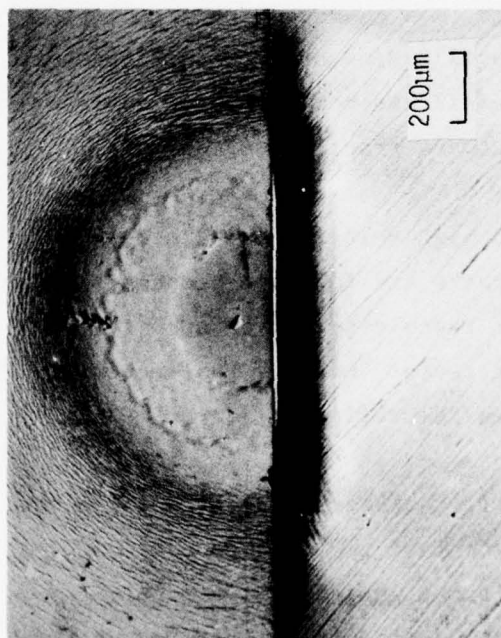
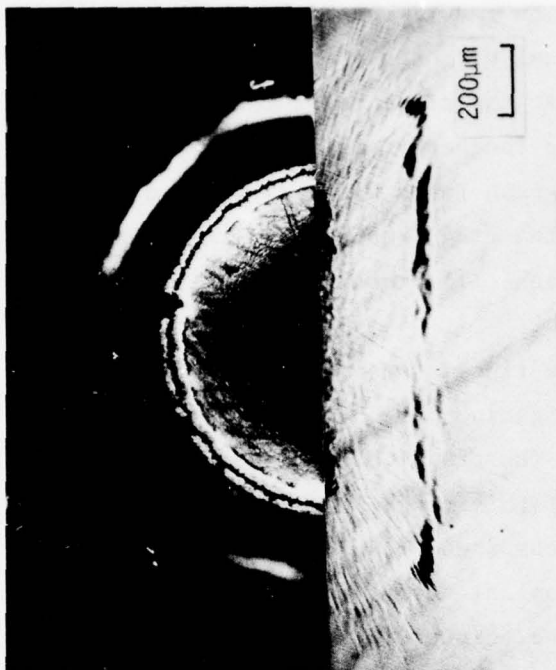
Figure 3.7. 1.9 mm Water Drop Impacting at  $660 \text{ ms}^{-1}$ .

An isolated circumferential ring fracture develops for impact velocities greater than  $450 \text{ ms}^{-1}$  which is readily observed when viewing the surface of the specimen in an optical microscope as shown in Fig. 3.5a. As the impact velocities increase the presence of the circumferential ring fracture is obscured in the roughened annulus. The bright ring which is overexposed in the micrograph taken with transmitted light in Fig. 3.6b indicates the location of the ring fracture for this case which is not as obvious in reflected light illumination.

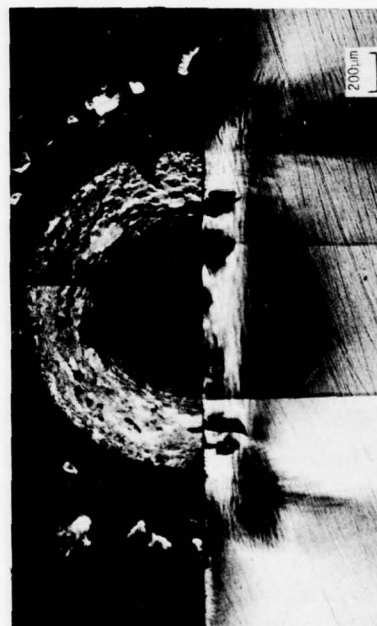
In addition a distinct subsurface ring is seen surrounding the central damage pattern. Transmitted lighting parallel to the impact face was used to enhance this effect. The transmitted light micrograph in Fig. 3.5a is focused at the level of this ring. Detailed examinations of these rings indicate that they are composed of a series of short fracture segments arrayed on a truncated conical surface which expands outward from the impact zone. At impact velocities in excess of  $600 \text{ ms}^{-1}$ , the fractures could be seen to be short circumferential segments approximately  $5 \mu\text{m}$  long lying in planes parallel to the specimen's surface. Several isolated fractures were observed in high intensity transmitted light away from the main clusters but still lying on a conical surface. However below  $600 \text{ ms}^{-1}$  this level of detail was not possible, apparently due to the short separation distance between fracture segments.

Several specimens spanning low to high velocity impacts were sectioned. The circumferential ring cracks are found to propagate normal to the specimen's surface. The ends of these cracks are found to curve both outward and inward from the impact center, however the mechanism controlling this effect has not yet been identified.

The details of the deformation patterns seen in cross section are difficult to photograph in sufficient contrast to yield good reproductions, however some representative deformation and fracture patterns are shown in Fig. 3.8. The details of the deformation patterns which



a. 1.75 mm water drop impacting at  $394 \text{ ms}^{-1}$ . b. 1.6 mm water drop impacting at  $520 \text{ ms}^{-1}$ .



c. 1.9 mm water drop impacting at  $660 \text{ ms}^{-1}$ .

Figure 3.8. Subsurface Deformation and Fracture on Cross Sections of PMMA Specimens as a Function of Impact Velocity.



evolve after integrating microscope observations using various lighting conditions and incremental focusing cannot be adequately portrayed in a single micrograph. The descriptions provided are based on these observations.

The characteristic deformation pattern seen in Fig. 3.8a is observed at all impact velocities. The inner boundary tends to form a truncated conical boundary originating at the periphery of the central undamaged zone for the low velocity collisions. The outer boundary is a curved surface which increases in depth below the impact face with increasing radial distance. The subsurface fracture rings are located at the periphery of the distinct interface between the deformation zone and the central conical region (Fig. 3.8b). A second set of deformation trajectories which are approximately orthogonal to the initial array could be discerned for impact velocities greater than  $600 \text{ ms}^{-1}$ . An example is shown in Fig. 3.8c. In addition the higher velocity impacts produced a more complex fracture array which includes the subsurface fractures in Fig. 3.8b as well as an even greater fracture concentration at a depth intermediate to the initial subsurface fractures and the impact face. These fractures are oriented essentially parallel to the surface and do not conform to the orientation of the local deformation pattern, although in some specimens a third deformation pattern with the indicated fracture orientation is seen superposed onto the more prevalent patterns.

A noteworthy effect associated with this investigation is that when the specimens are thinned below a certain level, still greater than the diameter of the visible damage site, the deformation patterns and subsurface fractures completely disappear. The stressed regions no longer appear using transmitted polarized light. The features observed above are thus associated with the residual elastic stress state in the impacted material. This observation would imply that there may be additional damage which is not readily observable. In particular there may be significantly more subsurface crazing than is evident in the post-test examinations.

Typical depths and radii for the fractures described above are listed in Table 3.1. The profilometer traces and sectioned specimens represented in Fig. 3.5 to 3.8 show that the surface circumferential crack is located at the bottom of the depressed annulus regions (at a radius  $b$  from the impact point) and the subsurface circumferential crazing which is visible occurs at a radial dimension quite close to  $c$  (as defined in the insert in Fig. 3.3).

On the basis of the measurements listed in Table 3.1 it appears that these fractures occur initially at depths on the order of  $200\text{ }\mu\text{m}$  below the surface. A question arises as to what precedes the development of these fractures at impact velocities below the observed fracture threshold. The precursor to these fractures is conjectured to be related to the deformation marking which can be seen in the depressed annulus as shown in Fig. 3.9. The image of a thin ring of deformed material is typically observed within the depressed annulus surrounding the central undamaged zone for impacts below  $400\text{ ms}^{-1}$ . As the impact velocity approaches and exceeds  $400\text{ ms}^{-1}$  the deformation marking is not seen when the microscope is focused on the surface. However the deformation marking becomes apparent by focusing the optical microscope from 20 to  $100\text{ }\mu\text{m}$  below the surface: the greater depth being associated with the higher velocities. This effect is demonstrated in Fig. 3.10. The perfection of this deformation pattern is occasionally disrupted by inclusions in the material: Fig. 3.10 being an extreme example. It is hypothesized that the subsurface ring fracture (crazes) then form at the periphery of the subsurface deformation cone when a critical stress level is reached. The proposed sequence of events leading to visible subsurface crazing is highly speculative and requires substantiation.

Higher magnification microscope examinations of the specimens impacted at greater than  $500\text{ ms}^{-1}$  show evidence of occasional short radial fractures exterior to the ripple pattern zone. The significance of the radial fractures requires clarification, since radial fractures also tend

Table 3.1. Representative Dimensions Associated with Surface and Subsurface Circumferential Fractures.

IMPACT VELOCITY ( $\text{ms}^{-1}$ )	DROP DIAMETER (mm)	SURFACE RING CRACK		SUBSURFACE RING CRACK	
		DIAMETER (mm)	PENETRATION DEPTH (mm)	DIAMETER (mm)	LOCATION BELOW SURFACE (mm)
476	1.62	0.59	0.05	0.98	0.27
512	1.66	.77	.10	1.17	.36
520	1.62	.87	.10	1.38	.33
665	1.90	1.24	.22	2.08	.40*
685	1.80	1.08	.25	2.20	.55**

\* Intermediate fractures are dominant and are formed at a mean depth of 0.20 mm.

\*\* Concentration of intermediate fractures also present at a mean depth of 0.27 mm.



Deformation marking on surface  
in the annular depressed zone.

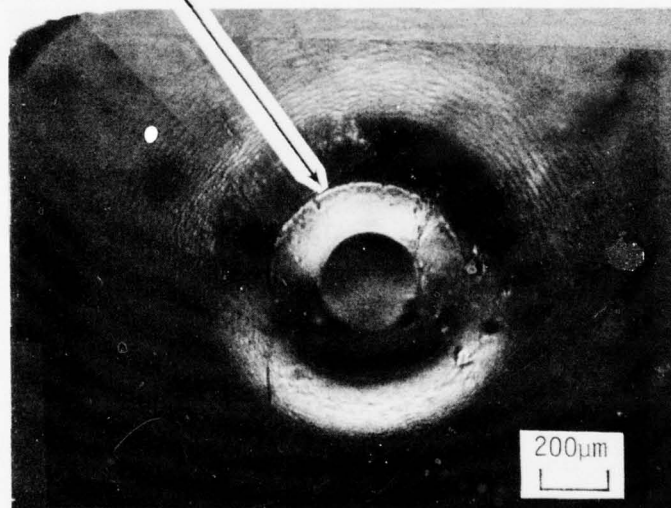
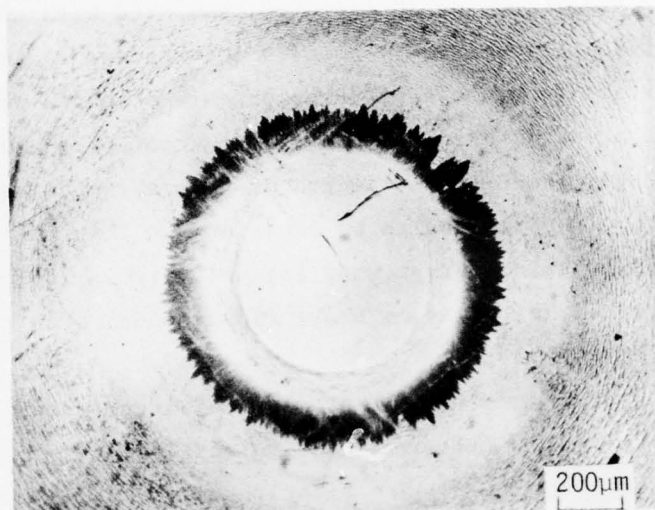
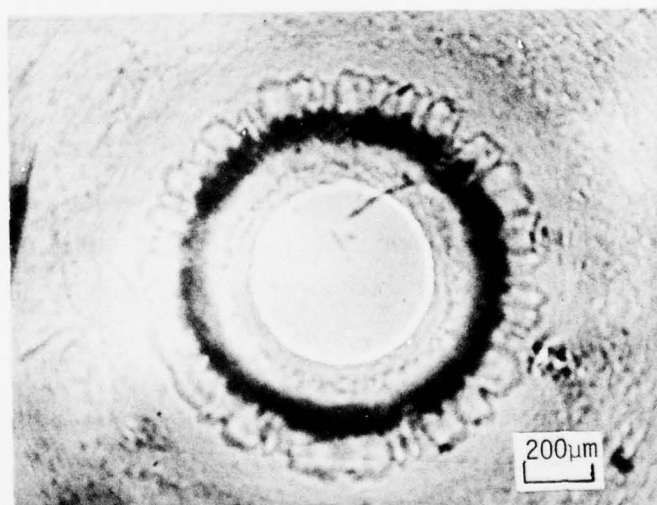


Figure 3.9. Characteristic Water Drop Impact  
on PMMA at  $300 \text{ ms}^{-1}$  Showing  
Deformation Marking Usually Present.



(a) Focused on Surface



(b) Focused 100  $\mu\text{m}$  Below Surface

Figure 3.10. 1.8 mm Water Drop Impact on PMMA at  $390 \text{ ms}^{-1}$ .  
Water Drop Was Considerably Flattened Before Impact.

to form where there is an imbalance in the local stress conditions, due possibly to very small bubbles in the drop, compared with an idealized axisymmetric stress distribution. However interesting radial and circumferential surface fracture configurations are obtained when the impacted specimens are etched in acetone. The extent of the fractures which appear are dependent on the length of time the specimen remains in an acetone bath, so caution has to be exercised so that the impact-induced fractures are differentiated from what may be a stress corrosion effect. The results described are based on short (10 seconds) etch durations.

The etching procedure shows that surface circumferential fractures are formed over the full range of impact velocities. At the lower velocities these fractures apparently are tightly sealed and have relatively shallow depths. It is not until a velocity of  $450 \text{ ms}^{-1}$  is reached (Fig. 3.5) that the fractures become large enough to be seen with an optical microscope. Above this velocity a dominant single circumferential fracture develops. The etched surfaces also reveal that two concentric surface ring cracks are formed at impact velocities below this level: one located near the bottom of the depressed annulus and the second at the outer periphery of the depressed annulus. A second surface ring crack at the periphery of the depressed zone is also evident for the higher velocity impacts. A small number of radial fractures interconnect the two concentric rings and a greater number of radial fractures propagate outward from the second (unseen) circumferential fracture for the higher velocity impacts.

The fracture patterns which have been observed in PMMA are interesting on their own as well as the insights they may provide with respect to the water drop impact response for other materials.



#### 4.0 WATER DROP IMPACTS ON SINGLE CRYSTALS

The investigations to date have concentrated on the crystallographic mechanisms for damage initiation due to single water drop impacts and spherical solid particles. Most of the specimens used in this study were polished to acceptable optical tolerances. However residual grinding flaws and other induced defects are of major importance for damage initiation in a rain environment. For subsonic impact velocities these sites influence the erosion process in most of the crystals examined which have a higher tolerance for crystallographic fractures. Procedures to control the extent of grinding damage and other non-crystallographic defects may greatly enhance the rain erosion resistance up through low supersonic velocities for the crystals considered here.

The observed impact damage close to the fracture initiation threshold displays a strong dependence on the surface finish, but as the impact velocity increases significantly beyond these levels this dependence is of lesser importance. Thus, in order to investigate the actual material response near the fracture threshold, it became essential to have adequately prepared surfaces. These requirements have become evident during the course of this program.

A number of ceramic materials received water drop impacts, however detailed investigations of the material response have focused on single crystals of magnesium oxide ( $\text{MgO}$ ), calcium fluoride ( $\text{CaF}_2$ ), and lithium fluoride ( $\text{LiF}$ ). A partial listing of the material properties relevant to their particle impact response is provided in Table 4.1. The water drop impact experiments carried out on these materials are summarized in Table 4.2. All of the specimens of  $\text{MgO}$  and  $\text{LiF}$  were impacted on a (100) plane.

Table 4.1. Properties of Single Crystals.

	MgO	LiF	CaF <sub>2</sub>
Crystal Structure	Rock Salt	Rock Salt	Fluorspar
Density (g/cc)	3.58	2.60	3.18
Elastic Constants (GPa)			
$C_{11}$	287	111	166
$C_{12}$	88	42	49
$C_{44}$	154	63	36
Wave Velocity in <100> Direction (mm/ $\mu$ s)			
$C_{\ell}$	8.96	6.53	7.22
$C_s$	6.56	4.92	3.36
Knoop Hardness			
(001) <100>	400	87-96	178
(001) <110>	780-800	93-103	157
(110) <001>	420	87-98	---
(1 $\bar{1}$ 0) <1 $\bar{1}$ 1>	930	97-120	---
(110) <1 $\bar{1}$ 0>	810	93-116	---
Slip System	{110} <1 $\bar{1}$ 0>	{110} <1 $\bar{1}$ 0>	{100} <011>
Cleavage Plane	{100}	{100}	{111}
Water Solubility (mg/100g H <sub>2</sub> O)	.62	270	1.31

Table 4.2. Water Drop Impacts on Single Crystals.

SHOT NO.	MATERIAL	IMPACT VELOCITY ( $\text{ms}^{-1}$ )	EQUIVALENT DROP Diameter (mm)	$\frac{b_1}{b_2}$	PRESSURE (torr)	REMARKS
583	MgO	276	1.68	1.12	0.20	
415	MgO	366	1.38	--	0.40	
586	MgO	415	1.67	1.04	0.20	
465	MgO	433	1.88	1.12	0.50	
587	MgO	441	1.60	1.04	0.20	
590	MgO	459	1.56	1.00	0.20	
592	MgO	510	1.56	1.00	0.25	
633	MgO	610	1.68	1.00	0.50	
658	MgO	679	1.65	1.00	0.40	
983	MgO	328	1.60	1.00	0.10	
945	MgO	397	1.62	1.00	0.10	
896	MgO	400	1.25	1.15	0.20	
858	MgO	413	1.68	1.00	0.20	
979	MgO	512	--	--	0.10	
777	MgO	555	1.55	1.21	0.30	
809	MgO	556	1.43	1.41	0.30	
953	MgO	563	1.68	1.00	0.10	
952	MgO	568	1.71	1.00	0.10	
1010	MgO	574	1.63	1.00	0.10	
807	MgO	672	1.82	1.21	0.30	
792	MgO	684	1.43	1.45	0.30	
793	MgO	696	1.32	1.26	0.25	
808	MgO	722	1.69	1.17	0.30	
460	$\text{CaF}_2(111)$	272	1.75	1.60	0.50	
462	$\text{CaF}_2(111)$	281	1.81	1.45	0.50	
516	$\text{CaF}_2(111)$	292	1.85	1.27	0.45	
626	$\text{CaF}_2(111)$	301	1.74	1.00	0.30	
621	$\text{CaF}_2(111)$	318	1.54	1.48	0.30	
517	$\text{CaF}_2(111)$	326	1.82	1.20	0.40	
629	$\text{CaF}_2(111)$	371	1.62	1.00	0.50	specimen fractured

Table 4.2. (continued)

SHOT NO.	MATERIAL	IMPACT VELOCITY ( $\text{ms}^{-1}$ )	EQUIVALENT DROP Diameter (mm)	$\frac{b_1}{b_2}$	PRESSURE (torr)	REMARKS
841	$\text{CaF}_2(111)$	304	1.86	--	0.30	
995	$\text{CaF}_2(111)$	307	1.31	1.00	0.10	
772	$\text{CaF}_2(111)$	312	1.58	1.53	0.30	
771	$\text{CaF}_2(111)$	318	1.68	--	0.30	
821	$\text{CaF}_2(111)$	367	1.50	--	0.30	
840	$\text{CaF}_2(111)$	385	1.83	2.10	0.50	
947	$\text{CaF}_2(111)$	404	1.71	1.00	0.10	
969	$\text{CaF}_2(111)$	510	1.71	1.00	0.10	
979	$\text{CaF}_2(111)$	521	1.71	1.00	0.10	
913	$\text{CaF}_2(111)$	523	1.68	1.00	0.20	
518	$\text{CaF}_2(100)$	290	1.82	1.20	0.45	
622	$\text{CaF}_2(100)$	305	1.63	1.20	0.30	specimen fractured
582	$\text{CaF}_2(100)$	306	1.72	1.16	0.40	specimen fractured
650	$\text{CaF}_2(100)$	317	1.63	1.70	0.40	
519	$\text{CaF}_2(100)$	331	1.82	1.20	0.30	specimen fractured
859	$\text{CaF}_2(100)$	334	1.72	1.15	0.20	
946	$\text{CaF}_2(100)$	402	1.68	1.00	0.10	
878	$\text{CaF}_2(100)$	458	1.70	1.23	0.25	
972	$\text{CaF}_2(100)$	506	--	--	0.10	
976	$\text{CaF}_2(100)$	508	1.71	1.00	0.10	
987	$\text{CaF}_2(100)$	528	1.54	1.00	0.10	
914	$\text{CaF}_2(100)$	546	1.62	1.00	0.07	
593	LiF	243	1.48	1.00	0.20	
591	LiF	247	1.65	1.32	0.20	
1002	LiF	209	1.37	1.00	0.10	
980	LiF	385	1.63	1.00	0.10	
886	LiF	497	1.15	1.30	0.22	
915	LiF	555	1.56	1.00	0.10	



Table 4.2. (concluded)

SHOT NO.	MATERIAL	IMPACT VELOCITY ( $\text{ms}^{-1}$ )	EQUIVALENT DROP Diameter (mm)	$\frac{b_1}{b_2}$	PRESSURE (torr)	REMARKS
520	Si(111)	291	1.78	1.29	0.40	specimen fractured
619	Si(111)	305	1.58	1.21	0.25	
458	Si(111)	313	1.70	1.43	0.50	
523	Si(111)	351	1.76	1.13	0.40	
522	Si(100)	290	1.71	2.00	0.40	specimen fractured
623	Si(100)	305	1.64		0.30	
637	Si(100)	352	1.51	--	0.40	
627	Si(100)	381	1.60	1.16	0.30	
521	Si(110)*	291	1.82	1.20	0.40	
620	Si(110)*	305	1.67	1.24	0.30	
651	Si(110)*	352	1.74	1.00	0.40	
624	Ge(111)	305	1.61	1.25	0.30	
* Si(110) was ordered, however Laue verification of the orientation indicated the impacted face is close to a (221) orientation.						

The water drop impacts listed in Table 4.2 were undertaken at various stages of the development of the liquid drop impact facility described in Section 2.2. Several comments will be made regarding the data summary in Table 4.2. Photographic records have been taken of the drop which strikes the specimen. However the initial procedure for obtaining this photograph was to specify the time delay for triggering the flash unit after the firing circuit was actuated. This procedure introduced a degree of arbitrariness in the location of the sabot traveling down the barrel relative to the position of the water drop. The present procedure for photographing the drop was incorporated into the system after shot no. 658. As indicated in Section 2.1 the drop is photographed when the sabot is less than 25 mm from the drop. The triggering of the flash unit can still be delayed so a record can be made when the sabot is close to the drop, however as pointed out in Section 2.3.1 the time increment the drop is exposed to the gas flow during this period is only a small fraction of the total exposure time. Thus the observed drop distortions should be representative of what they actually would be when the drop impacts the specimen. While the level of drop distortion is recorded in Table 4.2 (the ratio  $b_1/b_2$  as defined in Section 2.3.2) for the early records, they cannot be considered indicative of the actual level of distortion which may have occurred. The data obtained for each of these procedures is listed with respect to the impact velocity. The equivalent drop diameter is determined from Eq.(2.22).

The fracture threshold due to water drop impingement for the crystallographic orientations of  $\text{CaF}_2$  and Si was found to be in the vicinity of  $300 \text{ ms}^{-1}$  in all cases. It is seen from Table 4.2 that gross fracture of these crystals was prevalent in the initial tests for small increases in the impact velocity beyond the water drop fracture threshold. As stated in Section 2.2 this placed a somewhat severe limitation on the scope of the materials investigation. Considerable improvements were made in the recovery system as evidenced by the data recorded in Table 4.2 for shot numbers above 658.

A cursory examination of the data recorded in Table 4.2 which is becoming available for water drop impacts indicates that the fracture thresholds for  $\text{CaF}_2$  and Si occur at almost the same water drop impact condition: a 1.8 mm water drop impact at approximately  $300 \text{ ms}^{-1}$ . However the fracture surface energy of Si is about 2.5 times that of  $\text{CaF}_2$  and the Knoop hardness is approximately seven times greater. This result is somewhat unexpected and it is not known if the initial surface condition of the specimens alone could account for this difference. In actual fact the surface finish on this lot of  $\text{CaF}_2$  was extremely poor. Examples of comparable impact conditions are shown in Fig. 4.1 and 4.2.

It is also interesting to note the large dominantly  $\{111\}$  oriented cleavage cracks which occur in Si and Ge outside the central impact zone as illustrated in Fig. 4.1 and 4.3. It is obvious that these large cracks will have a deleterious effect on the erosion resistance of these materials.

Analyses of the stresses generated in a target material due to water drop impacts on single crystals is considerably more difficult than in the case of isotropic materials (Adler, 1979), so it is presently not possible to gain a realistic understanding of the dynamic stress distributions which may develop within a particular crystal structure. An estimate of these stress distributions for restricted crystallographic orientations has been described by Adler and Hooker (1977). This information is useful in establishing the temporal development of the damage sequence during the collision process. Even though this can only be done in a very approximate way, some consideration will be given to the temporal evolution of the final damage state in order to relate the impact damage to the available deformation and fracture models developed primarily for quasistatic loading conditions. The water drop impact damage on  $\text{MgO}$ ,  $\text{CaF}_2$ , and  $\text{LiF}$  single crystals will be described.

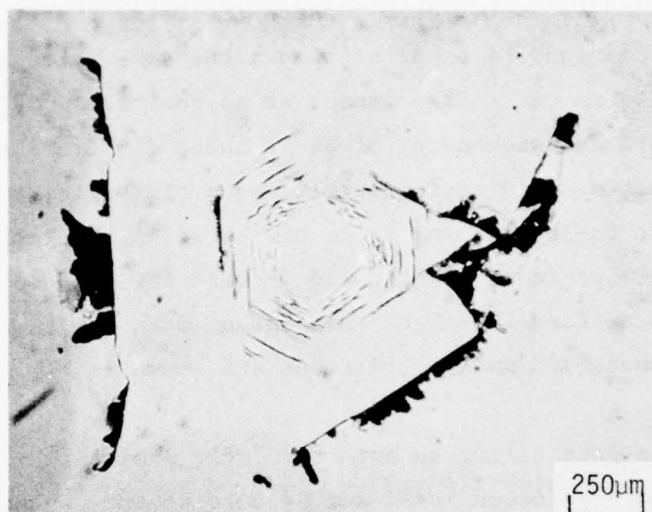


Figure 4.1. 1.70 mm Water Drop Impact on Si(111)  
at 313 ms<sup>-1</sup>.

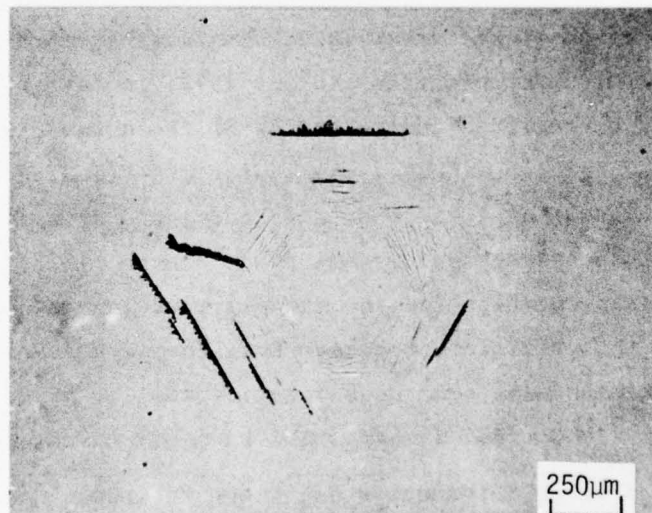


Figure 4.2. 1.82 mm Water Drop Impact on CaF<sub>2</sub> (111)  
at 326 ms<sup>-1</sup>.



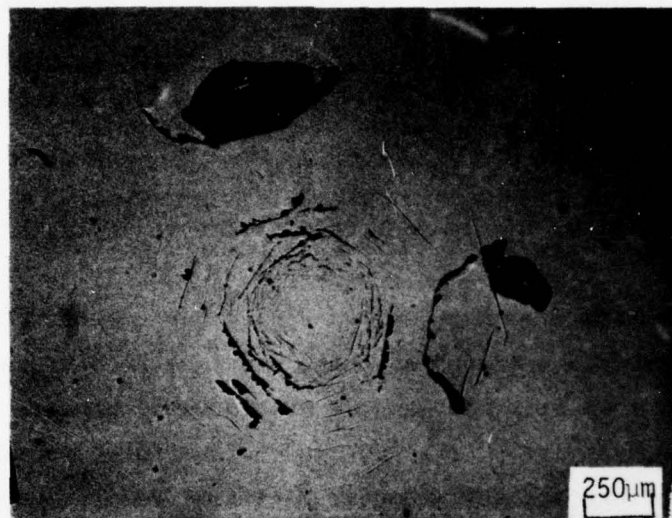


Figure 4.3. 1.61 mm Water Drop Impact on Ge(111)  
at 305 ms<sup>-1</sup>.

#### 4.1 MAGNESIUM OXIDE

Magnesium oxide (MgO) has been used as an irdome material particularly in the hot-pressed form (IRTRAN-5). The irdome and window applications of magnesium oxide are based upon its desirable properties: a high Knoop hardness number, large rupture modulus, insolubility in water, high thermal conductivity and good optical transmission from 0.3 to 6  $\mu\text{m}$  (Kruse, 1962).

MgO crystallizes in the rock salt structure which has cubic symmetry. Freshly cleaved single crystals of MgO are sufficiently ductile at room temperature that samples can be bent by hand (Gorum, et al., 1958). Flow stresses measured on these samples in the three-point bend configuration ranged from 20.7 to 103 MPa (Stokes, et al., 1959a, have measured similar values). It is concluded from this experiment that the surface dislocations are sufficiently mobile at room temperature to permit quasistatic macroscopic flow at stress levels of approximately 69 MPa. The observed deformation is based upon the slip mechanism in which dislocation bands are initiated at surface defects and then widen and propagate into the interior via active  $\{110\}\langle 110 \rangle$  slip systems. The response of single crystals of MgO subjected to the water drop impact conditions in Table 4.2 will be described.

##### 4.1.1 Specimen Preparation and Characterization

Single crystals of MgO were purchased from Norton Chemical Corp., Niagara Falls, Ontario, Canada, in the form of cleaved, undoped high purity single crystals. The crystals were water white in appearance and the manufacturer claims typical chemical analyses to be:

SiO <sub>2</sub>	30 PPM	CaO	30 PPM
Fe <sub>2</sub> O <sub>3</sub>	140 PPM	ZrO <sub>2</sub>	20 PPM
TiO <sub>2</sub>	12 PPM	MnO <sub>2</sub>	25 PPM
Al <sub>2</sub> O <sub>3</sub>	64 PPM	NiO	5 PPM

Specimens were prepared by cleaving, mechanically polishing, and chemically polishing. The specimens were first cleaved to size ( $\sim 15 \times 15 \times 5$  mm) on {100} planes. The sized pieces were then mechanically polished on one of the 15x15 mm faces to remove the cleavage steps and artifacts. The polishing procedure consisted of:

- (i) rough flat lap with 12  $\mu$ m SiC on a ceramic plate
- (ii) 5  $\mu$ m Al<sub>2</sub>O<sub>3</sub> on ceramic plate
- (iii) 0.3  $\mu$ m Al<sub>2</sub>O<sub>3</sub> on ceramic plate.

All three steps used water for the lapping medium.

Chemical polishing was done with a hot ( $\sim 100^\circ\text{C}$ ) 10N H<sub>3</sub>PO<sub>4</sub> aqueous solution. The action of this polish is described in Sangwal and Sutaria (1976). The polishing was continued until no evidence of mechanical polishing induced dislocations was apparent when the surface was etched. The prepared surfaces were then flat and oriented within 2 to 3 degrees of a {100} plane. Throughout this section the impact face will be labeled the (001) plane.

A dislocation etchant consisting of 0.5N aqueous H<sub>2</sub>SO<sub>4</sub> at 50°C was used for revealing ingrown dislocations, low angle tilt boundaries, and slip bands associated with impact. The etching times varied from 0.5 to 1.0 minute. The action of this etchant is also described more fully in Sangwal and Sutaria (1976). In addition to being a dislocation etchant, this solution preferentially dissolves material at fractures even if they are so tightly sealed as to be invisible to a light microscope before etching. This characteristic of the etchant was used to reveal the very fine fracture structure around the impact site.

Knoop microhardness measurements were made on the (001) surfaces prepared for impact. The hardness values were  $820 \pm 20 \text{ kg/mm}^2$  at 100 g load for measurements made with the major axis of the Knoop indentation in a  $\langle 110 \rangle$  direction on a {100} face. This value compares well with that reported by Brooks and Burnand (1973) listed in Table 4.1. An estimate of the initial or ingrown dislocation content of the crystals was made by counting etch pits on a {100} face. The density was determined to be approximately  $3 \times 10^5/\text{cm}^2$  not including the dislocations present in low angle tilt boundaries. Fig. 4.4 is a micrograph of a typical surface after dislocation etching.

After the specimen impacts a water drop and is recovered, it is carefully removed from the sabot and cleaned of recovery debris. The impact site is then identified by stress birefringence patterns visible in transmitted polarized light. Once identified the impact site may be viewed with reflected light at higher magnifications (100 to 400 X was used). There are very few features visible on the impacted surface, occasionally the larger fractures produced at velocities above  $600 \text{ ms}^{-1}$  may be seen.

A light dislocation etch was used to enhance the visibility of the damage for all impact conditions. Fig. 4.5 contains composite micrographs of the impacted face for shot no. 809 and 953. (Refer to Table 4.2.) The impact damage comprises a characteristic slip band pattern and a superimposed annular fracture pattern. The slip band pattern will be discussed first.

#### 4.1.2 Slip Band Structure in Water Drop Impacted Specimens

As seen in Fig. 4.5 there is a central region with a very low density of slip referred to as the central undamaged zone. The following descriptions will be made with reference to a right handed coordinate system with the z axis in the impact direction.



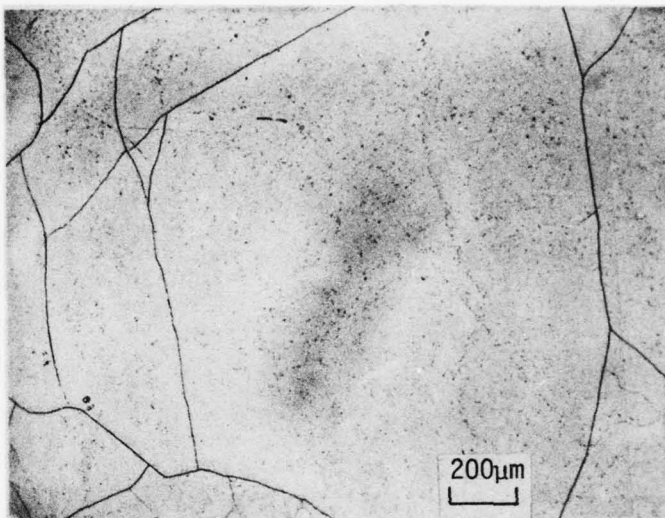
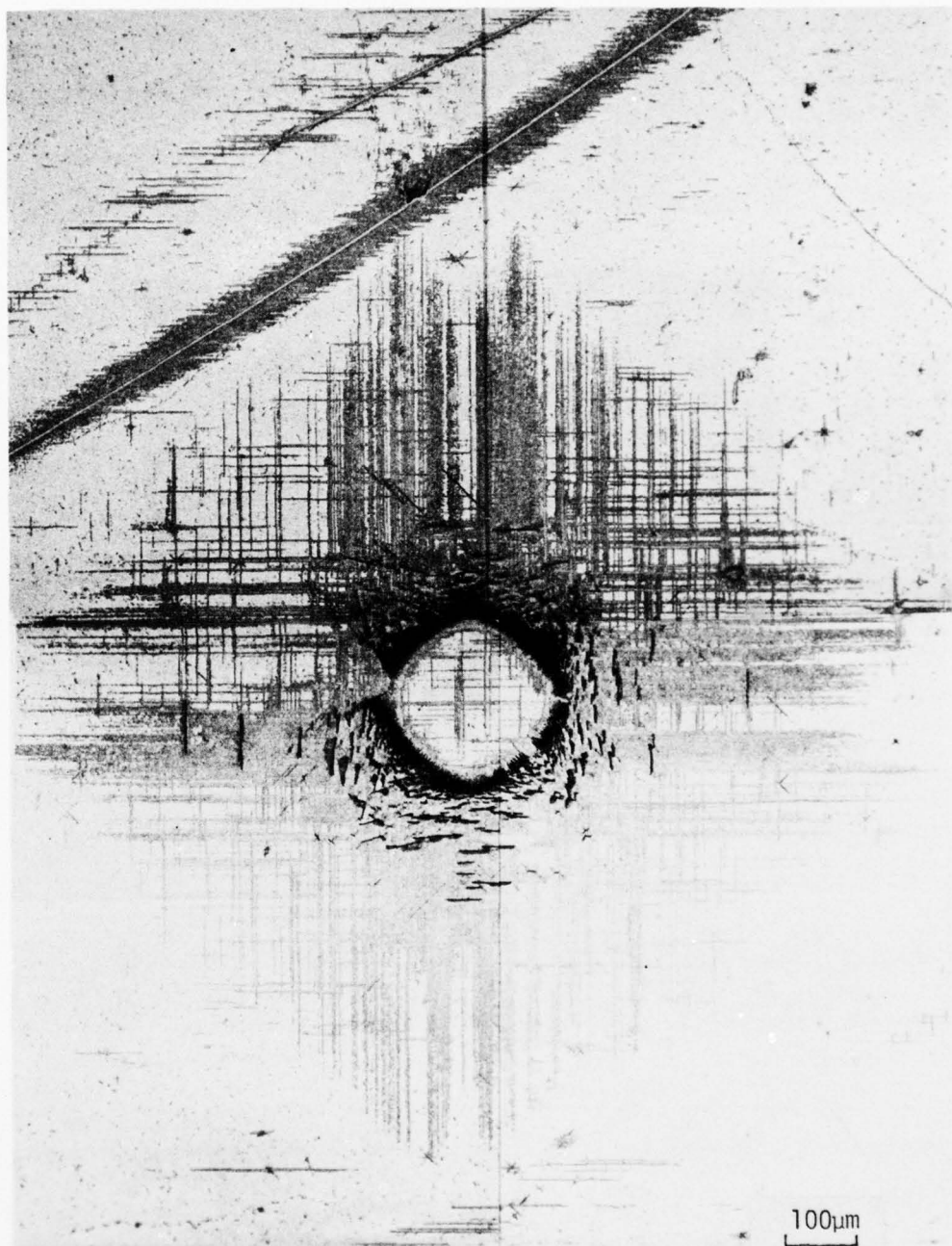
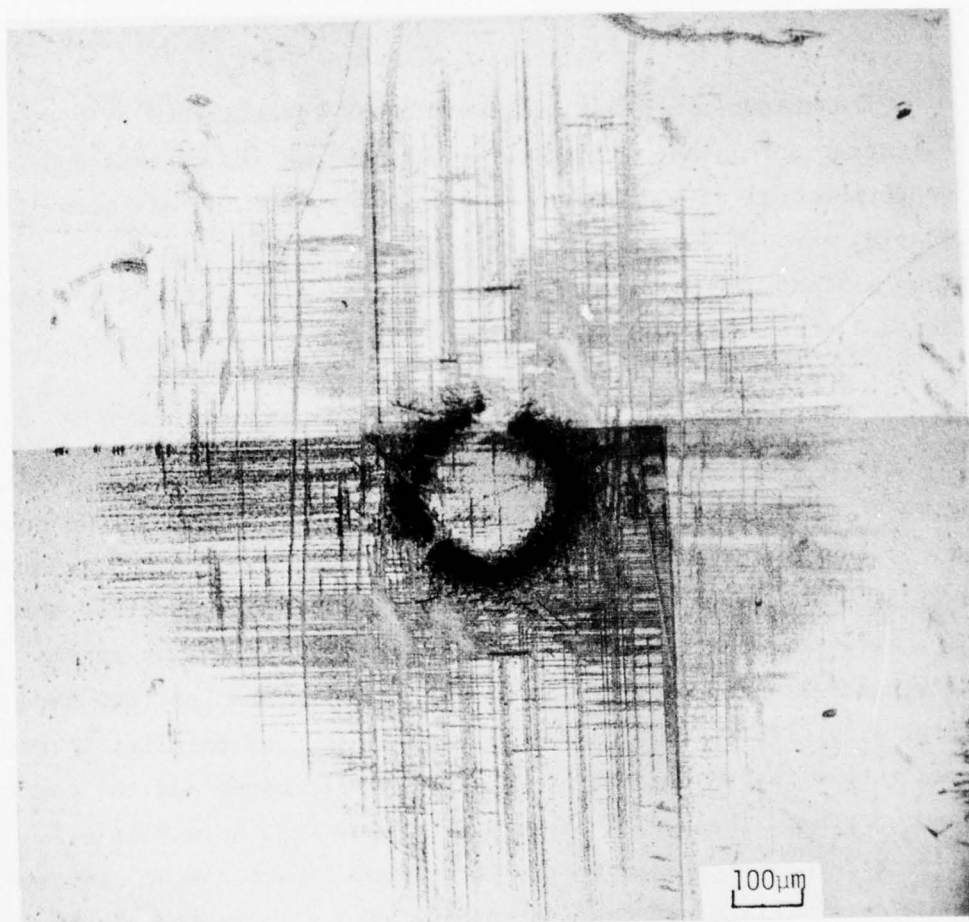


Figure 4.4. Dislocation Etched (001) Surface of MgO Specimen Prepared for Impact.



a. Shot No. 809 at  $556 \text{ ms}^{-1}$

Figure 4.5. Dislocation Etched Water Drop Impacts  
on (001) Face of MgO.



b. Shot No. 953 at  $563 \text{ ms}^{-1}$ .

Figure 4.5. (continued)

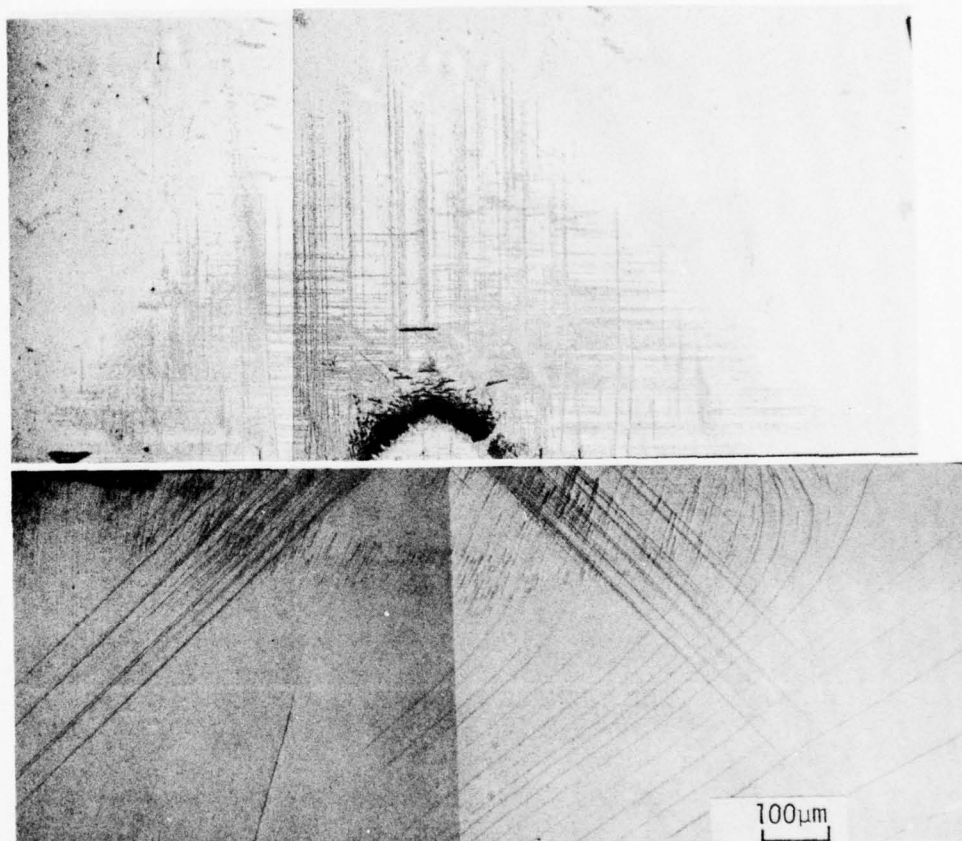
The slip band intersections with the (001) impact face are almost entirely in the [100] and [010] directions. There are a few exceptions associated with some of the larger impact fractures. These exceptions appear in the [110] and  $[\bar{1}\bar{1}0]$  directions. Due to their scarcity and short range, the slip bands associated with the fractures are suspected to be a result of the fractures rather than a cause.

The subsurface slip band pattern was investigated by sectioning the impact on a plane which passes through the impact axis and is therefore orthogonal to the impact face. This sectioning was accomplished by cleaving through the impact on the (010) plane. Again the surface was given a light dislocation etch and the slip band patterns revealed. Fig. 4.6 shows both the etched cross section and impact face of shot no. 807 and 953.

From the cross sections it is seen that there are essentially two types of slip bands present. One type apparent in both cross sections originates at the impact surface and proceeds at  $45^\circ$  into the crystal away from the center of the impact. These bands are labeled A in Fig. 4.7. In addition to the Type A slip bands there is another set of slip bands present only in the higher velocity shot no. 807 impact (Fig. 4.6). These slip bands are both at  $45^\circ$  and parallel to the impact face in the region bounded by the Type A slip bands and the central undamaged zone. These slip bands are labeled Type B in Fig. 4.7. The resultant deformations due to the water drop impact can be constructed from these observations and consideration of the slip systems in MgO. Since MgO has cubic symmetry there will be four planes of symmetry for water drops impacting in the [001] direction on the (001) face. Fig. 4.7 is a simplified sketch of the slip band structure constructed from the symmetry information and the slip band observations. MgO is known to slip on {110} planes in  $\langle 110 \rangle$  directions characteristic of ionic crystals with rock salt structure. Klein and Edington (1966) have discussed the reasons for the {110}  $\langle 110 \rangle$  slip systems being operative in MgO. From



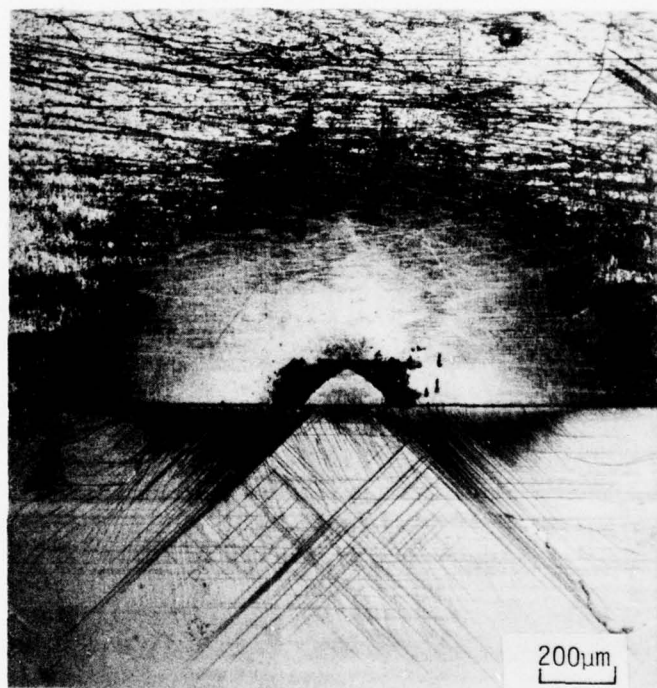
IMPACT FACE



CROSS SECTION

a. Shot No. 953 at  $563 \text{ ms}^{-1}$

Figure 4.6. Dislocation Etched Impact Face and Cross Section of MgO Specimens.



IMPACT FACE

CROSS SECTION

b. Shot No. 807 at  $672 \text{ ms}^{-1}$ .

Figure 4.6. (continued)

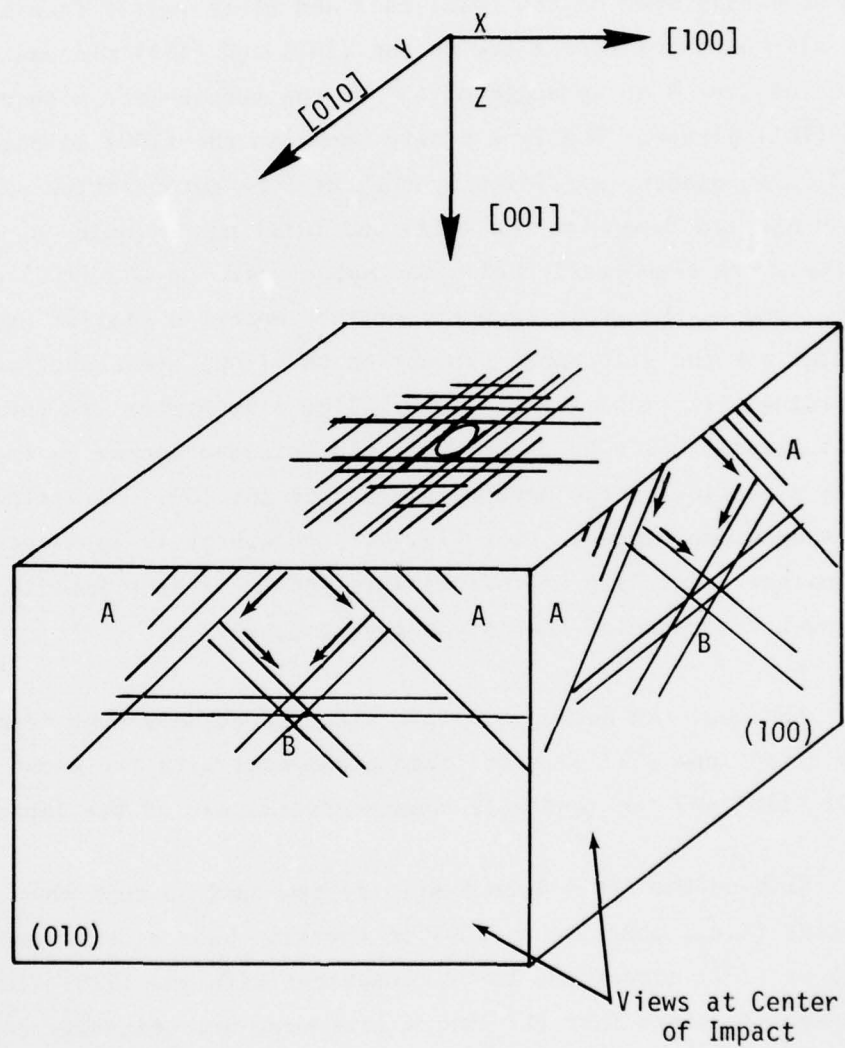


Figure 4.7. Sketch of Slip Bands Present and Coordinate System Used for Single Drop Impacts on MgO.

Fig. 4.5, 4.6, and 4.7 it is apparent that the slip due to drop impact takes place predominantly on the four  $\{110\}$  planes which make an angle of  $45^\circ$  to the (001) surface. These slip bands will be labeled  $\{110\}_{45^\circ}$ . Specifically these four planes are (101),  $(\bar{1}01)$ , (011), and  $(0\bar{1}1)$ . This can be easily seen on the (010) face and (001) impact face in Fig. 4.7. The slip bands of Type A are on the (101) and  $(\bar{1}01)$  planes. The slip bands of Type B at an angle of  $45^\circ$  to the surface are also on the (101) and  $(\bar{1}01)$  planes. The Type B slip bands in the (100) direction are also  $\{110\}$  slip planes, specifically they are the intersection of the (010) cross section face with the (011) and  $(0\bar{1}1)$  planes which appear at  $45^\circ$  to the surface generally below the impact site on the (100) cross section face. Due to the cubic symmetry of the impact, a similar explanation applies for the slip bands present on the (100) cross section. The two remaining slip planes of the  $\{110\}$   $\langle 110 \rangle$  slip system are the (110) and  $(\bar{1}\bar{1}0)$  planes. Slip bands on these planes would appear in the [110] and  $[\bar{1}\bar{1}0]$  direction on the impact face and in the [001] direction on the cross sectioned faces. From Fig. 4.5 and 4.6 it is apparent that there is insignificant slip on these planes for water drop impacts on (001) MgO over the range of conditions investigated.

Now that the dominant active slip planes have been identified, the slip directions will be identified consistent with the known slip systems  $\{110\}$   $\langle 110 \rangle$  and the generally compressive nature of the impact stresses.

Slip on the (101) Type A slip system must be such that the material interior (i.e., positive x side) to the slip band either moves in the  $(\bar{1}01)$  or  $(10\bar{1})$  directions to be consistent with the  $\{110\}$   $\langle 100 \rangle$  slip systems. The fact that the impact pressures are primarily compressive at the center of the impact makes  $(\bar{1}01)$  the obvious choice. A somewhat similar argument applies to the Type B slip bands present in the higher velocity impacts. For these bands the slip is such that the material on the positive side of the band moves in a (101) direction. Both of these deformations are indicated in Fig. 4.7 by small arrows. By symmetry the mirror image bands slip as indicated in Fig. 4.7.

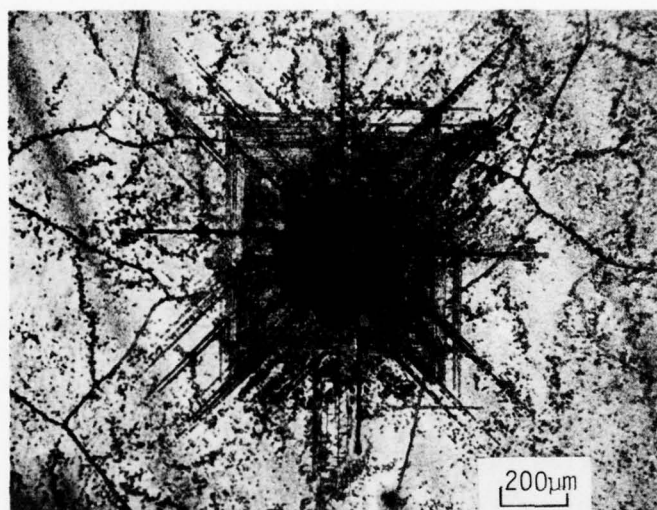


The Type B slip bands which appear in the  $[100]$  direction on the  $(010)$  cross section are as previously indicated: the same Type B slip bands which appear at  $45^\circ$  to the surface on the  $(100)$  cross section. By symmetry the slip bands on the  $(010)$  cross section have the same slip as those on the  $(100)$  cross section. Therefore the slip on the bands appearing in the  $[100]$  direction on the  $(010)$  cross section is either in the  $[011]$  or  $[0\bar{1}1]$  direction. The cumulative effect of slip in the indicated directions on these six slip planes is that the region of the crystal generally below the impact bounded by the six slip planes (A and B) and the impact face is moved in the  $[001]$  direction without being deformed by slip itself.

For impact velocities on the order of  $560 \text{ ms}^{-1}$  and less (see Fig. 4.6a), there are very few Type B slip bands present. Although no Type B slip bands intersected the cross section in Fig. 4.6b, some were identified by transmitted polarized light. At the lower velocities the displacement of the material below the impact and resultant stresses are not sufficient to activate a large number of Type B slip bands.

The deformation response of  $(001)$  faces of MgO single crystals described above for water drop impacts is significantly different than that of quasistatic spherical indentations or solid particle impacts on  $(001)$  MgO. There has been a significant amount of research done on the mechanisms of solid particle impacts on MgO, (Keh, 1960, Jolliffe, 1966, Narayan, 1973, Narayan and Washburn, 1973, and Hooker and Adler, 1978).

For both solid particle impacts and spherical indentations, all authors report seeing slip on all six  $\{110\} \langle 110 \rangle$  slip systems. The presence of all systems produces a characteristic "rosette" pattern (see Fig. 4.8 for an example). In addition to the four  $\{110\}_{45^\circ}$  slip systems identified in the water drop impacts, two  $\{110\} \langle 110 \rangle$  slip planes which intersect the  $(001)$  surface at  $90^\circ$  ( $\{110\}_{90^\circ}$ ) are also active. The slip on the  $\{110\}_{90^\circ}$  planes is in the  $[110]$  directions in the impact plane.



→  
[100]

Figure 4.8. Characteristic Rosette Pattern for Sapphire  
Bead Impact on (001) MgO (Hooker and Adler, 1978).

This slip plane network indicates not only displacement of the material under the impact site in the  $[001]$  direction as in the water impacts but also displacement of material parallel to the impact plane.

The previous description of the slip deformations observed for water drop impacts has not considered the temporal development of slip or possible strain rate effects. Although it is not possible to observe the step by step development of slip during an impact, there are several clues in the slip pattern left by the impact which when combined with an understanding of the temporal nature of the loading function do provide some understanding of the evolution of the resulting deformation.

For impacts generating Type B slip bands there is an apparent blockage of the two orthogonal sets of Type B slip bands by both interaction with each other and the Type A slip bands. This blockage indicates that, although slip did not occur at the same time, it did occur later than the slip on the interior Type A bands. In addition to the evidence of slip blockage, the fact that the lower velocity impact in Fig. 4.6 has only begun to produce Type B slip bands indicates that slip on the Type B slip bands occurs later than slip on Type A bands and most likely is a result of the Type A slip deformations.

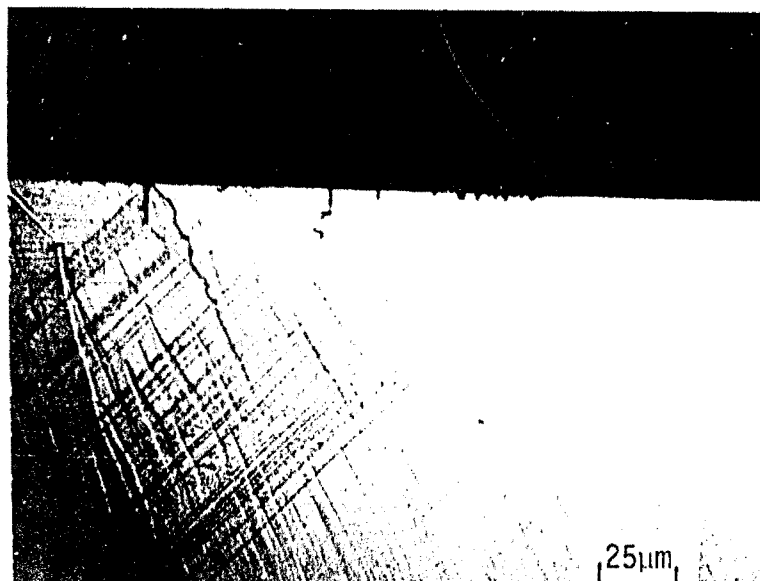
A reasonable explanation of this sequence of events is that the Type B slip bands were activated by  $[100]$  and  $[010]$  tensile stresses in the region of the crystal immediately below the impact site which was being driven in the  $[001]$  direction.  $[100]$  tensile stresses in the  $(010)$  plane would result from the  $[\bar{1}00]$  and  $[100]$  components of  $[\bar{1}01]$  and  $[101]$  slip, respectively, on the Type A  $\{110\}_{45^\circ}$  slip systems originating at the impact surface. Similar stresses would arise in the  $[010]$  direction in the  $(100)$  plane.

As can be seen in Fig. 4.6, the most extensive slip bands (both on the impact face and the cross section) are the ones which originate at the periphery of the central undamaged zone. These slip bands are the deepest because they were nucleated first and subsequently propagated for the longest time. The slip bands occurring further out are smaller due to a combination of later nucleation and an attenuating stress field. The slip bands eventually disappear due to insufficient stress to nucleate them.

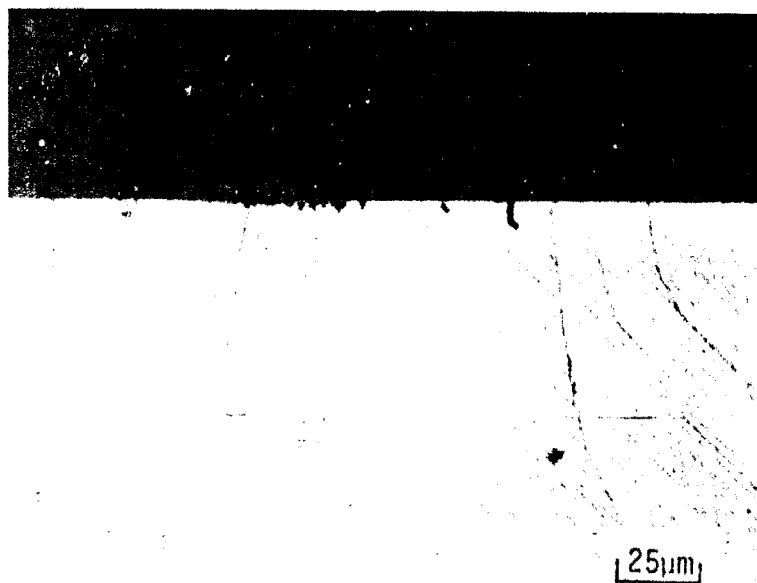
The stresses required for nucleation (activation) and expansion (motivation) of slip bands in MgO has been extensively studied by Stokes, et al. (1959b), and in LiF by Gilman and Johnston (1957) and Johnston and Gilman (1960). Stokes, et al., found the activation stress to be approximately twice the motivation stress in chemically polished single crystal MgO. The higher stress required for activation of dislocations than for motivation and the fact that dislocations move at a velocity which is a function of the applied stress (Johnston and Gilman, 1959) partially accounts for the slip band development during impact. As can be seen in Fig. 4.5, 4.6, 4.9, and 4.10, the Type A slip bands are numerous, narrow and independent.

This slip band pattern is very different from quasistatic deformations. Quasistatic slip band behavior has been studied in MgO by Argon and Orowan (1964) and Stokes, et al. (1959b), and in LiF by Johnston and Gilman (1960). For single crystals the slip bands (comprised of dislocation half loops) in quasistatic deformations through various mechanisms described in these references widen and expand resulting in plastic shear of the crystal. The end result is a few very wide and extensive slip bands. Only a few slip bands develop due to the shortage of active sources in chemically polished specimens and the larger stress required to activate rather than to motivate slip bands.



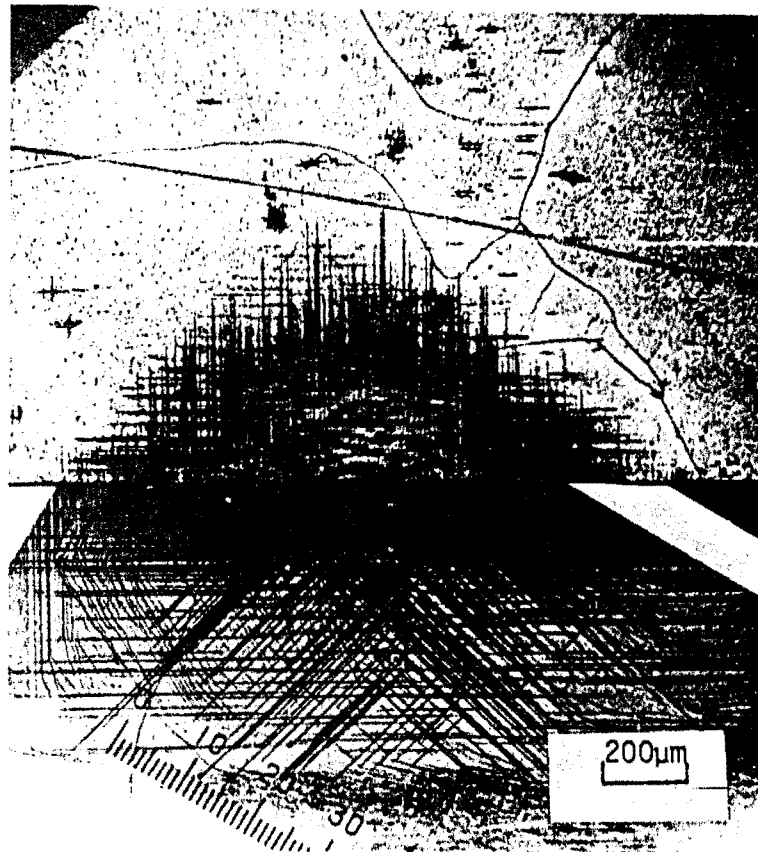


a. Shot No. 953 at  $563 \text{ ms}^{-1}$



b. Shot No. 807 Impacted at  $672 \text{ ms}^{-1}$

Figure 4.9. Etched Cross Section Showing Slip Bands and Fractures In MgO.



IMPACT FACE

CROSS SECTION

Figure 4.10. Dislocation Etched Impact Face and Non-centerline Cross Section of Shot No. 808. Note Interaction of Fracture Pattern with Low-Angle Tilt Boundary.

In the water drop impact situation, there are many narrow slip bands also comprised of dislocation half loops which indicate that the stresses are large enough for slip band activation but the temporal development of strain is more rapid than can be accommodated by slip band motivation. A quantitative feeling for the order of magnitude of the strain rates occurring in a  $550 \text{ ms}^{-1}$  water drop impact can be gained by realizing that the total time that the peak impact pressures are acting on the surface is estimated to be on the order of 50 nanoseconds.

The necessity of constant activation of new slip bands at high strain rates would result in a higher flow stress than that of a quasi-static deformation (i.e., a strain rate effect). Jolliffe (1966) measured a dynamic yield stress in LiF 30% higher than the static yield stress. Measurements were made by determining the extent of slip bands and comparing with calculated Hertzian stresses for spherical impacts and indentations. His results tend to corroborate the suspected strain rate effect for water drop impacts on MgO. Klein (1965) has reported a similar trade-off between activation and motivation of slip in explosively shocked MgO single crystals. He reports numerous narrow slip bands for crystals subjected to short and intense loading, and fewer but wider slip bands for crystals exposed to longer but lower intensity loads. He also reports intermediate results.

On the basis of the previous analysis, a specimen of (001) MgO was prepared with numerous surface dislocation sources such that slip could be motivated at a lower stress than that required to activate slip. The objective of this experiment was to see if impact resistance could be improved. The specimen was prepared by mechanical polishing with  $\text{Al}_2\text{O}_3$  submicron size polishing compound on nylon. The surface contained such a high density of dislocations that etching could not distinguish individual dislocations or slip bands. In addition to dislocations the surface contained numerous scratches.

After water drop collisions at  $512 \text{ ms}^{-1}$  and  $574 \text{ ms}^{-1}$  the impacts were located by transmitted polarized light (etching revealed nothing) and sectioned. The etched cross section and impact face are shown in Fig. 4.11. The impact shows numerous slip bands but no detectable fractures. Fig. 4.12 is included for comparison and is a chemically polished specimen (containing few dislocation sources) impacted at  $413 \text{ ms}^{-1}$ . Note the distinct fracture annulus and few but independent slip bands.

These results indicate that introducing dislocation sources in the impact surface does help to improve the impact fracture resistance. It is possible that the surface was in a partially compressive state due to the polishing which may have also helped to eliminate the fractures. One surprising result is that the polishing scratches did not act as flaws to promote fracture as they do for  $\text{CaF}_2$  (see Section 4.2). Stokes, et al., (1959a) have developed a method for introducing dislocation sources in the surface without leaving scratches or a compressive layer. This method could be used to check the above result.

Although Klein and Edington (1966) have identified slip at high strain rates on  $\{100\}$ ,  $\{111\}$ , and  $\{112\}$  planes in the  $\langle 110 \rangle$  directions in addition to slip on  $\{110\}$  planes in  $\langle 110 \rangle$  directions, the only slip systems identified for the MgO water drop impact conditions in Table 4.2 are the  $\{110\} \langle 110 \rangle$  systems. Even though we observe slip only on  $\{110\} \langle 110 \rangle$  systems for impact on a  $\{100\}$  plane, it is possible other slip systems may be active for other impact conditions. Slip on other systems may occur for impacts on planes other than (001). Impact orientations such that the stresses on the  $\{110\} \langle 110 \rangle$  systems are less preferential may also cause slip on other systems. Hulse, et al. (1963), have used a similar approach to activate slip on  $\{100\} \langle 110 \rangle$  systems at elevated temperatures for MgO crystals in compression.

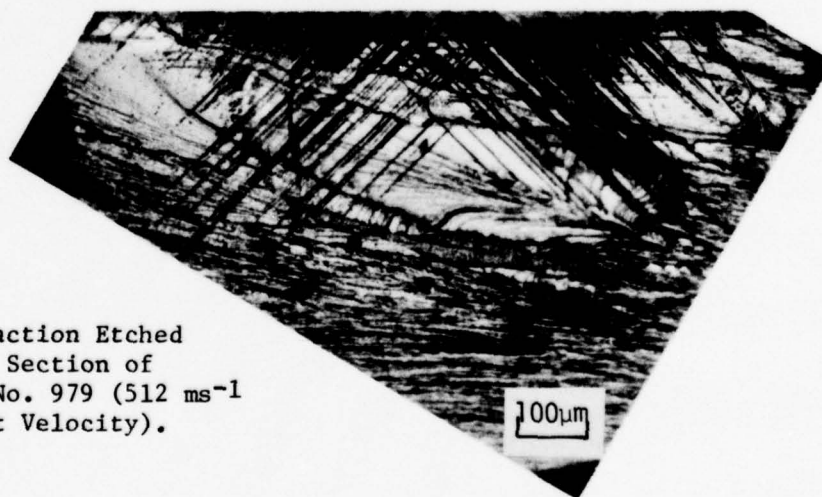




a) Impact Site of Shot No. 1010  
Viewed in Transmitted Polarized  
Light. Impact Velocity  $574 \text{ ms}^{-1}$ .

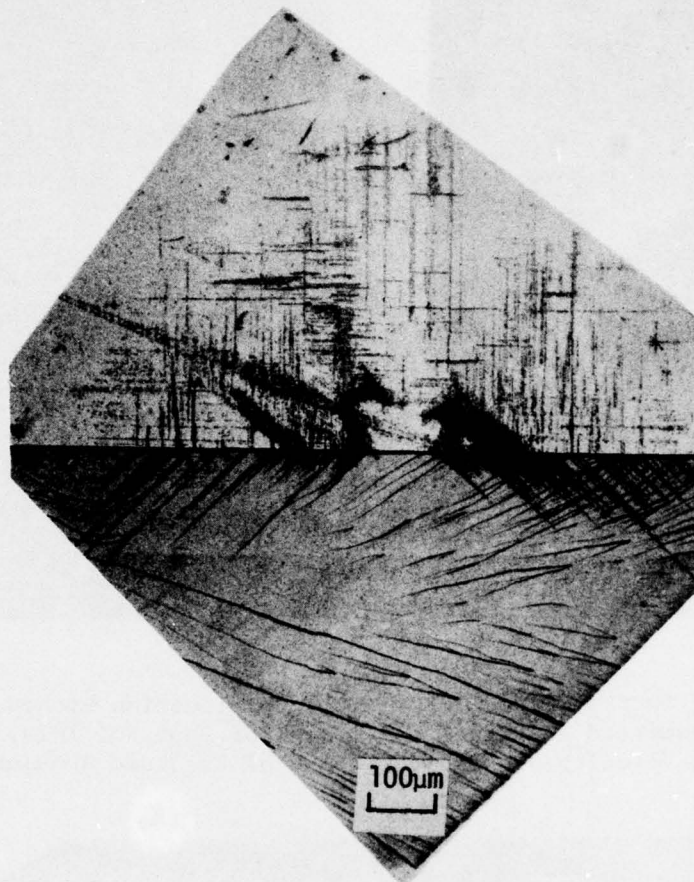


b) Dislocation Etched Impact Site  
for Shot No. 1010. Note Absence  
of Fracture Annulus.



c) Dislocation Etched  
Cross Section of  
Shot No. 979 ( $512 \text{ ms}^{-1}$   
Impact Velocity).

Figure 4.11. Nature of Water Drop Impact Damage  
on Mechanically-Polished  $\text{MgO}$ .



Impact Face

Cross  
Section

Figure 4.12. Dislocation Etched Impact Face and Cross Section of Shot No. 858 ( $413 \text{ ms}^{-1}$ ). Distorted Incomplete Fracture Annulus and Slip Band Pattern is Due to Bubbles in the Drop.

Narayan (1973) and Narayan and Washburn (1973) have reported that low velocity  $\text{Al}_2\text{O}_3$  microsphere impacts on (100) MgO produce slip in the  $\{110\} \langle 110 \rangle$  slip systems and that in addition the dislocations consist of dislocation dipoles (two closely spaced dislocations of opposite sign). In contrast, low strain rate indentations made by a sharp pin show single dislocations. Whether or not the dislocations present in a water drop impact damage site are single or dipole pairs and what consequence that would have on slip band development will have to be investigated further.

#### 4.1.3 Fracture Initiation Mechanisms

In addition to the characteristic slip band pattern for a single drop impact on (001) MgO, there is a characteristic fracture annulus for impact velocities in the range from 276 to 679  $\text{ms}^{-1}$ . When etched and viewed on the impact face, the fractures display the following features (refer to Fig. 4.5 and 4.13).

- (i) Due to the four-fold symmetry around the [001] impact axis, the impact damage is similar in eight octants.
- (ii) The fractures exist in an annulus whose inner boundary is approximately square. The diagonals of this square are the [100] and [010] directions.
- (iii) The fractures found at the inner radii tend to be of very short range and high density.
- (iv) In the  $\langle 100 \rangle$  radial directions the larger fractures tend to intersect the surface tangent to the impact annulus.
- (v) The fractures lying near a  $\langle 110 \rangle$  radial direction are of two types: (1) those whose intersection with the (001) impact face is tangent to the impact; (2) those that are apparent distortions in a radial direction of the fractures in (ii). Intersections of these radially distorted fractures from two quadrants form the W-shaped fractures seen in Fig. 4.13.



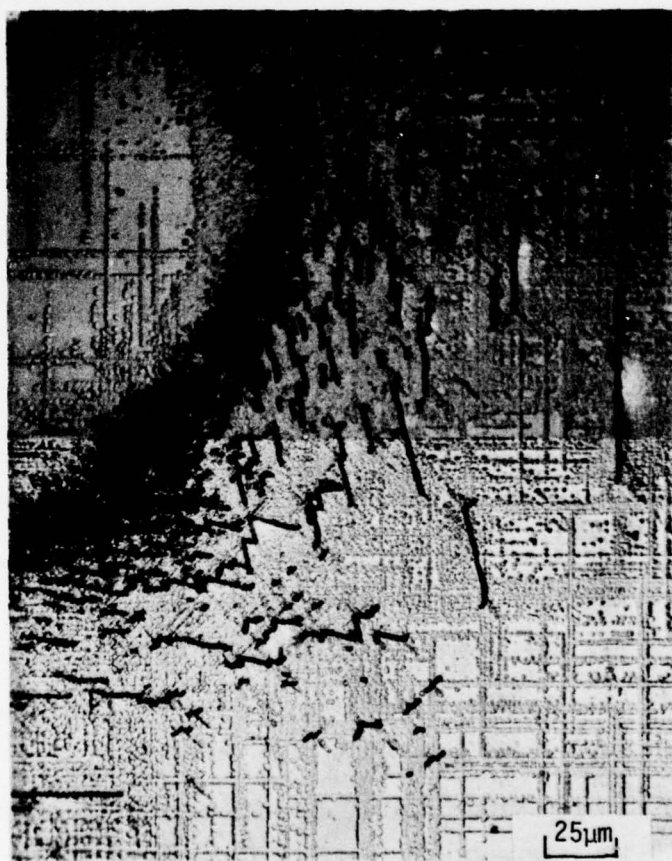


Figure 4.13. Inner Region of One Quadrant of Figure 4.5.



- (vi) The density of fracture falls off rapidly outside the fine fractures (iv). The fractures present farthest from the center are of type (iv) and are generally in the  $\langle 100 \rangle$  radial sectors.

In cross section the fractures of type (iii) are found to be very shallow ( $< 3 \mu\text{m}$ ) and the larger fractures of type (iv) to be  $10 \mu\text{m}$  or less in depth. The type (iv) fractures typically consist of two straight sections as seen in Fig. 4.9.

The fracture annulus appears to be the cumulative effect of dislocation and dislocation slip band interaction phenomena which are active in the water drop impact situation. Fracture initiation mechanisms have been suggested by Stokes, et al. (1958, 1959b, 1960), Cottrell (1958), Keh, et al. (1959), Argon and Orowan (1964), Clarke, et al. (1962), Washburn, et al. (1959), and Briggs, et al. (1964). All of these mechanisms require intersecting slip bands for operation. In Fig. 4.9a both orthogonal and nonorthogonal intersecting  $\{110\}_{45^\circ}$  slip bands are seen. Although intersecting slip bands were not observed after etching shot no. 807 (Fig. 4.9b), they could be seen when viewed with transmitted polarized light. A possible sequence of events for slip band development is described which is consistent with previous observations and includes dislocation slip band interactions in the region of the fracture annulus.

Consider a 2 mm water drop impacting (001) MgO at  $500 \text{ ms}^{-1}$ . The calculated longitudinal and shear wave velocities along the  $\langle 100 \rangle$  directions in MgO are 8.96 and  $6.56 \text{ mm}/\mu\text{s}$  (Adler and Hooker, 1977). The rate of expansion of the contact zone between the drop and the face of the MgO target will be approximated by a compressible drop impact on a rigid plane. Initially the periphery of the contact zone moves faster than the wave speeds in MgO or water, however it only takes 5.8 ns for the shear wave in MgO to separate from the contact boundary. This occurs at a radial distance of  $76 \mu\text{m}$  from the point of impact. The drop continues

to load the surface for at least an additional 40 ns and the boundary of the contact zone reaches a radial distance in excess of 200  $\mu\text{m}$ . At this point pressure release occurs and the applied pressure precipitously declines. During this time the contact zone is being deformed in the [001] direction.

The impact region in MgO will experience both the effects of the stress waves propagating in the material and the direct deformation of the contact zone. A possible mechanism for activation of intersecting active slip bands in the vicinity of the impact face is formulated on the basic water drop loading sequence. When the shear wave separates from the contact zone it is capable of activating Type A slip bands (Fig. 4.7). The initiation of the Type A slip bands at the boundary of the central undamaged zone can be clearly seen in Fig. 4.6. Next, due to the direct deformation in the [001] direction of the material in the contact zone, the surface exterior to the contact zone is in a tensile state. While these tensile stresses exist in the vicinity of the impact face, the orthogonal  $\{110\}_{45^\circ}$  slip bands seen in Fig. 4.9 are activated, intersect with the active Type A bands already present, and cause the observed fractures. As the contact zone expands and engulfs the fractures the attendant compressive state halts further fracture development at that location. The short period of time that the tensile stresses exist would account for the extremely shallow (3  $\mu\text{m}$ ) fractures at the inner radii and somewhat deeper fractures ( $\sim 10 \mu\text{m}$ ) at the outer range of the fracture annulus. As described above the  $(\bar{1}01)$  slip bands activated in tension only have time to propagate to shallow depths and interact with other bands.

The fracture initiation mechanism proposed by Stokes, et al., (1958, 1959b, 1960) occurs at intersections where two expanding slip bands have completely cut through one another. This situation exists at the surface during the short time it is in a tensile state. A fracture is nucleated by a pile-up of edge dislocations in the slip bands

activated in tension against the barrier provided by the orthogonal slip bands (see Fig. 4.14). Once a crack is nucleated it tends to propagate along the  $\{110\}$  plane at the edge of the barrier slip band. At some point the fracture is large enough to initiate cleavage on the  $\{100\}$  plane normal to the tension. This mechanism generates a characteristic  $(\bar{1}01)$   $[010]$  slit source. This characteristic shape can be seen in cross section in Fig. 4.9.

Stokes, et al., (1960) have noticed that by introducing many active slip systems the above fracture initiation mechanism can be suppressed for quasistatic deformations. Their conclusion is that one or both of the following mechanisms is responsible: (1) if the spacing between slip bands is very small, the slits, although they may form, will not be able to grow to a critical size to cause catastrophic fracture on a  $\{100\}$  plane, and (2) the numerous slip sources allow deformation to proceed homogeneously in the crystal and eliminates large local strains. If either or both of these mechanisms are active, introducing numerous active slip systems in the surface layer to be impacted should suppress fracture formation in single crystal MgO.

Fracture suppression by introducing numerous slip sources was observed (as mentioned previously) and attributed to rate effects of slip band activation and motivation. The suppression mechanisms proposed by Stokes for quasistatic deformations most likely also contribute to dynamic fracture suppression.

A mechanism for fracture nucleation as a result of interacting non-orthogonal  $\{011\}$   $\langle 110 \rangle$  slip systems has been proposed by Keh, et al., (1959). Close examination of Fig. 4.5 reveals numerous fractures which were apparently nucleated at the intersection of two non-orthogonal  $\{110\}_{45^\circ}$  slip systems. During the time the surface layer is in tension, the two intersecting Type A slip systems with dislocation motions are the proper geometry to interact as in Keh's model. A schematic of Keh's



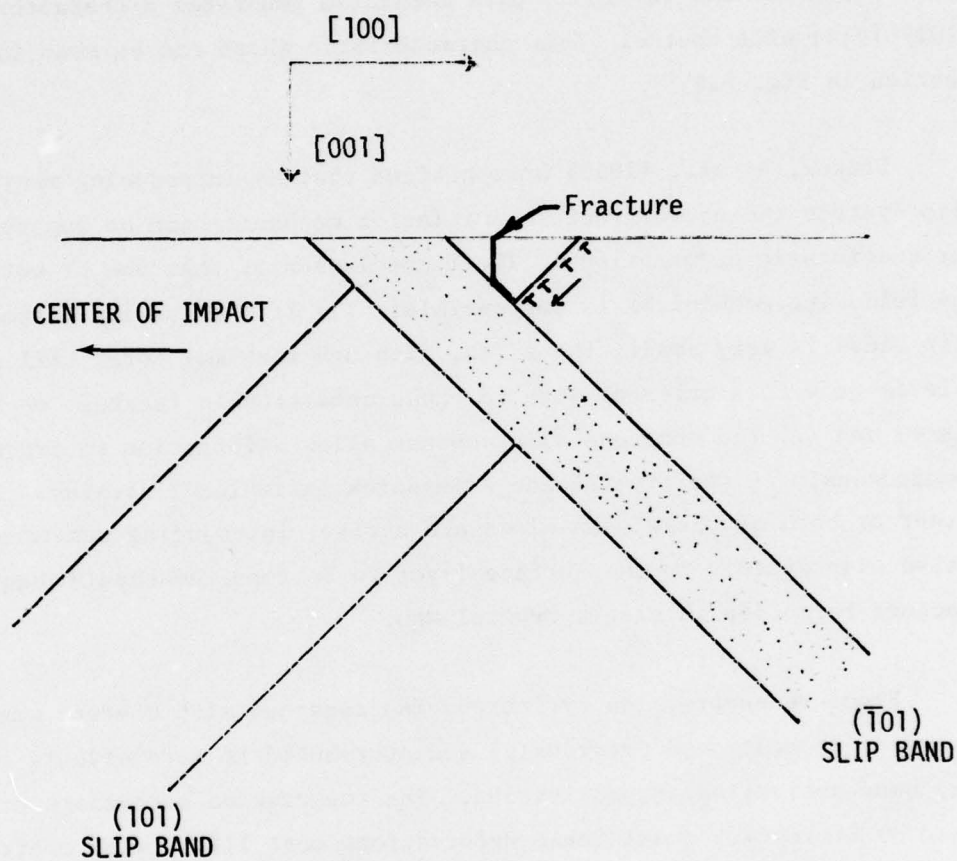


Figure 4.14. Slip Band Interaction for Fracture Initiation  
Proposed by Stokes, et al. (1958, 1959, 1960).



model is shown in Fig. 4.15. The fractures predicted by this model would lie in a radial direction relative to the impact. Close examination of Fig. 4.5 reveals there are short  $\langle 110 \rangle$  radial fracture segments (on the order of the width of the intersecting slip bands) in the fractures present at the intersections of the non-orthogonal  $\{011\}_{45^\circ}$  slip bands. The extension of these radial fractures in a tangential direction is consistent with the radial tensile forces, i.e., a flaw was initiated in the  $\langle 110 \rangle$  radial direction by the Keh mechanism and then propagated in the tangential direction by the radial surface tensile stresses.

Cottrell (1958) has proposed that a fracture on the (001) plane may be initiated by the intersection of edge dislocations moving on (101) and  $(10\bar{1})$  planes in metals. The Cottrell mechanism could account for the (001) fracture to the surface but would not be able to account for the (101)  $[010]$  slits observed in Fig. 4.9. The fracture extension mechanism proposed by Clarke, et al., (1962) in which a microcrack grows to critical size by generating dislocations at its front is also not likely to be active in this case due to the change in direction in the fracture from parallel, or inclined at  $45^\circ$ , to the surface to perpendicular to the surface.

Argon and Orowan (1964) have a different view of the fracture initiation process for slip band interactions in MgO than that of Stokes, et al., (1958, 1959b, 1960), Keh, et al., (1959), Clarke, et al., (1962), Cottrell (1958), and Washburn, et al., (1959). Argon and Orowan maintain that fractures are caused at slip band intersections due to high macroscopic stresses resulting from the geometrical incompatibilities of plastic deformation across the intersecting slip bands rather than the coalescence of individual dislocations. It is conceivable that due to the high strain rates associated with water drop collisions, even though the slip bands are very narrow, stresses large enough to cause fracture could be attained due to the inability of additional plastic deformation to relieve the stresses fast enough. This mechanism may operate during

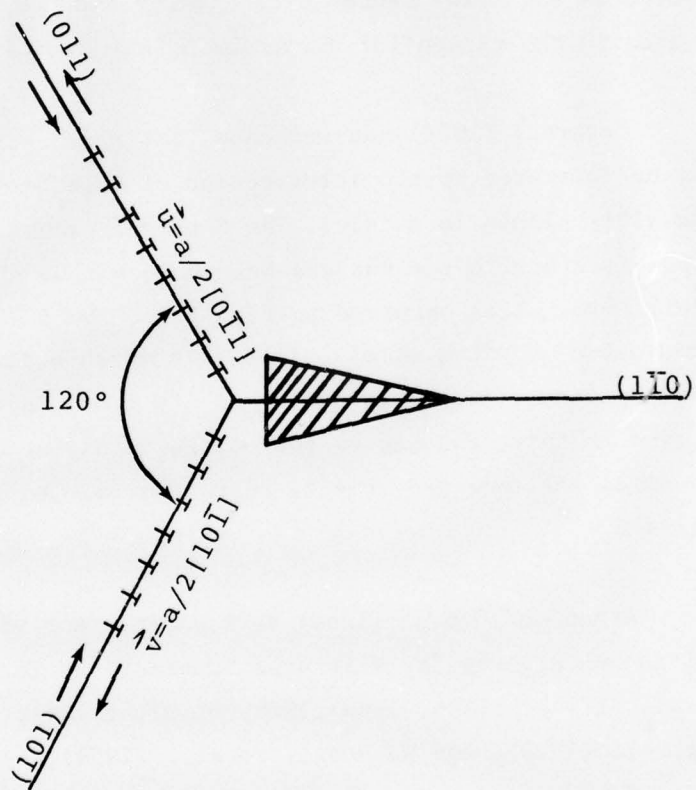


Figure 4.15. Crack Formation on (110) Plane in MgO Crystals (due to Keh, et al., 1959).

the surface tensile state at the intersection of both the orthogonal and non-orthogonal  $\{011\}_{45^\circ}$  slip planes. Presumably the stresses due to slip band intersection would initiate a fracture at the intersection, then the surface layer tensile stresses would cause the fracture to propagate to the surface. This two stage fracture mechanism would explain the observed sharp turn in the fractures (see Fig. 4.9). In Fig. 4.10 it is apparent that there has been an interaction between the low-angle tilt boundary which passes through the slip band pattern visible on the impact face and the slip bands to either cause or enhance the fractures present. Slip across a low-angle boundary was suggested as a mechanism of crack formation by Orowan (1954) and observed by Gilman (1954). For both LiF and MgO Washburn, et al. (1959), have observed dislocation pileups against subgrain boundaries (i.e., low-angle boundaries) are the exception rather than the rule. They have postulated that sub-boundaries are effective barriers only when certain geometric relations exist between the dislocation Burgers' vector and the boundary. Washburn's work was done at low strain rates.

To obtain some understanding of water drop impacts on MgO at  $1000 \text{ ms}^{-1}$ , impacts have been made with nylon beads as a water drop simulation (Adler and Hooker, 1977). The lack of surface fractures but severe subsurface fractures is particularly striking. It would be of interest to see if a water drop collision would produce the type of damage observed for the nylon bead impact at the higher impact velocity. A comparison could be carried out at close to  $800 \text{ ms}^{-1}$  using water and an equivalent size nylon bead.

A nylon bead impact at  $1000 \text{ ms}^{-1}$  on MgO has been described by Hooker and Adler (1978) in some detail. Fig. 4.16 is an etched cross section of the impact. The large wing-like structures are fractures caused by the impact. Close observation of these reveals two distinct origins of fracture (one for each wing). The origins are at the position which in a water drop impact is at the intersection of the Type A



Figure 4.16. Cross Section of Nylon Bead Impact  
at  $1000 \text{ ms}^{-1}$  on (001) MgO.



and Type B slip bands. It is quite likely that a flaw was initiated by the mechanism of Argon and Orowan (1964) or a dislocation coalescence mechanism. After initiation the flaw was propagated to leave the wing-like fracture.

The fact that there is not a fracture annulus on the surface similar to those observed for water drop impacts is somewhat surprising and probably has something to do with the different temporal development and magnitude of impact stresses for nylon versus water. The fracture response of ZnS to water drop and nylon bead impacts is described in Section 5. Comparison of high velocity water drop and nylon bead impacts on MgO at  $800 \text{ ms}^{-1}$  may help to clarify this apparent anomaly, as well as to explore the nature of the damage produced by nylon beads at lower impact velocities.

#### 4.2 CALCIUM FLUORIDE

Calcium Fluoride has a fluorspar structure with mechanical properties which are significantly different from those of MgO or LiF which have a rock salt structure.  $\text{CaF}_2$  cleaves on  $\{111\}$  planes characteristic of crystals with a fluorspar structure and exhibits slip on  $\{100\}$  planes in  $\langle 110 \rangle$  directions (Phillips, 1961). In contrast to MgO,  $\text{CaF}_2$  shows very little ductility at room temperature (Burn and Murray, 1962).

##### 4.2.1 Specimen Preparation and Characterization

Polished specimens of single crystal  $\text{CaF}_2$  were purchased from Harshaw Chemical Co., Solon, Ohio. The specimens were supplied as right cylinders 17 mm in diameter and 8 mm thick with polished faces in the  $\{111\}$  and  $\{100\}$  orientations. Unfortunately the as-received polished faces contained numerous scratches and polishing artifacts which interacted strongly with the water drop impact damage. (We are not aware of any successful chemical polishing procedure for  $\text{CaF}_2$ .) The specimens

were subsequently sent to AMF Optics, Woburn, MA, for polishing with a proprietary mechanical polish. The AMF polish was significantly better than that from Harshaw.

A dislocation etchant consisting of 25 ml HCl, 5 ml HNO<sub>3</sub>, and 30 ml H<sub>2</sub>O (Becher, 1976) was used to reveal fractures and dislocations on both {111} and {100} faces. To reveal dislocations on {100} faces, the surface must be meticulously polished to a high degree of perfection. An estimate of the ingrown dislocation content of the bulk material was obtained by counting etch pits on a {111} cleaved face. The density was determined to be on the order of  $5 \times 10^4 \text{ cm}^{-2}$  not including those present in the low-angle tilt boundaries. Figure 4.17 is a micrograph of a cleaved and etched {111} surface.

The {111} and {100} oriented specimens were impacted over the velocity range of 300 to 550 ms<sup>-1</sup>. Table 4.2 summarizes the shot numbers and impact conditions.

#### 4.2.2 Dislocation Etch Pit Patterns on CaF<sub>2</sub>

Water drop impacts on {100} and {111} faces produced different but characteristic dislocation etch pit and fracture patterns. The dislocations present in {111} impact sites will be discussed first.

Dislocation etched impact sites for impact velocities of 307 ms<sup>-1</sup>, 404 ms<sup>-1</sup>, and 521 ms<sup>-1</sup> are shown in Fig. 4.18. It is immediately apparent that in comparison to (100) MgO that (111) CaF<sub>2</sub> exhibits much less dislocation slip band activity and that impacts at 307 ms<sup>-1</sup> have considerably fewer dislocation etch pits than impacts at 521 ms<sup>-1</sup>. In addition to having less dislocation activity the dislocations present are either loosely organized into slip bands or isolated.

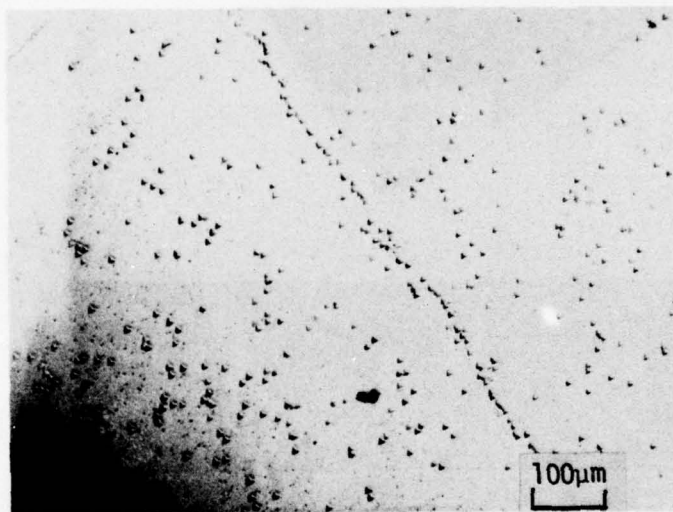
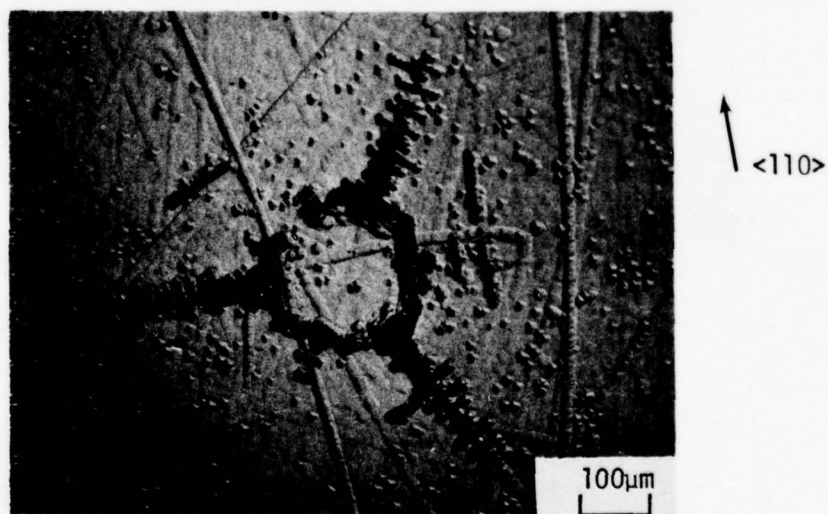
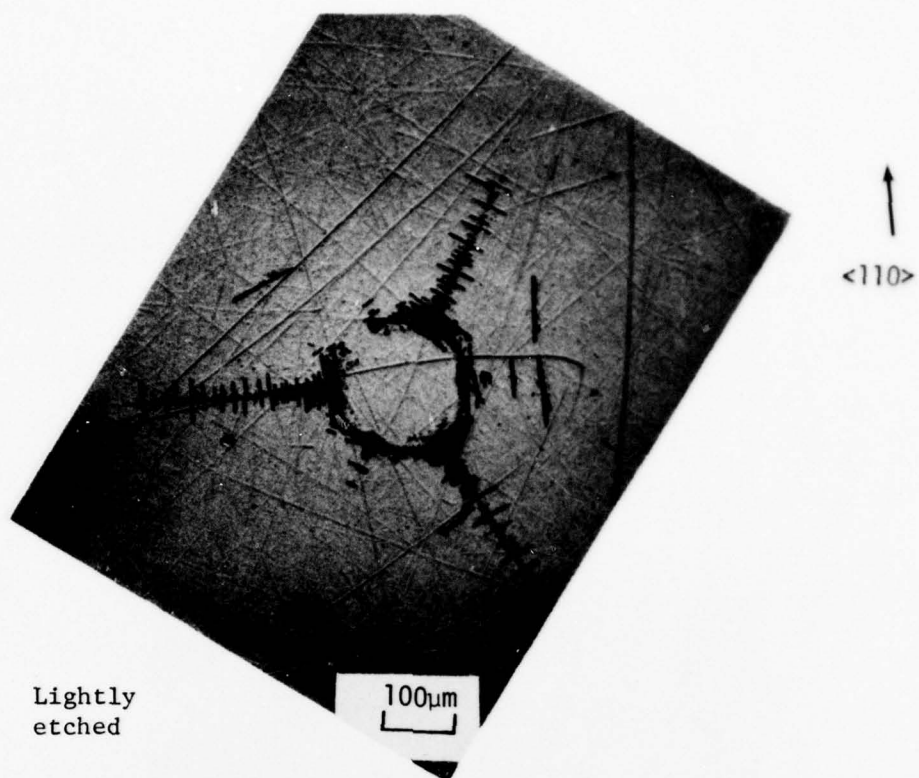


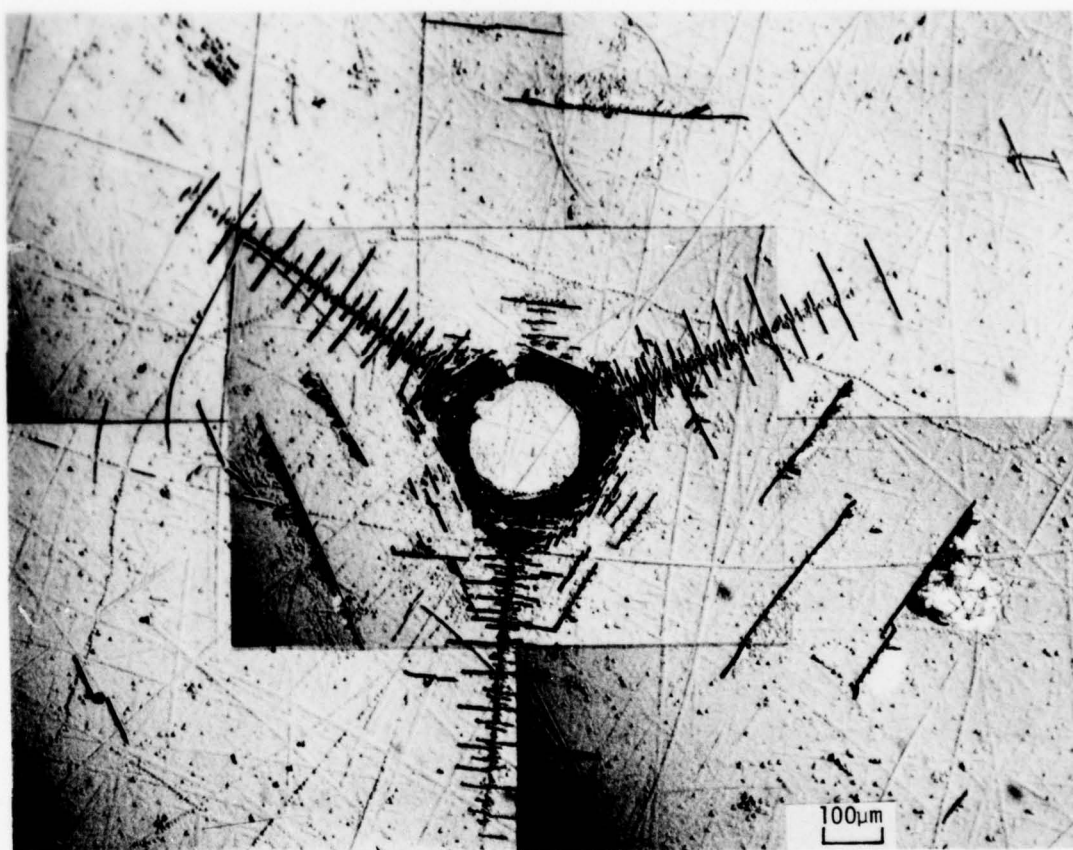
Figure 4.17. Dislocation Etched {111} Face of  $\text{CaF}_2$  Single Crystal Showing In Grown Dislocation Density and Low Angle Tilt Boundary.



a) Shot No. 995 at  $307 \text{ ms}^{-1}$

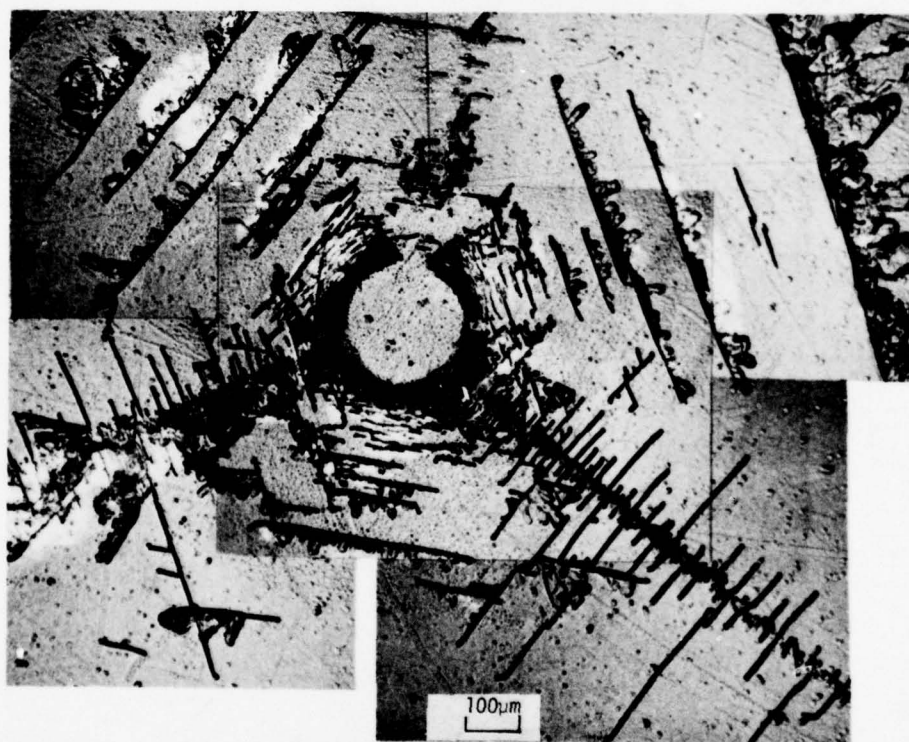
Figure 4.18. Dislocation Etched {111} Impacts on  $\text{CaF}_2$ .





$\angle 110^\circ$       b. Shot No. 947 at  $404 \text{ ms}^{-1}$ .

Figure 4.18. (continued)



c. Shot No. 975 at  $512 \text{ ms}^{-1}$ .

$\langle 110 \rangle$

Figure 4.18. (continued)

Although somewhat difficult to discern from the polishing damage present, the dislocations due to impact tend to appear in three areas and in numbers which increase with impact velocity. The three locations are:

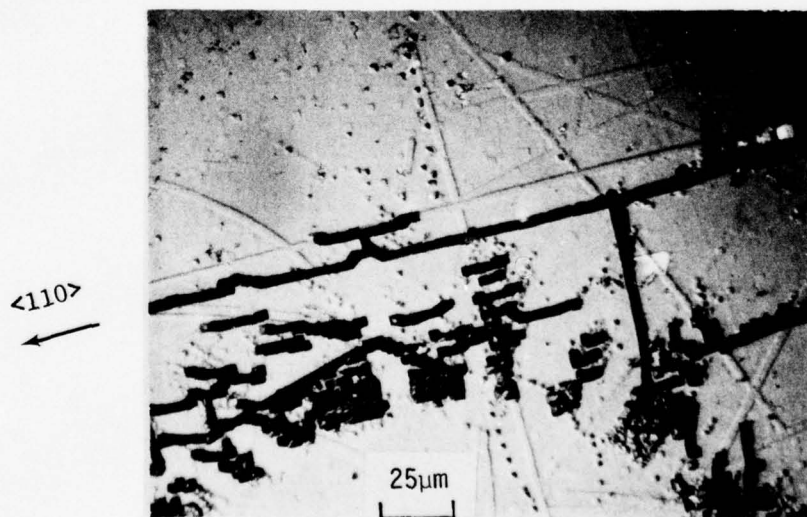
- (1) Three sectors of the central unfractured zone,
- (2) Along the axis of the three dominant radial fracture directions, and
- (3) The exterior region of the larger fractures.

The loosely organized slip bands lie in the three  $\langle 110 \rangle$  directions in the (111) impact plane. Assuming these dislocations are associated with the primary slip system  $\{100\} \langle 110 \rangle$ , their slip plane is a  $\{100\}$  plane which makes an angle of  $54.74^\circ$  with the impact surface; and their Burgers vector is either in the  $\langle 110 \rangle$  direction lying in the (111) impact plane coincident with the slip band or in the orthogonal  $\langle 110 \rangle$  direction. Their geometry can be more easily seen with reference to Fig. 4.19. Based on our examination of MgO in which there is no deformation in directions in the impact plane, the Burgers vector for the slip bands in  $\text{CaF}_2$  is most likely in the  $[\bar{1}10]$  direction.

Dislocation etching water drop impact damage on  $\{001\}$  oriented  $\text{CaF}_2$  also revealed individual dislocations and slip bands. Micrographs of etched (001) impacts at  $332 \text{ ms}^{-1}$  and  $528 \text{ ms}^{-1}$  are provided in Fig. 4.20. Again as for the (111) impacts, there is much less dislocation activity than for an equivalent impact on (001) MgO. Also as in the  $\{111\}$  impacts the dislocation activity increases with impact velocity. At an impact velocity of  $528 \text{ ms}^{-1}$  the dislocations tend to arrange themselves in fairly well-defined slip bands which intersect the (001) surface in the  $[010]$  and  $[100]$  directions. This behavior is consistent with the  $\{100\} \langle 110 \rangle$  slip system for  $\text{CaF}_2$ . The active slip planes for the slip bands on the surface are (100) and (010) which are both orthogonal to the (001) impact surface and to each other. The Burgers vector

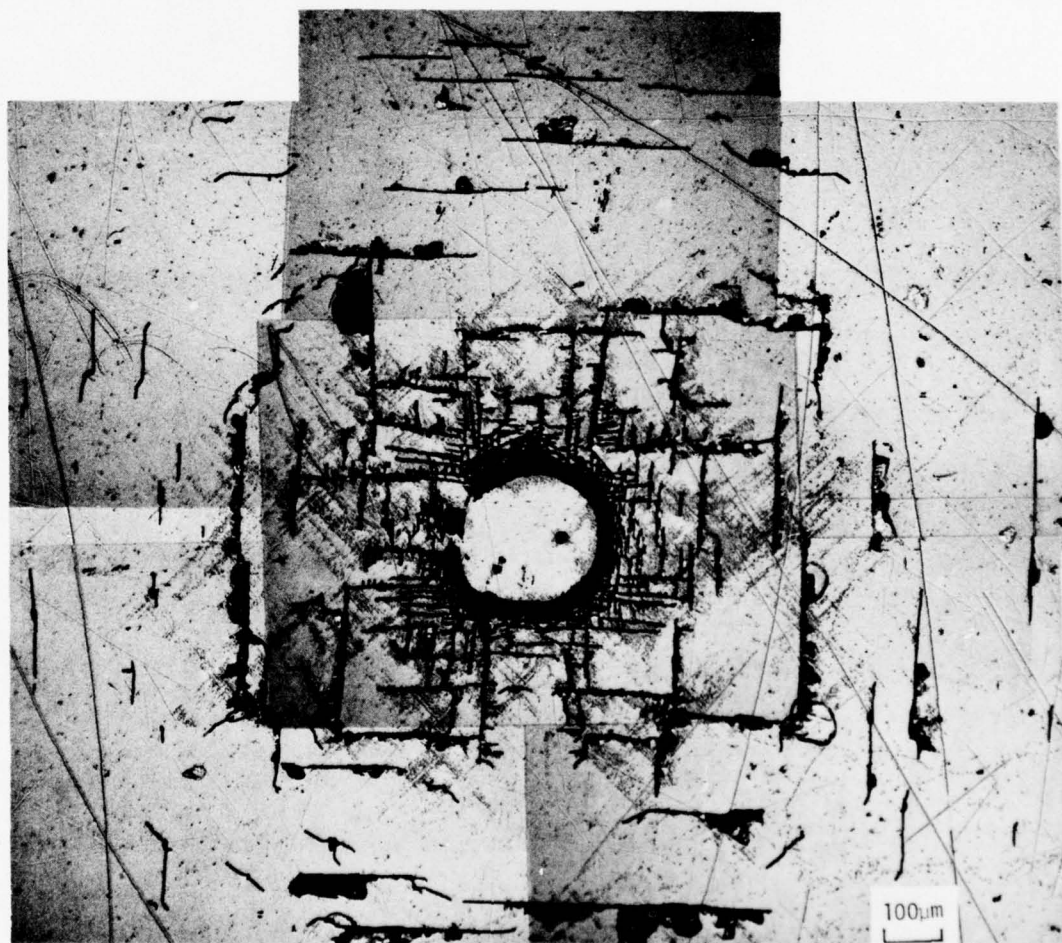






a) Shot No. 999 at  $332 \text{ ms}^{-1}$

Figure 4.20. Dislocation Etched {100} Impacts on  $\text{CaF}_2$ .



b. Shot No. 987 at  $528 \text{ ms}^{-1}$ .

$\downarrow$   $\langle 110 \rangle$

Figure 4.20. (continued)

for these slip planes are the four  $\langle 110 \rangle$  directions which make a  $45^\circ$  angle with the surface. There are only four sectors in which these slip systems allow displacement down from the surface and radially out from the impact. These sectors are centered about the four  $\langle 110 \rangle$  radial directions and can be seen in Fig. 4.20b to have the most dislocation activity both in the central unfractured region and exterior to the dense band of fractures.

The fact that  $\text{CaF}_2$  responds to water drop impacts in a significantly less ductile manner than  $\text{MgO}$  comes as little surprise when the critical resolved shear stress and fracture surface energies are compared. Experimentally measured values are listed in Table 4.3. From these values it is apparent that  $\text{MgO}$  not only yields at a lower stress<sup>\*</sup> but requires much more energy to create a fracture surface.

#### 4.2.3 Fracture Geometries

As pointed out in the previous section,  $\text{CaF}_2$  has a much lower fracture energy than  $\text{MgO}$  and exhibits considerably more impact fractures for both  $\{111\}$  and  $\{100\}$  orientations than  $\text{MgO}$ . Both  $\{111\}$  and  $\{100\}$  impacts have a characteristic fracture pattern for the velocity range investigated. For  $\{111\}$  impacts the intersections of the fractures with the impact face can be seen in Fig. 4.18 for impact velocities of 307, 404, and  $512 \text{ ms}^{-1}$ . The morphologies of the fractures below the surface are revealed on the  $(110)$  cross section orthogonal to the surface passing through the impact center in Fig. 4.21. The characteristic fracture pattern on the surface of a  $\{001\}$  impact on  $\text{CaF}_2$  can be seen in Fig. 4.20 for impact velocities of 332 and  $528 \text{ ms}^{-1}$ . The subsurface behavior of the fractures can be seen in Fig. 4.22.

Observation of the fractures on the impact face and in cross section indicates that for both the  $\{111\}$  and  $\{001\}$  impacts the fractures tend to lie almost entirely on the  $\{111\}$  cleavage planes. For

---

\* The values are for quasistatic deformations; the relative differences are used as a first approximation to the dynamic values.

TABLE 4.3. FRACTURE DATA FOR SINGLE CRYSTALS.

<u>CRYSTAL</u>	<u>CRITICAL RESOLVED SHEAR STRESS (MPa)</u>	<u>FRACTURE SURFACE ENERGY (J/m<sup>2</sup>)</u>	<u>RATIO OF FRACTURE ENERGY TO CRITICAL SHEAR STRESS</u>
<u>MgO</u>			
{110} <110>	37.0 <sup>a</sup>		.032
{001}		1.2 <sup>b</sup> 1.15 $\pm$ 0.80 <sup>c</sup> 1.15 <sup>d</sup>	
<u>CaF<sub>2</sub></u>			
{100} <110>	50.0 <sup>e</sup>		.009
{111}		0.45 <sup>b</sup>	
{111} <110>		0.51 <sup>f</sup>	
{111} <112>		0.80 <sup>f</sup>	
<u>LiF</u>			
{110} <110>	5.4 <sup>g</sup>		.063
{001}		0.34 <sup>b</sup>	

a) Stokes, et al., 1959a.

b) Gilman, 1960.

c) Westwood and Goldheim, 1963.

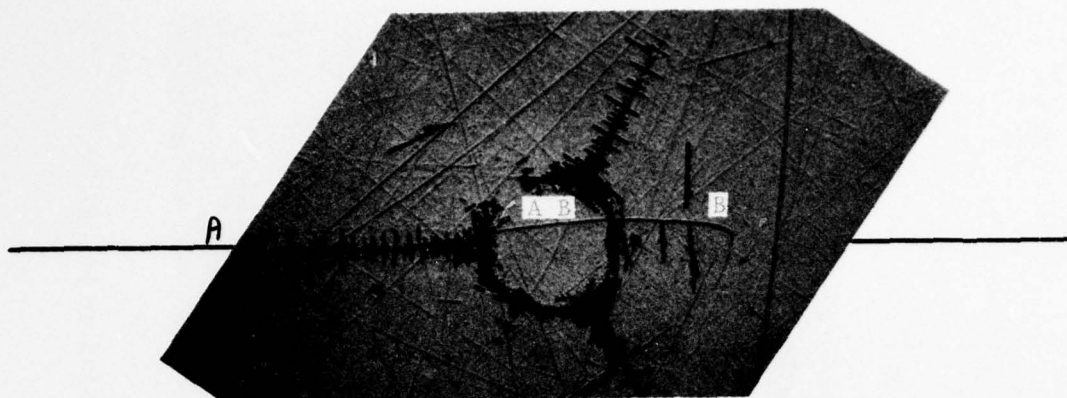
d) Ahlquist, 1974.

e) Phillips, 1961.

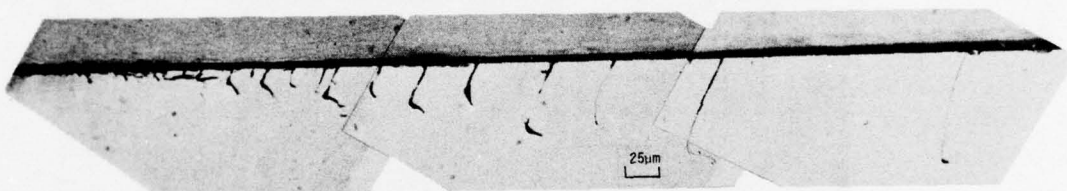
f) Freiman, et al., 1976.

g) Gilman and Johnston, 1957.

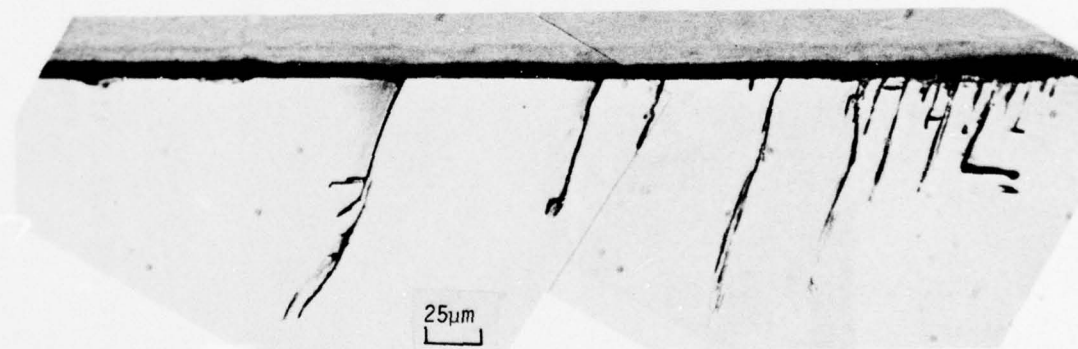




a. Location of cross section on impact site.



b. Section A-A.



c. Section B-B.

Figure 4.21. (110) Cross Section of Water Drop Impact on {111}  $\text{CaF}_2$  at  $307 \text{ ms}^{-1}$ .

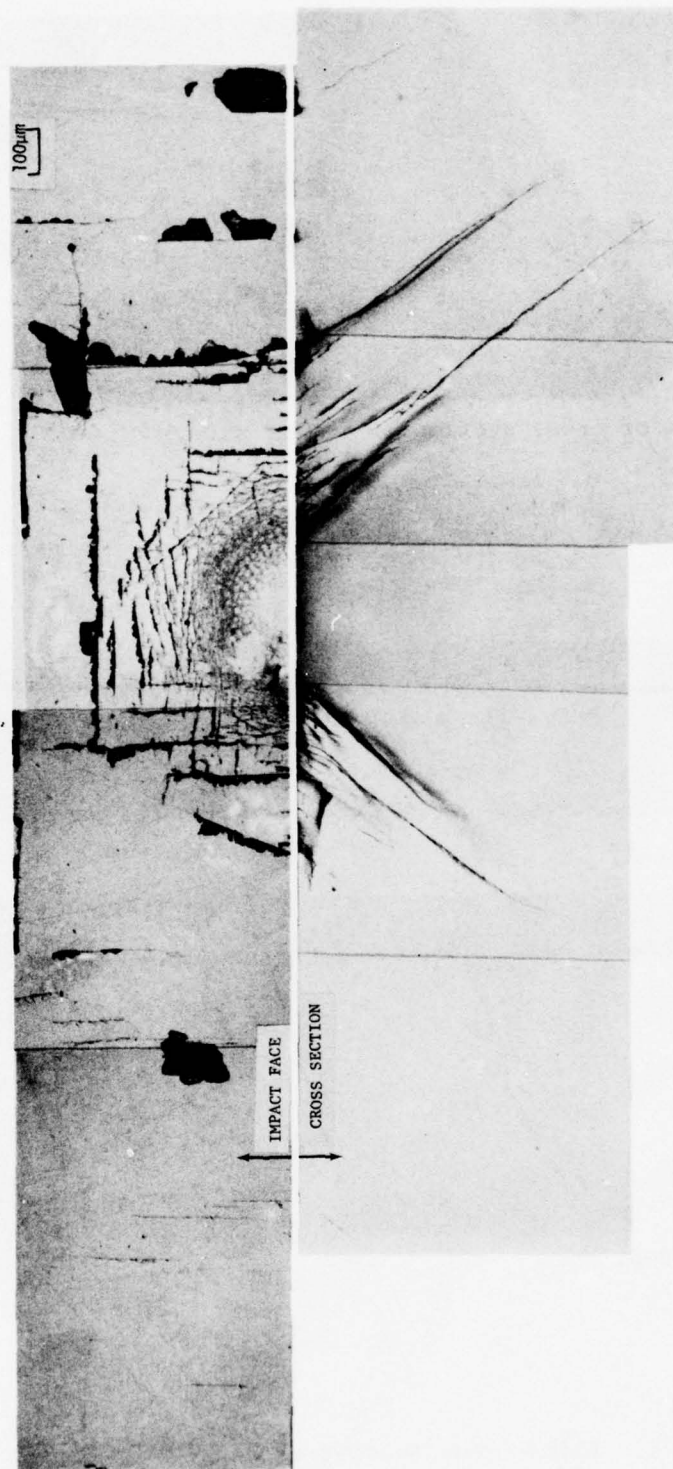


Figure 4.22. (100) Cross Section of a Water Drop Impacting at  $548 \text{ ms}^{-1}$   
(Shot no. 914) on (001)  $\text{CaF}_2$ .

the {111} impacts the fractures are predominantly on the three {111} planes which intersect the {111} impact surface at 70.53° and for the {100} impacts the fractures are almost entirely on the four {111} cleavage planes which intersect the surface at 54.74°. The strong preference of the fractures to follow the {111} fracture planes is apparent in Fig. 4.21a. The fractures change from the {111} cleavage at 70.53° to the surface to the {111} cleavage plane parallel to the surface. This strong preference to fracture on the {111} cleavage plane is most likely the result of significantly higher fracture energies required for other planes.

The mechanisms responsible for initiating the above-mentioned fractures appear to be somewhat different than for the (001) impacts on chemically polished MgO. Dislocation and slip band interactions were concluded to be operative in (001) impacted MgO. O'Neill, et al. (1973), have observed an absence of fractures due to dislocation interactions for both hardness and friction experiments in CaF<sub>2</sub> under conditions that MgO and LiF fractured due to dislocation interactions. They attribute this to the inability of the {100} <110> slip system in CaF<sub>2</sub> to produce sessile coalescing dislocations. Phillips (1961) proposed a method by which fracture on a {100} plane could be initiated according to the equation,

$$1/2 a [\bar{0}11] + 1/2 a [0\bar{1}1] = a[0\bar{1}0]$$

However Phillips also observed that it is not possible to initiate a fracture on a {111} plane by dislocation reactions. The method proposed by Argon and Orowan (1964) for MgO whereby fractures are initiated due to the nonaccommodation of deformation at slip band intersections may also be active in CaF<sub>2</sub> impacts.

In contrast to MgO, surface flaws in mechanically polished CaF<sub>2</sub> specimens seen to be the primary fracture nucleation sites when favorably oriented with the {111} fracture planes. To date we have been unable to prepare a surface with a relatively low initial flaw distribution

or a chemically polished surface on  $\text{CaF}_2$  specimens. As can be seen in the etched micrographs of (100) and (111) impacted  $\text{CaF}_2$ , there are numerous polishing scratches which have interacted with the fracture pattern to enhance the fracture damage.

#### 4.3 LITHIUM FLUORIDE

Water drop impact damage on lithium fluoride single crystals which is considerably softer than either  $\text{MgO}$  or  $\text{CaF}_2$  was also investigated.  $\text{LiF}$  exists in the same rock salt cubic crystal structure as  $\text{MgO}$  and has the same  $\{110\} \langle 110 \rangle$  primary slip systems.

##### 4.3.1 Specimen Preparation and Characterization

Single crystal lithium fluoride ( $\text{LiF}$ ) in the form of  $\{100\}$  cleaved and annealed blocks approximately  $12 \times 12 \times 8$  mm were purchased from Harshaw Chemical Co., Solon, Ohio. Spectrographic analysis performed by Harshaw indicates trace impurities of calcium, magnesium, and silicon.

The as-received crystals contained cleavage steps and deformation damage on the surfaces. The following procedure was used to prepare the surfaces for impact.

- (i) The cleaved surface was mechanically polished flat.
- (ii) The flat surface was then chemically polished with fluorboric acid at room temperature until the damaged layer due to mechanical polishing was removed.
- (iii) Since (ii) left a microscopically rough surface, the specimen was given a dislocation etch (Johnston, 1962), which left the surface generally smooth with the ingrown dislocation content revealed (see Fig. 4.23). The ingrown dislocation density was on the order of  $3 \times 10^5/\text{cm}$  not counting those present in the low angle tilt boundaries.



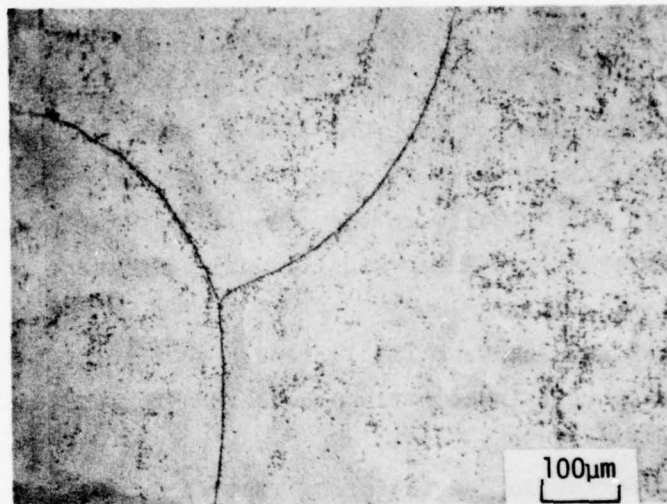


Figure 4.23. Lightly Dislocation Etched (001) Surface of LiF Prepared for Impact Revealing In-grown Dislocation Content and Low Angle Tilt Boundaries.

(001) LiF specimens were subjected to the water drop impact conditions listed in Table 4.2. After removal from the sabot and careful removal of recovery debris by washing in methanol and ether, the impact sites could generally be identified by transmitted polarized light. Application of a dislocation etchant (Johnston, 1962) revealed characteristic fractures and slip bands. The slip bands will be discussed first.

#### 4.3.2 Dislocation Slip Bands in (001) Impacted LiF

Although there are many background dislocations, the slip band pattern due to impact at  $385 \text{ ms}^{-1}$  on (001) LiF can be seen in Fig. 4.24. Analogous to (001) MgO impacts, the slip bands appear almost entirely in the  $\langle 100 \rangle$  directions on the (001) face. Since both LiF and MgO slip on  $\{110\}$  planes in  $\langle 110 \rangle$  directions, a similar response is not unexpected. Although LiF and MgO slip on the same  $\{110\} \langle 110 \rangle$  systems, their critical resolved shear stresses are significantly different.

Gilman and Johnston (1957) report a critical resolved shear stress of 5.4 MPa for LiF in comparison to 37 MPa for MgO and 50 MPa for  $\text{CaF}_2$  (as summarized in Table 4.3). The much softer nature of LiF allowed bulk specimen deformation due to forces imposed during launching and recovery at velocities greater than  $400 \text{ ms}^{-1}$ . These deformations made identification of the slip bands due to impact extremely difficult to isolate from those due to launch and recovery at the higher velocities.

Two investigations of water drop impacts on annealed single crystals of LiF are available for comparison with our findings. Jolliffe (1966) examined the impact damage associated with 1.5 and 2.5 mm water drops impacting from  $15$  to  $65 \text{ ms}^{-1}$ , and Hoagland and Jung (1978) studied the effects of 0.4 mm water drops impacting at  $96$  and  $134 \text{ ms}^{-1}$ . In both cases water drop collisions were produced in a whirling arm configuration, whereby the specimen is mounted at the end of a propeller blade and passes through a single stream of falling water drops during each revolution. Experimental details are quite scant in both accounts.

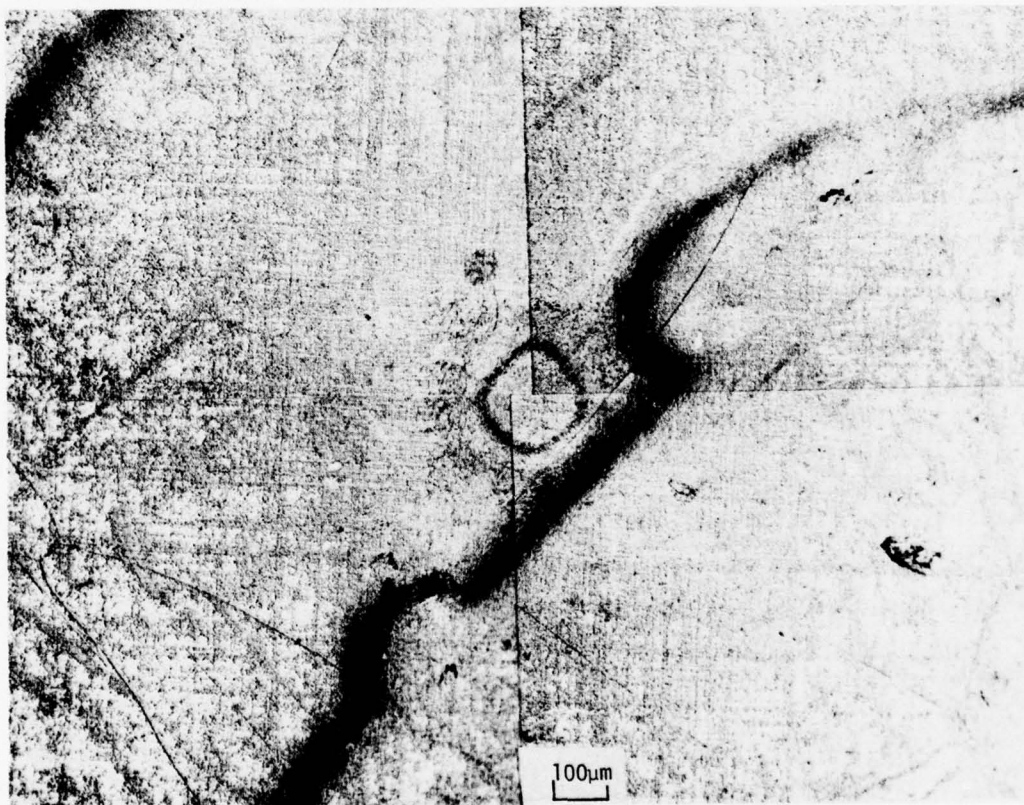


Figure 4.24. Dislocation Etched Water Drop Impact on (001) LiF at  $385 \text{ ms}^{-1}$  (Shot no. 980). (The dark band is the remnants of a chemically polished cleavage step.)



In order to compare with the observations reported water drop impacts were undertaken in the vicinity of  $200 \text{ ms}^{-1}$ , which is the lower velocity conveniently achieved in the power gun. For confirmed single drop impacts at  $200 \text{ ms}^{-1}$  there is very little bulk deformation of the specimen and changes in the impact surface dislocation structure are observable. Shot no. 1002 ( $209 \text{ ms}^{-1}$ ) was one of the shots specified to investigate the response of (001) LiF at or near the damage threshold. After lengthy and detailed observation of the etched impact surface, no significant change was attributable to the water drop impact, although several small (up to  $100 \mu\text{m}$ ) clusters of  $\{110\}_{45^\circ}$  and  $\{110\}_{90^\circ}$  slip bands were located on the surface. The fact that the clusters observed in shot no. 1002 are randomly spaced over distances considerably greater than the drop diameter and that there are several make them very unlikely to be the result of the single water drop impact.

Hoagland and Jung (1978) report seeing very similar clusters which they attribute to water droplet impacts on (001) annealed and irradiated LiF at velocities of 96 to  $160 \text{ ms}^{-1}$ . As is apparent for the higher velocity drop impacts on LiF and as has been discussed in some detail for MgO and  $\text{CaF}_2$ , the predominant mode of deformation due to water drop impact is slip in directions away from the surface and not in directions in the surface. The  $\{110\}_{90^\circ}$  slip systems constitute slip in the surface and their presence in the clusters observed in shot no. 1002 and by Hoagland and Jung indicate the clusters are the result of something other than a water drop impact.

Jolliffe (1966) also reports seeing small clusters of dislocations on multiply-impacted annealed LiF at velocities from 15 to  $66 \text{ ms}^{-1}$ . The clusters Jolliffe observed showed a strong predominance of slip on the  $\{110\}_{45^\circ}$  slip systems and much less activity on the  $\{110\}_{90^\circ}$  systems compared to solid sphere impacts. The observation of slip being predominantly on the  $\{110\}_{45^\circ}$  systems agrees with the single drop impact observations for LiF, MgO, and  $\text{CaF}_2$ . However the presence of  $\{110\}_{45^\circ}$  slip



can also be the result of an initial incident which introduced the dislocation cluster followed by preferential growth and expansion of the  $\{110\}_{45^\circ}$  slip bands present in the cluster by subsequent drop impacts. Expansion of previously introduced slip bands by water drop impacts has been observed in MgO (Adler and Hooker, 1977) as well as in mechanically polished MgO discussed in Section 4.1.3.

In addition to dislocation clusters Hoagland and Jung (1978) report evidence of rearrangement or motion due to water drop impact of the in-grown dislocations in annealed LiF. The post-impact analysis of shot no. 1002 did not preclude rearrangement due to impact of the initially present dislocations. It appears that an impact at  $209 \text{ ms}^{-1}$  is below the threshold for introduction of organized slip bands and fracture patterns in annealed LiF, although some motion of dislocations occurs. Furthermore the stresses generated by an 0.4 mm water drop are significantly lower than those for a nominal 1.5 mm drop size.

Hoagland and Jung and Jolliffe comment that there are far fewer dislocation clusters present than the estimated number of drop impacts. In both experiments the quantity and form of the water which impacts the surface is completely unknown. These procedures contribute relatively little to understanding the nature of the damage produced by water drop collisions on LiF.

#### 4.3.3 Impact Fracture Patterns on (001) LiF

Not only are the slip band patterns very similar for (001) impacts on LiF and MgO but so are the fracture patterns. Fig. 4.25 is a view of the fracture annulus for an impact at  $385 \text{ ms}^{-1}$  which appears quite similar to the fracture annulus for MgO in Fig. 4.5a. Due to the similar fracture and slip band behavior compared with MgO, the discussion of fracture initiation in MgO presented in Sections 4.1.2 and 4.1.3 also applies to LiF.

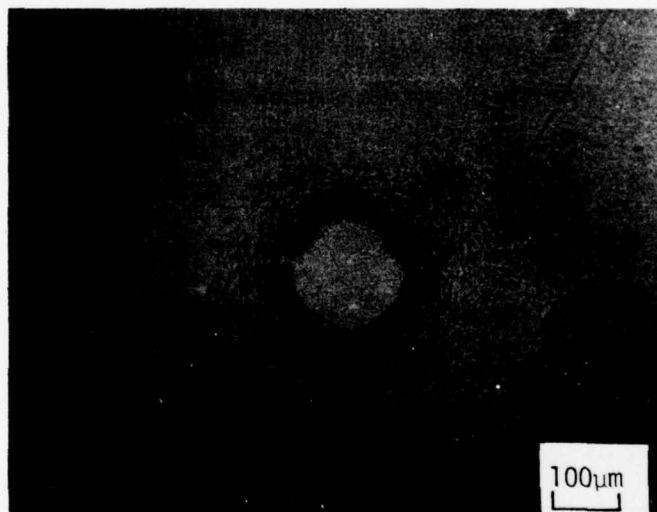


Figure 4.25. Fracture Annulus for Shot No. 980 (Impacted at  $385 \text{ ms}^{-1}$ ) Viewed in Transmitted Light.

For water drop impacts on LiF there is a strong dependence of slip and fracture extent on impact velocity. As previously pointed out an impact velocity of  $209 \text{ ms}^{-1}$  is below the threshold for introduction of organized slip or fracture. Impacts at  $385 \text{ ms}^{-1}$  are very similar to those on MgO at  $560 \text{ ms}^{-1}$ . Impacts at  $555 \text{ ms}^{-1}$  on annealed LiF display what appears to be a more advanced development of the fracture pattern seen at  $385 \text{ ms}^{-1}$ . Fig. 4.26 shows the fractures visible without etching due to an impact at  $555 \text{ ms}^{-1}$ . The interior fractures which are revealed by etching have the same character as the fractures due to a  $385 \text{ ms}^{-1}$  impact. The larger fractures developed at high velocity impacts are extensions of the "W"-shaped fractures observed in MgO (Fig. 4.13). Assuming no change in the fracture mode, the extent of the fractures in MgO may be scaled with respect to the fractures produced in LiF at considerably lower velocities. The validity and form of the correlation require further investigation.

The similarity in impact response of MgO and LiF can be attributed to a high ratio of fracture energy to critical resolved shear stress in addition to identical slip and fracture systems. Values of the fracture energy and critical resolved shear stress are listed in Table 4.3.  $\text{CaF}_2$  in contrast to LiF and MgO does not have as large a ratio of fracture energy to critical resolved shear stress and the energy due to water drop impact is dissipated predominantly by fracture rather than slip.



Figure 4.26. Unetched Water Drop Impact on (001) LiF at  $555 \text{ ms}^{-1}$  (Shot no. 915).



## 5.0 SOFT PARTICLE SIMULATION OF WATER DROP IMPACT DAMAGE

As pointed out in the Introduction, solid particle simulations of water drop impact damage effects have been attempted in the past with generally negative results (e.g., Engel, 1955; Fyall, 1967; Lankford, et al., 1973). Our motivations for pursuing what appears to be a futile undertaking are: (1) there is a need for the attainment of water drop impacts on tough ceramic materials at impact velocities approaching  $2400 \text{ ms}^{-1}$  (Mach 7) on a cost-effective basis, (2) soft solid particle impacts are frequently assumed to simulate the effects of water drop collisions without adequate justification, and (3) propelling particles, in a manner analogous to water jets, affords a considerably broader range of impact conditions and specimen selection than is possible using water drops.

The differences in the loading conditions for hard solid particles, nylon beads, and water drops have been described (Adler and Hooker, 1977). A comparison between solid particle and water drop impact damage is worthwhile, since it is much easier to propel a solid particle at a fragile target at high velocity than to propel the target material into a water drop. The first alternative removes the restriction on geometry of the test specimen and eliminates the specimen recovery problem which at high velocities requires an elaborate experimental facility. The technology is currently available for propelling soft particles to velocities in excess of  $4000 \text{ ms}^{-1}$  and hard solid particles to even greater velocities (Carlyle, et al., 1975).

It is not our intention to demonstrate that the soft body simulation is a universal relationship but to show that it may be a valid approach for restricted classes of materials. Some evidence in support of this hypothesis has been acquired for CVD zinc sulfide using nylon beads. Characterization of water drop impact damage on CVD zinc sulfide is currently in progress (research supported under Contract F33615-78-C-5143

with the Air Force Materials Laboratory) over a velocity range from 222 to 684 ms<sup>-1</sup>. Some of the impact data will be used from this program for comparison with nylon bead impacts. CVD zinc sulfide was selected for investigation since it had already been used in particle impact programs funded by the Office of Naval Research.

Evans and Wilshaw (1976) examined the dynamic fracture characteristics of CVD zinc sulfide due to 500  $\mu$ m nylon beads impacting over a velocity range from 406 to 1000 ms<sup>-1</sup> as part of a broader study. The damage created on brittle surfaces by particle impacts is classified as either elastic or elastic/plastic response. The authors distinguish between these two regimes as follows. In the elastic regime the maximum tensile stresses are the radial stress components. The radial stresses produce circumferential cracks which initiate at the surface and propagate into the target material. In the elastic/plastic regime the maximum tensile stresses occur near the surface and are the circumferential components of the stress tensor. This stress condition produces radial cracks which propagate outward along the surface, while below the surface the maximum tensile stresses create subsurface lateral fractures. Evans and Wilshaw state that the damage produced by nylon beads is similar in appearance to the damage due to water drop impacts in that both impact conditions produce a damage annulus consisting of a series of approximately concentric circular crack segments.

The nylon bead impacts on zinc sulfide represent the elastic response regime: other impact conditions were considered by Evans and Wilshaw to investigate the nature of the fractures in the elastic/plastic regime. These investigators divided the damage region into a contact zone (the central undamaged region) and a concentric damage annulus. The damage annulus is then divided into an inner annulus and an outer annulus as defined by the two distinct forms of the fracture trajectories they identified in sectioned specimens. For the nylon bead impacts they found that the cracks in the inner annulus were nearly normal to the impact face at the specimen's surface, but quickly tended to follow a trajectory

approximately parallel to the impact surface which propagated outward from the point of impact. The cracks in the outer annulus penetrated somewhat deeper and were primarily straight cracks inclined  $50^\circ$  to the impact surface. On the basis of Evans and Wilshaw's observations, the character of the damage in the damage annulus is quite different from that which is found for water drop collisions as displayed in Fig. 5.1. Evans and co-workers measured the lengths of the circumferential surface cracks and their radial distribution but did not investigate the attributes of the nylon bead impacts which contribute to the general character of the subsurface fracture trajectories. The subsurface damage is of major concern in the present program.

We are in a position to investigate the extent to which this comparison may be valid. The property data provided for the CVD ZnS used in the experiments of Evans and co-workers indicates it probably had a grain size of 30 to 40  $\mu\text{m}$  (Evans, et al., 1976; Evans, et al., 1977), fracture toughness of  $1\text{MN/m}^{3/2}$  (Evans and Charles, 1976), Young's modulus of 102 GPa, and a Knoop hardness of  $194\text{ kg/mm}^2$ .<sup>\*</sup> Grain size measurements were made by us on two lots of CVD ZnS as summarized in Table 5.1. The 100 g Knoop hardness of material A was  $238\text{ kg/mm}^2$  and  $194\text{ kg/mm}^2$  for material B. The revised grain size (see footnote) and hardness from Evans' work agree favorably with material B for the growth plane parallel to the surface of the specimen. Equiaxed grains in three dimensions do not appear to be a characteristic of CVD ZnS. For material A Young's modulus is 100.8 GPa and the fracture toughness is  $0.67\text{ MN/m}^{3/2}$  (Wimmer and Graves, 1977).

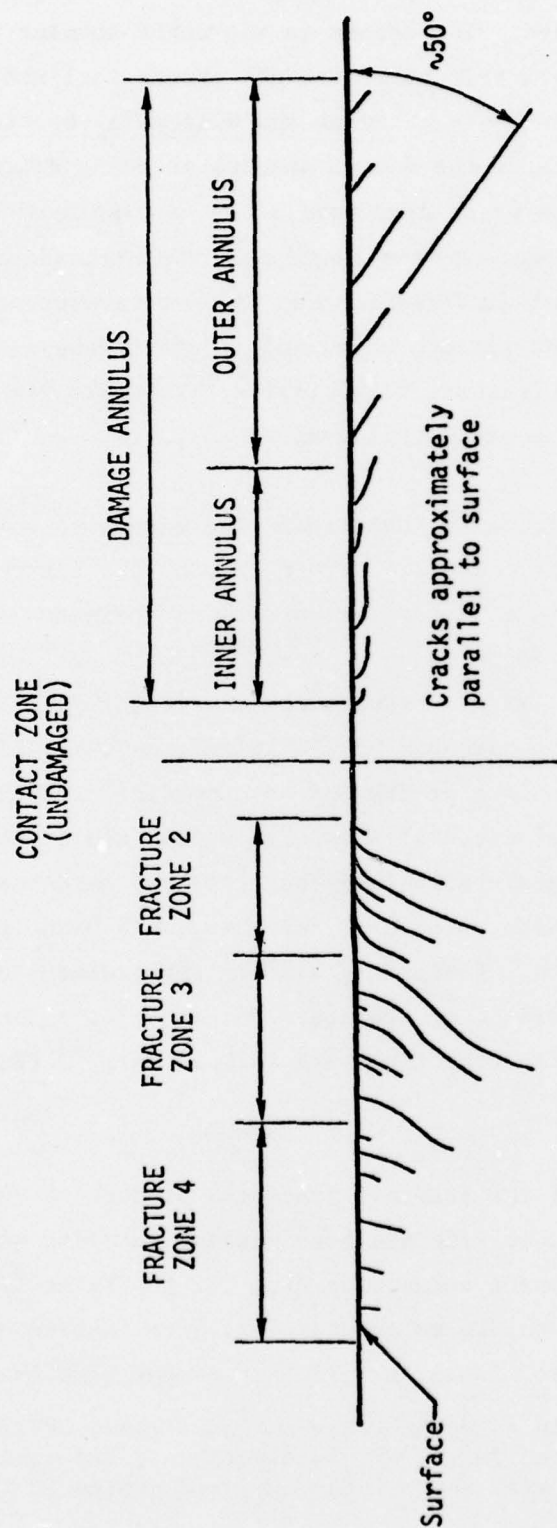
The character of the internal fractures produced by water drop collisions on CVD zinc sulfide has been studied on cross sections through the impact site for impact velocities from 222 to  $684\text{ ms}^{-1}$ . Experiments with nylon beads, 0.5 to 2.0 mm in diameter, were carried out in the same manner as the water drop impact experiments except that the nylon beads

<sup>\*</sup>Dr. Evans indicated in a recent conversation (Evans, 1979) that the same lot of CVD ZnS was used in all of his experiments and that the average grain size was 10  $\mu\text{m}$  with essentially equiaxed grains in three dimensions.



FRACTURE PATTERN FOR 500  $\mu\text{m}$   
 NYLON BEAD IMPACTING FROM  
 406 to 1000  $\text{ms}^{-1}$  (Evans and Wilshaw, 1976)

FRACTURE PATTERN FOR 1.3 mm  
 WATER DROP IMPACTING FROM  
 222 to 684  $\text{ms}^{-1}$



NOT TO SCALE

Figure 5.1. Schematic Representation of the Observed Subsurface Fracture Patterns for Water Drop and Nylon Bead Impacts on CVD Zinc Sulfide.



Table 5.1. Grain Size Dimensions  
for CVD Zinc Sulfide

	AVERAGE INTERCEPT DIMENSION ( $\mu\text{m}$ )
<u>MATERIAL A</u>	
Growth Plane (equiaxed grains)	3 to 4
Plane Perpendicular to Growth Plane (columnar grains)	
Direction Parallel to Growth Plane	3 to 4
Direction Perpendicular to Growth Plane	5 to 30
<u>MATERIAL B</u>	
Growth Plane (equiaxed grains)	8 to 10
Plane Perpendicular to Growth Plane (columnar grains)	
Direction Parallel to Growth Plane	5 to 10
Direction Perpendicular to Growth Plane	10 to 100

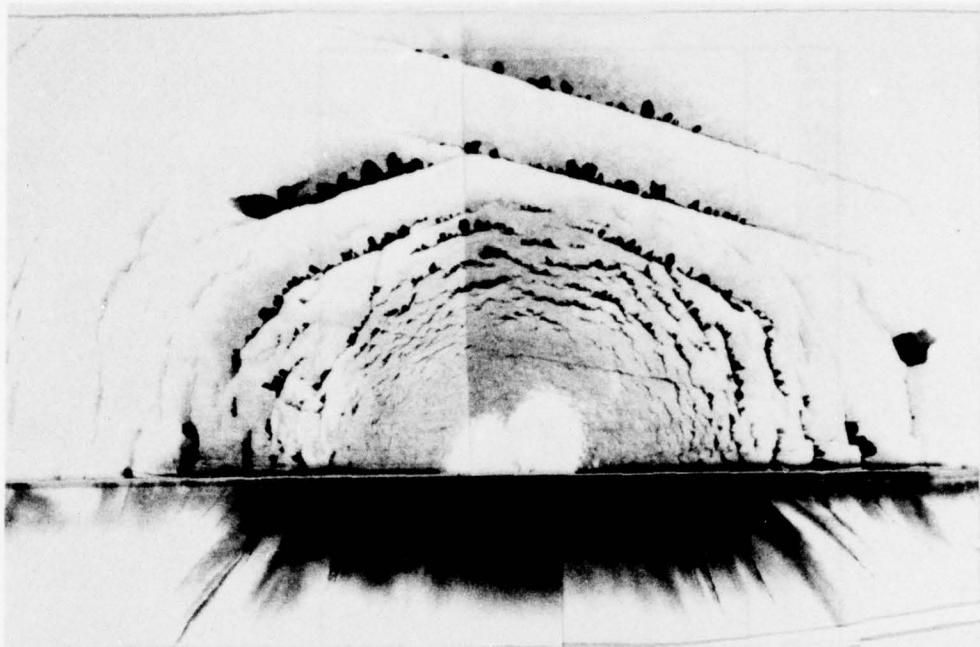
were suspended in the path of the moving specimen. The general character of the subsurface crack patterns for nylon bead collisions was found to be quite similar to the observed crack patterns for water drop impacts in contrast to the comparison shown in Fig. 5.1. In reexamining the work of Evans and Wilshaw (1976), the same bead diameter, 500  $\mu\text{m}$ , and impact velocity in the range they investigated were used to ascertain if their observations were due to a particle size effect; however, this does not appear to be the source of the discrepancy. The nature of the subsurface fractures remains unchanged for particle diameters from 0.5 to 2.0 mm.

The impact conditions for and the measurements made on the nylon bead and water drop impacted specimens are tabulated in Table 5.2. The boundaries of the fracture zones defined in Fig. 5.1 for nylon bead impact N3 show reasonable agreement with the boundaries for water drop impacts A5 and A6, however the maximum fracture depths for shot no. N3 agree more closely with the higher velocity water drop impact. Comparing the relevant dimensions for nylon bead impacts N2 and N3, there is some basis for speculating that a slight decrease in the diameter of the 2 mm bead may produce a significant difference in the fracture depths. Unfortunately it is difficult to establish equivalent relations between the two impact conditions analytically due to the lack of information pertaining to the dynamic constitutive relations for the nylon formulations from which the beads are made (Adler and Hooker, 1977). Surface and cross section views of particle impacts A5 and N3 are shown in Fig. 5.2. The lack of lateral outflow damage on the surface of the nylon bead impact specimen is evident. The discrepancy in the penetration depth of the fracture is also obvious, although this difference may be minimized by experimentally determining roughly equivalent impact conditions. However the sectioned specimens do reveal that the fracture configurations within each fracture zone are essentially the same for nylon beads and water drops of comparable size and impact velocity.

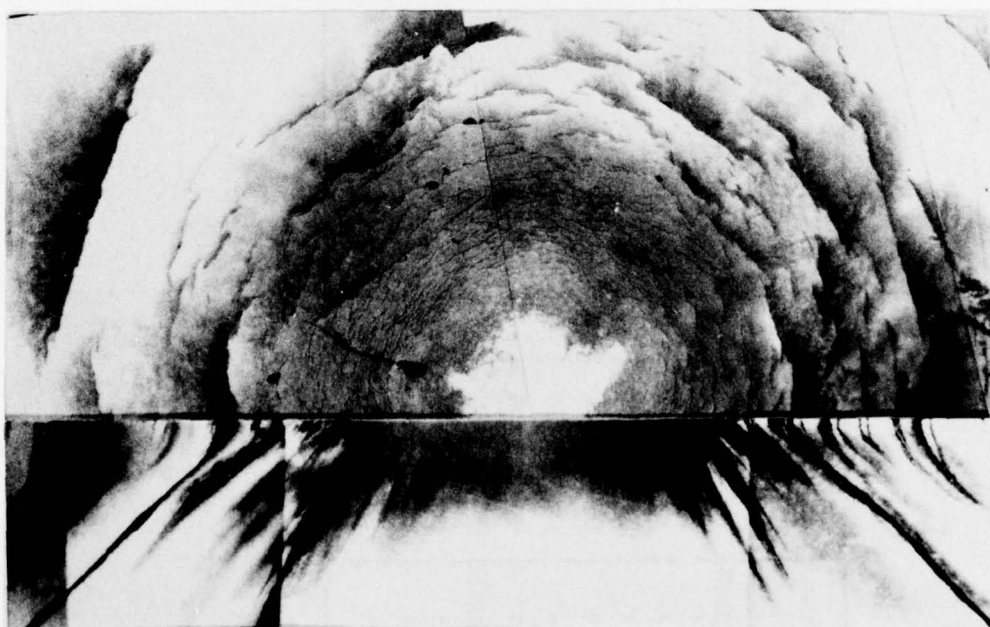
Table 5.2. Summary of Particle Impact Damage Dimensions on CVD Zinc Sulfide.

SHOT NO.	MATERIAL	IMPACT VELOCITY ( $\text{ms}^{-1}$ )	EQUIVALENT DROP DIAMETER	$b_1/b_2$	MAX. RADIUS of Zone 1 (mm)	MAX. RADIUS of Zone 2 Min. (mm) Max. (μm)	FRACTURE DEPTH Min. (μm) Max. (μm)	MAX. RADIUS of Zone 3 (mm) Max. (μm)	FRACTURE DEPTH Min. (μm) Max. (μm)	MAX. RADIUS of Zone 4 (mm) Max. (μm)	FRACTURE DEPTH Min. (μm) Max. (μm)	LATERAL OUTFLOW BEGINS INITIATION (mm)	TERMINATION (mm)
WATER DROP IMPACTS													
A3	A	237	1.60	1.54	0.13	0.25 3 20	-- 40	-- 0.40	-- --	-- --	-- --	-- --	--
A4	A	368	1.56	1.67	0.16	0.42 2 180	2 270	0.60 1.00	50 100	0.32 0.70			
A5	A	518	1.78	1.24	0.18	0.65 10 520	8 320	1.15 2.30	5 120	0.46 1.15			
A6	A	640	1.96	1.18	0.25	0.80 5 1200	10 1000	1.75 3.80	5 540	0.39 1.35			
A12	A	372	1.91	--	0.18	0.40 5 280	10 240	0.65 1.20	30 150	0.20 0.85			
A14	B	350	1.85	--	0.14	0.40 5 150	10 200	0.75 1.10	20 100	0.30 0.80			
NYLON BEAD IMPACTS													
M1	A	~550	0.50	--	0.05	0.15 5 100	10 140	0.32 0.80	20 80	-- --			
M2	A	470	1.0	--	0.09	0.22 2 180	10 150	0.45 0.70	20 80	-- --			
M3	A	550	2.0	--	0.20	0.60 5 800	20 1000	1.50 2.50	20 600-700	-- --			





(a) 1.78 mm Water Drop Impact at  $518 \text{ ms}^{-1}$  (Shot No. A5)



(b) 2 mm Nylon Bead Impact at  $550 \text{ ms}^{-1}$  (Shot No. N3)

Figure 5.2. Surface and Subsurface Fractures Due to Particle Impacts on CVD zinc sulfide.



Detailed microscope examinations of several cross sections for both water drop and nylon bead impacts reveal that the general fracture configuration displays a radical change in character depending on whether the fractures are interior or exterior to a dominant conical fracture inclined approximately  $45^\circ$  to the impacted face of the specimen. This dominant fracture occurs near the outer boundary of fracture zone 2 as defined in Fig. 5.1. This inclined fracture is often the deepest penetrating fracture and is relatively straight. The 0.5 and 1.0 mm diameter nylon beads tend to produce fractures within this dominant cone crack which are inclined at  $70^\circ$  to the specimen's surface initially but gradually assume inclination angles which decrease toward  $45^\circ$  as the radial distance approaches the location of the  $45^\circ$  cone crack. These fractures display negligible curvature. The fractures in zone 2 for the 2 mm nylon bead impact, N3, conform more to the curvature pattern observed for comparable size water drop collisions. These details cannot be seen clearly on the micrographs in Fig. 5.2, but are shown in the schematic representation in Fig. 5.1.

There appears to be adequate support for further exploration of the correspondence between nylon bead and water drop impacts, but data is required over an expanded range of velocities and for nylon bead diameters which produce fracture depths closer to those found for well-formed spherical water drops.

## 6.0 CONCLUSIONS

An experimental facility has been developed for producing spherical water drop impacts on brittle ceramic materials at both subsonic and supersonic impact velocities. While spherical water drop collisions may seldom be encountered in actual flight conditions, they are quite useful in understanding the response of materials due to water drop impingement, correlating the observed fracture behavior with more conventional fracture evaluations, and for both formulating and comparing analytical and computational models of the impact event.

Detailed microscopic examination of polymethylmethacrylate subjected to well-characterized spherical water drop impacts has provided a reasonably comprehensive picture of its deformation and fracture response including several previously unknown features of the resulting damage. This information will form the basis for analytical studies of the impact process.

At impact velocities up to  $400 \text{ ms}^{-1}$  the dimension of the inner radius of the characteristic depressed annulus for polymethylmethacrylate compares favorably with the radius computed from the condition that the velocity of the expanding contact zone is equal to the shock velocity in water. It is doubtful that this correlation could have been substantiated without the experimental capability to provide confirmed spherical drop impacts, since the available data obtained in other facilities shows a variety of trends with respect to the impact velocity.

At the initiation of the investigation of water drop impact damage in single crystals of  $\text{MgO}$ ,  $\text{CaF}_2$  and  $\text{LiF}$ , it was thought that due to the high strain rates imposed slip and fracture might occur in systems and planes other than those associated with quasistatic deformations. However slip and fracture occurred in the same systems and planes that are active in quasistatic deformations for all three materials for the impact conditions considered.

Identification of the slip bands generated by water drop collisions using section and etch procedures revealed a characteristic of the water drop impact which is significantly different from solid particle impacts. The deformation due to water drop impacts is such that material is displaced in directions away from the impact plane and not in directions in the impact plane. Rounded solid particle impacts in contrast cause a displacement both in directions in the impact plane as well as away from it.

For impacts on (001) MgO it was demonstrated that introduction of numerous active slip sources into the impact face is an effective means for reducing the impact damage and completely eliminating fracture for the impact velocities tested which approached  $600 \text{ ms}^{-1}$ . The numerous active sources allow deformation to take place by slip (rather than fracture) at rates greater than can be accommodated by dislocation multiplication methods in surfaces with very few active sources. However the presence of numerous active slip sources in  $\text{CaF}_2$  was not sufficient to eliminate water drop impact fractures over the velocity range investigated.

The difference in the response of MgO which exhibits extensive slip and insignificant fracture, or none at all, and  $\text{CaF}_2$  which exhibits extensive crack growth and very limited slip can be attributed to their respective fracture energies and critical shear stresses. MgO has a much higher ratio of fracture energy to shear stress than  $\text{CaF}_2$ , therefore the preference of  $\text{CaF}_2$  to fracture rather than slip when compared to MgO is understandable. The fact that it is the ratio of fracture energy to shear stress rather than the magnitude of either property is borne out by the impacts on LiF. LiF is much softer than either  $\text{CaF}_2$  or MgO (based on the magnitude of the critical resolved shear stress and microhardness) but has a high ratio of fracture energy to shear stress and exhibits, as does MgO, limited fracture and extensive slip. It is apparent that water



drop impact resistance in single crystals will benefit most from increases in fracture energy rather than hardness.

Since  $\text{CaF}_2$  was susceptible to fracture, the surface finish strongly influenced the extent and character of the damage due to water drop collisions.



REFERENCES

- W.F. Adler (1977). J. Mat. Sci., 12, 1253-1271.
- W.F. Adler (1979). In Treatise on Materials Science and Technology, Vol. 16 (C.M. Preece, ed.). Academic Press, New York.
- W.F. Adler and S.V. Hooker (1976). "Characterization of Transparent Materials for Erosion Resistance," Air Force Materials Laboratory Report AFML-TR-76-16.
- W.F. Adler and S.V. Hooker (1977). "Impact Damage in Single Crystals," Office of Naval Research Technical Report for Contract No. N00014-76-C-0744.
- W.F. Adler and S.V. Hooker (1978). J. Mat. Sci., 13, 1015-1025.
- C.N. Ahlquist (1974). Acta Met., 22, 1133-1137.
- A.S. Argon and E. Orowan (1964). Phil. Mag., 9, 1003-1021, 1023-1039.
- P.F. Becher (1976). Personal Communication.
- A. Behrendt (1974). In "Proceedings of the Fourth International Conference on Rain Erosion and Associated Phenomena," (A.A. Fyall and R.B. King, eds.) pp. 425-448. Royal Aircraft Establishment, Farnborough, England.
- F.P. Bowden and J.H. Brunton (1961). Proc. R. Soc. Lond., A263, 433-450.
- F.P. Bowden and J.E. Field (1964). Proc. R. Soc. Lond., A282, 331-352.
- A. Briggs, F.J.P. Clarke, and H.G. Tattersall (1964). Phil. Mag., 9, 1041-1055.
- C.A. Brooks and P.R. Burnand (1973). In The Science of Hardness Testing and Its Research Applications (J.H. Westbrook and H. Conrad, eds.) pp. 199-211. American Society for Metals, Metals Park, Ohio.
- J.H. Brunton (1966). Phil. Trans. R. Soc., A260, 79-85.
- R. Burn and G.T. Murray (1962). J. Amer. Ceramic Soc., 45, 251-252.
- J.D. Carlyle, M.E. Graham, and T.L. Menna (1975). Review of Scientific Instruments, 46, 1221-1225.
- F.J.P. Clarke, R.A. Sambell, and H.G. Tattersall (1962). Phil. Mag., 7, 393-413.
- A.H. Cottrell (1958). Trans. AIME, 212, 192.
- A.G. Evans (1979). Personal Communication, 8 February 1979.

- A.G. Evans and E.A. Charles (1976). J. Amer. Ceramic Soc., 59, 371-372.
- A.G. Evans, M.E. Gulden, G.E. Eggum, and M. Rosenblatt (1977). "Impact Damage in the Elastic Response Regime," Office of Naval Research Technical Report for Contract No. N00014-75-C-0669 for the period 1 Jan. to 30 Sept. 1977.
- A.G. Evans and T.R. Wilshaw (1977). J. Mat. Sci., 12, 97-116.
- A.G. Evans, T.R. Wilshaw, J.C. Chestnutt, and H. Nadler (1976). "Quasi-static Solid Particle Damage in Brittle Materials," Office of Naval Research Interim Report for Contract N00014-75-C-0669 for the period March 1975 to January 1976.
- O.G. Engel (1958). J. Res. NBS, 60, 245-280.
- O.G. Engel (1955). J. Res. NBS, 54, 51-59.
- J.E. Field, J.J. Camus, D.A. Gorham, and D.G. Rickerby (1974). In "Proceedings of the Fourth International Conference on Rain Erosion and Associated Phenomena," (A.A. Fyall and R.B. King, eds.) pp. 395-420. Royal Aircraft Establishment, Farnborough, England.
- J.E. Field, J.J. Camus, D.A. Gorham, and D.G. Rickerby (1976). "High Speed Liquid Impact Studies," Univ. of Cambridge, DR Mat. Report 203.
- J.E. Field, D.A. Gorham, and D.G. Rickerby (1979). In "Erosion: Prevention and Useful Applications," ASTM STP 664, (W.F. Adler, ed.) pp. 298-319. American Society for Testing and Materials, Philadelphia.
- S. Freiman, P. Becher, R. Rice, and K. Subramanian (1976). In Proc. Fifth Annual Conference on Infrared Laser Window Materials, pp. 519-533. Defense Advanced Research Projects Agency, Arlington, VA.
- A.A. Fyall (1967). In "Proceedings of the Second Meersburg Conference on Rain Erosion and Allied Phenomena," (A.A. Fyall and R.B. King, eds.) pp. 563-586. Royal Aircraft Establishment, Farnborough, England.
- A.A. Fyall (1970). In "Radome Engineering Handbook," (J.D. Walton, Jr., ed.) pp. 461-572. Marcel Dekker, New York.
- A.A. Fyall and P.A. Smith (1973). In "Proceedings IUTAM Symposium on Non-Steady Flow of Water at High Speeds," (L.I. Sedov and G. Yu. Stepanov, eds.) pp. 187-196. "Nauka" Publishing House, Moscow.
- J.J. Gilman (1954). J. Metals, 6, 621.
- J.J. Gilman (1960). J. Appl. Phys., 31, 2208-2218.

- J.J. Gilman and W.G. Johnston (1957). In Dislocations and Mechanical Properties of Crystals, pp. 117-163. Wiley, New York.
- A.E. Gorum, E.R. Parker, and J.A. Pask (1958). J. Am. Ceramic Soc., 41, 161-
- J.V. Hackworth and L.H. Kocher (1977). "Exploratory Development of Rain Erosion Resistant Infrared Window Materials," Air Force Materials Laboratory Report AFML-TR-77-84.
- F.J. Heyman (1968). Trans. ASME, J. Basic Eng., 90, 400-402.
- R.G. Hoagland and R.G. Jung (1978). "Water-Droplet Impact-Characterization of Damage Mechanisms," Office of Naval Research Final Technical Report for Contract No. N00014-76-C-0645.
- S.V. Hooker and W.F. Adler (1978). In Fracture Mechanics of Ceramics, 3 (R.C. Bradt, D.P.H. Hasselman, and F.F. Lange, eds.). Plenum Press, New York.
- C.O. Hulse, S.M. Copley, and J.A. Pask (1963). J. Amer. Ceramic Soc., 46, 317-323.
- D.C. Jenkins (1955). Nature, 176, 303-304.
- W.G. Johnston (1962). In Progress in Ceramic Science, Vol. 2 (J.E. Burke, ed.) pp. 1-75. Pergamon Press, New York.
- W.G. Johnston and J.J. Gilman (1959). J. Appl. Phys., 30, 129-144.
- W.G. Johnston and J.J. Gilman (1960). J. Appl. Phys., 31, 632-643.
- K.H. Jolliffe (1966). Phil. Trans., A260, 101-108.
- A.S. Keh (1960). J. Appl. Phys., 31, 1538-1545.
- A.S. Keh, J.C.M. Li, and Y.T. Chou (1959). Acta Met., 7, 694-696.
- G.H. Kinner (1967). In "Proceedings of the Second Meersburg Conference on Rain Erosion and Allied Phenomena," (A.A. Fyall and R.B. King, eds.) pp. 517-529. Royal Aircraft Establishment, Farnborough, England.
- M.J. Klein (1965). Phil. Mag., 12, 735-739.
- M.J. Klein and J.W. Edington (1966). Phil. Mag., 14, 21-29.
- P.W. Kruse (1962). Elements of Infrared Technology. John Wiley & Sons, New York.
- J.L. Lankford and R.A. Leverance (1971). "Determination of Threshold Damage in Radome Materials by Discrete Impact in a Ballistics Range," Naval Ordnance Laboratory Technical Report NOLTR-71-113.
- J.L. Lankford, R.A. Leverance, and S.A. Longas (1973). "Threshold Damage in Radome Materials by Discrete Water Impact (Ballistics Range Investigation)," Naval Ordnance Laboratory Report NOLTR-73-34.



- H.W. Leipmann and A. Roshko (1957). Elements of Gas Dynamics, Wiley, New York.
- J. Narayan (1973). Wear, 25, 99-109.
- J. Narayan and J. Washburn (1973). Wear, 23, 128-132.
- J.B. O'Neill, B.A.W. Redfern, and C.A. Brookes (1973). J. Mat. Sci., 8, 47-58.
- E. Orowan (1954). In Dislocations in Metals (M. Cohen, ed.) pp. 191 ff. American Society of Mining and Metallurgical Engineers, New York.
- W.L. Phillips, Jr. (1961). J. Amer. Ceramic Soc., 44, 499-506.
- A.A. Ranger and J.A. Nicholls (1969). AIAA J., 7, 285-289.
- W.G. Reinecke and W.L. McKay (1976). AIAA J., 14, 1635-1636.
- D.G. Rickerby (1977). Ph.D. Thesis, Univ. of Cambridge, Cambridge, England.
- K. Sangwal and J.N. Sutaria (1976). J. Mat. Sci., 11, 2271-2282.
- K.W. Schuler (1970). J. Mech. Phys. Solids, 18, 277-293.
- A.E. Siegal (1965). The Theory of High Speed Guns, NATO AGARDograph 91.
- R.J. Stokes, T.L. Johnston, and C.H. Li (1960). Phil. Mag., 6, 9-24.
- R.J. Stokes, T.L. Johnston, and C.H. Li (1959a). Trans. AIME, 215, 437.
- R.J. Stokes, T.L. Johnston, and C.H. Li (1959b). Phil. Mag., 4, 920-932.
- R.J. Stokes, T.L. Johnston, and C.H. Li (1958). Phil. Mag., 3, 718-725.
- G.D. Waldman and W.G. Reinecke (1971). AIAA J., 9, 1040-1048.
- J. Washburn, A.E. Gorum, and E.R. Parker (1959). Trans. AIME, 215, 230-237.
- A.R.C. Westwood and D.L. Goldheim (1963). J. Appl. Phys., 34, 3335.
- J.M. Wimmer and G.A. Graves (1977). "Exploratory Development on Multi-disciplinary Characterization of Infrared Transmitting Materials," Semiannual Progress Report No. 1, University of Dayton Research Institute Report UDRI-TR-77-35.